

On the (*Generative*) Linear Sketching Problem

Xinyu Yuan¹ Yan Qiao² Zonghui Wang¹ Wenzhi Chen¹

Abstract

Sketch techniques have been extensively studied in recent years and are especially well-suited to data streaming scenarios, where the sketch summary is updated quickly and compactly. However, it is challenging to recover the current state from these summaries in a way that is accurate, fast, and real. In this paper, we seek a solution that reconciles this tension, aiming for near-perfect recovery with lightweight computational procedures. Focusing on *linear sketching* problems of the form $\Phi f \rightarrow f$, our study proceeds in three stages. First, we dissect existing techniques and show the root cause of the sketching dilemma: an *orthogonal* information loss. Second, we examine how *generative* priors can be leveraged to bridge the information gap. Third, we propose FLORE, a novel generative sketching framework that embraces these analyses to achieve the best of all worlds. More importantly, FLORE can be trained without access to ground-truth data. Comprehensive evaluations demonstrate FLORE’s ability to provide high-quality recovery, and support summary with low computing overhead, outperforming previous methods by up to $10^3 \times$ in error reduction and $10^2 \times$ in processing speed compared to learning-based solutions. Our codebase will be released publicly in the near future.

1. Introduction

Accurately measuring the volume of water from a fire hose while being directly hit by it is nearly an impossible feat. In essence, this captures the central difficulty of streaming data analysis: the data item arrives in a continuous, unrelenting torrent, so instead we need to process each observation quickly to create a summary of the current state. Such a summary is referred to as a *sketch* of the data, which has been extensively studied (Krishnamurthy et al., 2003; Cormode,

¹College of Computer Science and Technology, Zhejiang University, Hangzhou, China ²School of Computer Science and Information Engineering, Hefei University of Technology, Hefei, China. Correspondence to: Zonghui Wang <zhwang@zju.edu.cn>, Wenzhi Chen <chenwz@zju.edu.cn>.

Preprint. March 17, 2026.

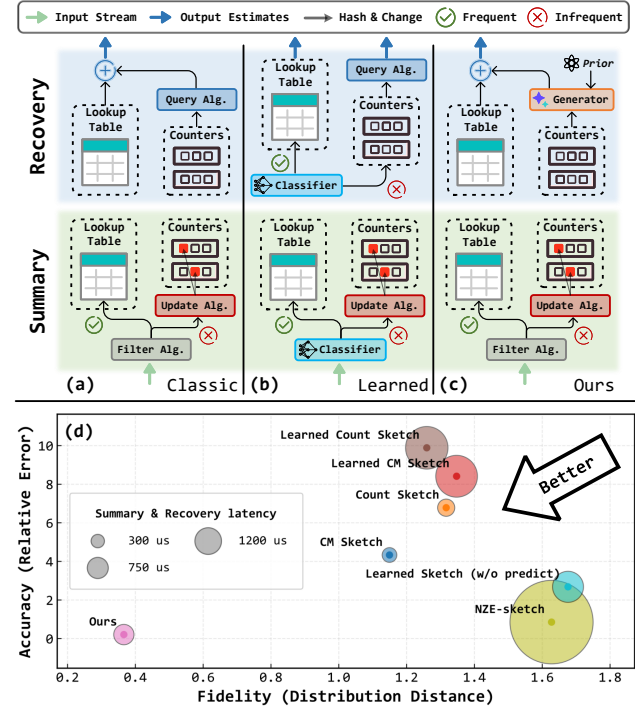


Figure 1. Comparison of our generative sketch solution and existing solutions. From (a) to (c), we present an overview of the full pipelines of three sketching frameworks. In (d), our proposal achieves the best trade-off among accuracy, fidelity and efficiency.

2017; Larsen et al., 2019), since it is helpful in any situation where people are monitoring a database or network that is being updated continuously. However, coping with the vast scale of information means making compromises—the description of the world via data sketching is approximate rather than exact. A particular challenge has been to design algorithms that navigate tradeoffs effectively, like sacrificing speed for accuracy or memory consumption for reliability (Bloom, 1970). The challenge gets harder, though, when the questions about stream get more complicated, e.g., heavy hitters (Misra & Gries, 1982), entropy (Chakrabarti et al., 2006), and graph summarization (Tang et al., 2016).

Drawing inspiration from compressive sensing (CS, Cormode & Muthukrishnan, 2005b), this paper interprets sketch as a coding problem, i.e., it is encoding sparse information, such as heavy-tailed traffic, down to compact summary and trying to extract information that lets them recover what was put in initially (§2.1). Further, if the coding procedure is

able to be represented as a linear transform of the input, i.e., $b = \Phi f$, it results in what we call a linear sketching problem (Cormode, 2011; Li et al., 2014). From this perspective, we show a fundamental tension between sketching cost and accuracy for existing techniques (§2.2). In particular, our analysis uncovers that the root cause lies in an inherent deficiency of orthogonal information that cannot be recovered without prior knowledge (§2.3). The central challenge thus shifts toward compensating for the missing component that meets both fidelity and efficiency requirements.

In order to overcome the above challenge, this work turns to a brand new sketching paradigm empowered by generative models (GMs). Our key insight is two-fold: (i) Systematically, since data-plane summary is on the critical path, as illustrated in Figure 1(c), deploying GMs for recovery in the control plane may avoid burdening the overall system. (ii) Theoretically, by enforcing consistency with the learned generative prior, GMs may help mitigate the aforementioned information loss from aggressive summarization. We study the generative linear sketching problem along two lines. In the *first line* (§3.1), we examine prevalent GMs on synthetic but representative streaming scenarios. Our preliminary experiments show that all GMs fit low-cardinality stream distributions (<10K distinct keys) well; however, it is non-trivial to scale these models other than flow-based generative model (FGM) to real-world applications, due to limitations of their own (e.g., unstable training, slow inference, and awful expressiveness). This motivates the *second line* (§3.2) of our work that leverages FGM to develop a novel and practical methodology for solving problems of interest. Specifically, we propose FLORE, the *first* deep generative sketching framework for fast summarization and accurate recovery while preserving fidelity (see Figure 1(d) for a comparative view of the trade-off under a 1MB sketch memory budget on CAIDA-2018 dataset). To realize FLORE, there are three core designs as follows. ① Instead of designing from scratch, we use the analysis results as a guideline: FLORE is purposefully modeled as an invertible solver to separate and generate the lost information from orthogonal subspaces of its underlying sketch. ② Since it is impractical to collect ground truth (GT) labels, FLORE is able to be trained with only accessing aggregated counters, based on a well-designed Expectation Maximization (EM) algorithm. ③ FLORE can easily support long-term, lightweight operation for high-speed, high-volume data streams without frequent model changes (see Appendix G.4), leveraging a stream filtering technique and scalable INN architecture.

Contributions. We summarize our contributions as follows:

- We dissect existing sketch techniques from a perspective of matrix analysis based on CS theory. We reveal the orthogonal irrecoverability that precludes perfect recovery from compact summary of the data stream.
- We investigate the feasibility of applying GMs to enhance

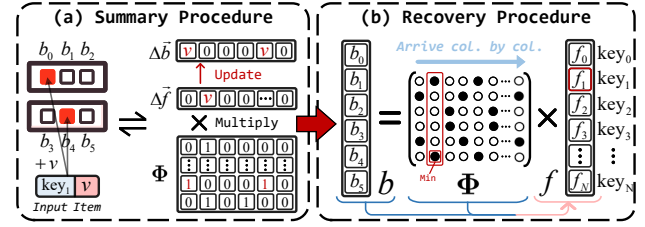


Figure 2. **Matrix formulation of Count-Min Sketch.** The linear sketching problem can be analyzed via simple matrix operations.

data sketching. By testing representative GM families, we find that, except for FGMs, they either scale poorly or fall short in the desired efficiency or accuracy.

- We design a new sketching framework, FLORE, that efficiently utilizes the distribution modeling capability of FGMs to embrace our analyses seamlessly. First, FLORE theoretically supports unbiased recovery, even without knowledge about the GT data. Second, FLORE is scalable and generic to various applications. To our best knowledge, the generative stream processing paradigm is never explored before.
- We conduct a comprehensive evaluation of FLORE on data streams simulated using ten datasets with diverse sizes and distributions. The results demonstrate FLORE outperforms nine state-of-the-art (SOTA) solutions, achieving up to a $10^3 \times$ reduction in per-element frequency estimation error, a $10^2 \times$ improvement in accurately estimating entropy and overall distributions, and up to a 80+ point gain in heavy-hitter detection. It also attains higher sketching throughput than prior art and can be further accelerated on GPUs.

2. Motivating Analyses

2.1. Problem Formulation

A data stream is a sequence of n tuples arriving in order. The t -th tuple is denoted as (key_t, v_t) , where $key_t \in \mathcal{I}$ is a data-item key used for hashing and v_t is a value associated with the item. These n tuples can have duplicate keys, but algorithms running on the data stream must be *one-pass*. Sketch techniques utilize a compact data structure to summarize each incoming item with constant-time complexity, e.g., $\mathcal{O}(k)$ when applying k independent hash functions to (flattened) counters $b \in \mathbb{R}^m$. Upon receiving a query, the goal is to recover the required statistics from the sketch summary, most notably frequencies $f \in \mathbb{C}^N$ in this paper.

Tailored problem. Our study focuses on the *linear sketching* problem, where the summary is defined to have a linear part such that each counter is updated linearly by incoming items. We further consider f to be sparse or heavy-tailed, a property justified and utilized in many prior works (Roy et al., 2016; Huang et al., 2017). Then, the problem falls into a classical CS framework: $\min_{\Phi f=b} \|f\|_1$, where Φ is an indicator matrix produced by multiple hashing operations, and its columns are presented one by one. In Figure 2, we use Count-Min Sketch as an example to illustrate the

matrix formulation with two procedures: summary and recovery. In this setting, $\Phi_{i,j} = 1$ if and only if key j is hashed to counter i ; otherwise, $\Phi_{i,j} = 0$. This problem is often highly ill-posed, i.e., $m \ll N$, and has been shown to be NP-hard (Foucart & Rauhut, 2022).

Note: We assume that the possible key set \mathcal{I} is known at the start of data streams, following the recent study (Da Dalt et al., 2022). In fact, the online collection of \mathcal{I} can be easily achieved by employing a simple Bloom Filter (Sheng et al., 2021), as detailed in Appendix D.1. For untracked keys, we report zeros as their final estimates¹, and extend our formulation to $\min_{\Phi f = b + \epsilon} \|f\|_1$ where ϵ captures the error induced by them. We will empirically show in §4 that the framework maintains overall accuracy under incomplete \mathcal{I} .

2.2. Limitations of Existing Techniques

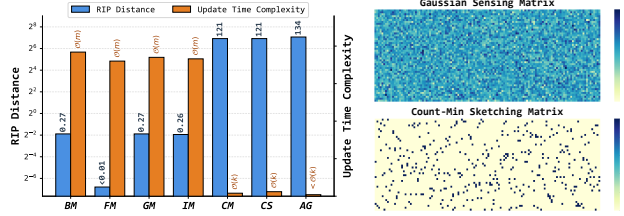
(1) Randomized approximation. Traditionally, \hat{f}_i is carried out by extracting information associated with key i from the sketch summary, which means each element’s estimate is computed individually. Representative sketch techniques include Count-Min Sketch (CM, Cormode & Muthukrishnan, 2005a) and Count Sketch (CS², Charikar et al., 2002). Essentially, their recovery of \hat{f}_i is based on observing only k entries of Φ , ignoring the influence of all other keys. While their processes are very fast (requiring only $\mathcal{O}(k)$ time) and aggregation by minimum or mean suppresses partial noise, the per-element accuracy, e.g., $\varepsilon \|f\|_1$ for CM and $\varepsilon \|f\|_2$ for CS, where ε denotes the sketch coefficient, is heavily constrained by the space budget, i.e., number of rows in Φ .

(2) Disentangled augmentation. The second class splits the sketch into two smaller components: a heavy part for frequent elements and a light part for infrequent elements. The Augmented Sketch (AG, Roy et al., 2016) and learning-augmented sketches (Hsu et al., 2019) both fall into this category. This design more effectively handles skewed distributions by mitigating hash collisions. From our perspective, such methods can be interpreted as a decomposition of the sketching matrix Φ , which allocates nonzero entries into separate components. By clearing columns of Φ , the degree of underdetermination is thus decreased. However, when resources are bounded, the capacity of the heavy part is limited. Additionally, the light part continues to suffer from large error bounds across all algorithms, which can become even worse under a fixed total space budget.

(3) Compressive sensing. Recently, the sketch techniques have begun to compute estimates for all elements simultaneously rather than independently. They typically decode all information by solving a system of linear equations using CS algorithms. Among these sketches, the PR-sketch

¹Amand et al., 2023 proved that truncating low frequency estimates to zeros will not impact the system’s overall accuracy.

²It should be distinguished from the compressive sensing (CS).



(a) RIP (acc.) & complexity (speed) (b) Measurement matrix
Figure 3. Compare compressive sensing with sketch techniques.

(PR, Sheng et al., 2021) and NZE-sketch (NZE, Huang et al., 2021) represent the most mature examples. Before proceeding with our analysis, we need to introduce a notion called restricted isometry property (RIP, Candes, 2008), which characterizes how well Φ preserves the norm of sparse signals. Since Φ must operate uniformly over all sparse vectors, this property is quantified by a sequence of restricted isometry constants (RICs), denoted by $\{\delta_s\}$, where

$$\delta_s = \sup \left\{ \frac{|\|\Phi x\|_2 - \|x\|_2|}{\|x\|_2} : x \text{ is an } s\text{-sparse vector} \right\}.$$

We say that Φ satisfies the RIP if δ_s is small for reasonably large s . Under this condition, the following error bound of CS-based sketch techniques holds:

Proposition 2.1. *Suppose that for $p > 0$, the error of best s -term approximation is denoted by $\sigma_s(f)_p := \inf_{\|z\|_0 \leq s} \|f - z\|_p$. Then, for any vector $f \in \mathbb{C}^N$, a CS solution f^* with $b = \Phi f + \epsilon$ and $\|\epsilon\|_2 \leq \eta$ approximates f with ℓ_2 -error*

$$\|f^* - f\|_2 \leq C s^{-1/2} \sigma_s(f)_1 + 2C\eta \quad (1)$$

where the constant $C = \frac{2(1+\rho)}{1-\rho}$ and $\rho \propto \delta_{2s}$.

Due to space constraints, we defer all detailed proofs henceforth to Appendix E. Proposition 2.1 indicates that their per-element accuracy is bounded on the order of around $\mathcal{O}(C s^{-1/2} \sigma_s(f)_1 / N)$, which is tighter than the bounds of previous techniques. However, this comes at a greatly increased query cost (Chakrabarti et al., 2025) and does not imply better estimates in practice. Since the coefficient C is positively correlated with RICs, we measure the RIP distance (i.e., the difference between $\|\Phi f\|_2$ and $\|f\|_2$) of the classical CS matrices and the matrices induced by sketch techniques. We test four types of CS matrices (Szarek, 1991; Candes & Tao, 2006): ① Bernoulli Matrix (BM), ② Fourier Matrix (FM), ③ Gaussian Matrix (GM), and ④ Incoherence Matrix (IM). In Figure 3(a), we can see that all three sketch techniques suffer from extremely high RIP distance (>120), while CS matrices achieve much smaller ones (<0.3). This discrepancy stems from the sparse characteristic of real-world sketching matrices, as visualized in Figure 3(b), because only updating a small number, e.g., $\mathcal{O}(k)$, of counters each time can keep pace with data streams. Thus, CS is still not enough for efficiently solving the target

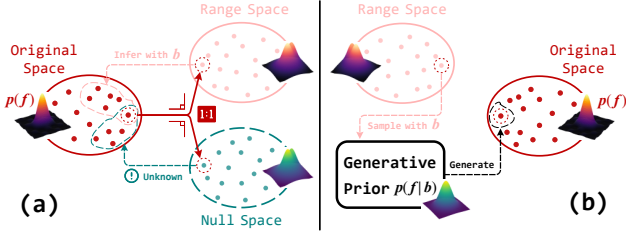


Figure 4. **Illustration of our key insights.** (a) The original streaming data cannot be recovered due to orthogonal information loss in the null space. (b) We leverage GMs to generate the null-space component which is in harmony with the range-space component.

problem. Theorem 2.2 formally shows that sketching matrices, e.g., $(0, 1)$ -matrix of CM, require substantially more rows (or counters here) than optimal RIP matrices.

Theorem 2.2. *Let $f \in \mathbb{C}^N$ be s -sparse and Φ be an $m \times N$ matrix that satisfies RIP for perfect recovery of the vector f . Then, the necessary number of counters*

$$m \geq \begin{cases} \mathcal{O}(s \log(N/s)), & \text{if } \Phi \text{ is random dense,} \\ \mathcal{O}(s^2), & \text{if } \Phi \text{ is 0-1 sparse.} \end{cases} \quad (2)$$

2.3. The Anatomy of Failure

Acknowledging the fundamental limitations of existing techniques, we next analyze the root causes of their poor performance. Our methodology is to examine whether compressed b admits perfect recovery of f , and range-null space decomposition is at the core of our work. Here we first introduce the definitions of null space and range space. A vector f_N is said to lie in the null space of Φ if and only if $\Phi f_N = 0$, and f_Φ lies in the range space of Φ if and only if $\Phi f_\Phi = b$. See related works (Wang et al., 2023; Fang et al., 2025) for more details. For any linear system, an arbitrary signal f can be decomposed into two parts: $f = f_\Phi + f_N$. This decomposition can be obtained in various ways, e.g., the singular value decomposition (SVD) used in Appendix E.5. In the context of linear sketching problems, however, this unfortunately leads to the following negative result.

Proposition 2.3. *The sketch summary b captures only the range-space component f_Φ , while the null-space component f_N is orthogonal to f_Φ and irrecoverable from b .*

Figure 4(a) illustrates the implication of Proposition 2.3, which we term *orthogonal irrecoverability*. To guarantee exact recovery, it basically requires that all f_N are nearly-zero vectors, as they are entirely discarded during compression. This requirement is especially hard to meet for sparse matrices induced by sketch techniques, motivating the use of external prior knowledge to compensate for the missing information, which we will get to later.

3. Deep Generative Linear Sketching

On generative optimization and why it might do better. As outlined in §2, relying solely on the summary b is insuf-

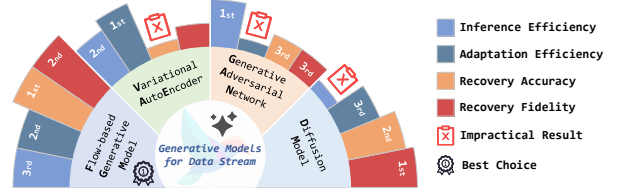


Figure 5. **Performance comparison across different GMs.** FGM achieves the most favorable trade-off in sketching tasks (*higher the better*). Detailed results are provided in Appendix F.

ficient to achieve nearly-zero-error data sketching. To break the “curse of compression”, we seek solutions that conform to two critical constraints: *consistency* and *fidelity*. For the consistency constraint, we can simply resort to the range-space $\Phi f \equiv b$. For the fidelity constraint, as discussed in §2.2, while the sparsity assumption of f is often natural and makes sense in CS theory, it is neither necessary nor sufficient for our goal. An augmented approach, which avoids presuppositions regarding f and also CS optimizations, is training a deep generator on recent realizations of the stream to directly produce samples that closely follow f ’s true distribution, thereby effectively “infilling” the null space. In Figure 4, we illustrate the key idea of which we refer to *generative prior* through the maximization of the likelihood $\log p(f | b)$. It can outperform existing techniques in scenarios where streaming data is volatile and hard to predict under limited memory budgets. Directly inferring f also obviates the need for solving a linear program, which significantly accelerates runtimes for large-scale data streams (see results in Appendix G.3.1). Once training is completed, the generator is expected to learn the unique optimum in Figure 4(b). Indeed, our proposal, FLORE, which is a manifestation of this approach, quickly converges to this outcome.

3.1. Integrating Generative Priors

There are two ways to incorporate generative priors into our algorithm design. The first is a straightforward strategy that adds distributional regularization during training, such as *Zipf’s law* (Powers, 1998). For example, the mapping $b \rightarrow f$ may be pre-trained on Zipfian datasets exhibiting similar skewness (Cao et al., 2024; Feng et al., 2025), or its outputs may be constrained to satisfy prescribed proportional structure (Yuan et al., 2026). However, this way has a clear shortcoming: the manually imposed, deterministic constraints are often overly restrictive, resulting in a narrow range of applicability. Therefore, here it is not a good fit.

In this work, we adopt the second way to establish a mapping between $[b, z]$ and f , where z is a latent vector drawn from a prior distribution, e.g., an isotropic Gaussian $\mathcal{N}(0, I)$. Unlike the previous strategy, the latent variable z explicitly introduces external information that can be actively leveraged for diverse generation. Moreover, for the guarantee of unbiased estimation, we prove the following theorem:

Theorem 3.1. *For a sketching matrix $\Phi \in \mathbb{R}^{m \times N}$ of rank*

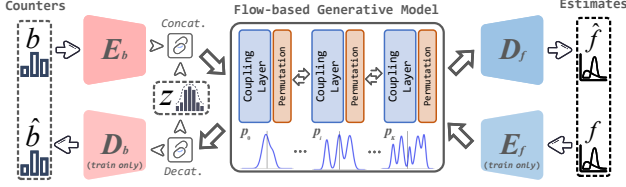


Figure 6. **Architecture of FLORE.** To enable lightweight training, FLORE is modeled as an invertible mapping in the latent space.

r , ground-truth vector $f \in \mathbb{C}^N$ and $b = \Phi f$, there exists a gaussian vector $z \in \mathbb{R}^{N-r}$ and a learnable mapping $G : \mathbb{R}^{m+N-r} \rightarrow \mathbb{R}^N$ such that $G([b, z])$ uniquely determines f .

Given the high-level view of the mapping, the next challenge is to maximize the log-likelihood of its outputs. To this end, we consider four classes of deep generative paradigms: variational autoencoder (VAE, Kingma & Welling, 2013), generative adversarial network (GAN, Goodfellow et al., 2014), diffusion model (DM, Ho et al., 2020), and flow-based generative model (FGM, Rezende & Mohamed, 2015). See our analyses on synthetic data streams with $1 \sim 100\text{K}$ distinct keys in Appendix F for differences in sketching performance between the above-listed GMs. Figure 5 presents a synopsis of the examination results. Importantly, we have three main observations: (i) GANs suffer from notorious sensitivity to adversarial training and a brittle optimization process even if we introduce the Wasserstein optimization (Arjovsky et al., 2017). (ii) VAEs rely on a loose surrogate objective, leading to poor performance as the size of the data stream increases (e.g., beyond 10K distinct keys). (iii) Although DMs are robust and enjoy stable training, their sampling complexity is prohibitively high, typically requiring several seconds, which makes them unsuitable for real-world applications. We finally adopt FGMs as the underlying model and build our designs upon them, as discussed later.

3.2. FLORE: FLOW-based Orthogonal REcovery

Below, we present the designs of our proposal, FLOW-based Orthogonal REcovery (or FLORE for short), which extends the classical FGM for sketching problems. Due to length limitations, more implementation details (e.g., data structures and summary algorithms) are included in Appendix D.

Design I: invertible architecture. As with classical FGMs, FLORE leverages invertible neural networks (INNs) for distribution learning. The INN typically consists of a sequence of transformations $\{T_i\}$ that are bijective with tractable Jacobian determinants, yielding the composite mapping

$$f = z_K = T_K \circ T_{K-1} \circ \dots \circ T_1(z_0), \quad z_0 = [b, z].$$

Similar to DMs (Rombach et al., 2022), such a chain preserves dimensionality and thus precludes intrinsic dimension reduction within INNs. Consequently, modeling large-scale data streams (with tens of thousands of unique items) makes them prone to spending excessive amounts of compute resources. So in contrast to purely INN-based approaches, our framework introduces two autoencoders to

project b and f into lower-dimensional representations (latent space) respectively, which scales more gracefully to higher-dimensional data. The overall architecture is shown in Figure 6, where the GM learns the semantic and conceptual structure of the data. The coupling operations in FLORE follow NICE (Dinh et al., 2014), with dimension shuffling applied after each layer to enhance expressive capacity.

Note: When the key set \mathcal{I} needs online collection, the data dimensionality grows dynamically. To handle this, we partition the model into conditioned sub-invertible-functions that share parameters but remain decoupled across segments, such that newly added dimensions minimally affect earlier intervals. This design further reduces model complexity and enables scalable real-time adaptation; its details can be found in Appendix D.3.

Design II: training objective. We next design a training strategy that enforces both the measurement consistency and the fidelity condition in FLORE. Specifically, the overall objective consists of three types of loss terms as follows.

① For aligning with the observation, there are two loss terms: *consistency loss* \mathcal{L}_{con} and *reconstruction loss* \mathcal{L}_{rec} . They penalize the deviations between b and f respectively. Let $f_G := G([b, z])$, then we can write

$$\mathcal{L}_{\text{con}} = \mathbb{E} \left[(\Phi f_G - b)^2 \right], \quad \mathcal{L}_{\text{rec}} = \mathbb{E} \left[(f_G - f)^2 \right].$$

② For learning the distribution, we also have two loss terms: *invertibility loss* \mathcal{L}_{inv} and *orthogonal loss* \mathcal{L}_{ort} . The former forces the INN to remain its invertibility by

$$\mathcal{L}_{\text{inv}} = \mathbb{E} \left[(f - G(G^{-1}(f)))^2 \right].$$

While the latter embraces the theoretical analysis presented in §2.3, which aims to make the distributions of z and b as orthogonal as possible, i.e., $q(b, z) = p_B(b)p_Z(z)$. Using a discrepancy metric \mathcal{D} (e.g., KLD (Kullback, 1951) or MMD (Gretton et al., 2012)), we define it as

$$\mathcal{L}_{\text{ort}} = \mathcal{D}(q(b, z) \parallel p_B(b)p_Z(z)).$$

Note: Here we do not incorporate the traditional negative log-likelihood loss, i.e., $\log p(z_0) - \log \sum_{i=1}^K \left| \det \frac{dT_i}{dz_{i-1}} \right|$, into our objective. Empirically, it tends to slow down model convergence; theoretically, Theorem 3.2 below shows that the aforementioned losses alone suffice to yield an unbiased estimation of the target (conditional) distribution.

Theorem 3.2. *If the designed loss terms, i.e., \mathcal{L}_{con} , \mathcal{L}_{inv} and \mathcal{L}_{ort} vanish, the invertible mapping $G : [b, z] \leftrightarrow f$ applied to the $p(b, z)$ recovers the true posterior $p(f | b)$.*

③ To instill *sparsity* into FLORE’s recovery (i.e., the idea of CS), we append a regularization term $\mathcal{L}_{\text{sp}} = \|f_G\|_1$.

Putting it together, we train FLORE by minimizing the loss

$$\mathcal{L}_{\text{total}} = \mathcal{L}_{\text{con}} + \alpha_1 \mathcal{L}_{\text{rec}} + \alpha_2 \mathcal{L}_{\text{inv}} + \alpha_3 \mathcal{L}_{\text{ort}} + \alpha_4 \mathcal{L}_{\text{sp}},$$

where $\alpha_{(\cdot)}$ are trade-off parameters controlling the relative contributions of individual loss terms. After training, the

learned generator G can be directly deployed to recover the streaming ground truth f from sampled inputs $[b, z]$, for both training data and previously unseen observations.

Algorithm 1 (Pytorch) Training pseudocode for FLORE

```

# Phi: linear sketching matrix (Count-Min)
# G.forw, G.back: forward and reverse process of FGM G
# a: list of trade-off parameters (alphas)

for b in loader: # load a minibatch from the stream
    # approximate GT via EM (can be pre-computed)
    f = EM_OPT_CM(b, Phi) # CM as the start point
    z = Gaussian(0, I) # sample the prior z
    f0 = G.forw([b, z]) # reconstruct f from b
    f1 = G.forw([Phi*f, z]) # reconstruct f from Phi*f
    f2 = G.forw(G.back(f)) # reconstruct f from itself
    bz = G.back(f0) # get joint distribution

    # training losses
    loss = L2Loss(Phi*f0, b) # consistency
    + a[0]*L2Loss(f1, f) # reconstruction
    + a[1]*L2Loss(f2, f) # invertibility
    + a[2]*MMD_or_KLD([b, z], bz) # orthogonality
    + a[3]*L1Loss(f0) # sparsity

    loss.backward() # compute the gradient
    update(G.params) # update G network
    
```

Design III: GT-free learning. It’s extremely hard to construct datasets that capture all aspects of very large databases in high-speed environments or testbeds. Hence, a particular challenge in our context is to train FLORE without ground truth (only counters b is available). Fortunately, taking into account the recent history of these counters, we’re able to automatically infer hidden GT patterns. The underlying sketch rules, e.g., Count-Min and Count, give a natural inductive bias for model learning (Cheng et al., 2023). Nonetheless, naively substituting the true f in the original objective by querying the sketch can destabilize the training procedure, because these estimations are often quite coarse (see §2.2).

To address this issue, we connect the approximation problem with maximum likelihood estimation (Vardi & Lee, 1993). Specifically, we can apply an EM algorithm to refine estimates obtained from the underlying sketch, and this results in the iterations described in Theorem 3.3.

Theorem 3.3. *Minimizing the Kullback–Leibler divergence $\mathcal{D}_{KL}(p(f|b) \| p(f^{(\cdot)}))$ yields the following EM update:*

$$f_i^{(n)} = f_i^{(n-1)} \sum_j \frac{\Phi_{i,j}^T}{(\Phi_{f^{(n-1)}})_j} b_j, \text{ initialized with } f_i^{(0)} > 0.$$

For a more visible connection and the corresponding proof, please refer to Appendix E.8. If the given linear sketching problem does not have a non-negative solution, then EM algorithm yields the closest approximation in terms of Kullback–Leibler divergence. Algorithm 1 depicts the final training procedure of FLORE in a Pytorch-like style.

Note: One may ask whether the refinement can be directly applied to linear sketching problems. Although our ablation studies in Appendix G.3.4 show that it can greatly reduce the error of conventional sketches like CM, this iterative procedure is often prohibitively expensive. In our implementation, the refinement is performed only 3–5 steps as a

one-time preprocessing operation.

Design IV: stream filtering. In the light of previous studies (Roy et al., 2016; Yang et al., 2018b; Kraska et al., 2018), we also separate frequent elements as key-value pairs and infrequent elements in the sketch. It has been proven that such separation can be realized with limited overheads, and potentially improve summary efficiency. In the data plane of FLORE, we employ a *model-free* stream filtering technique to achieve it, based on a heuristic mechanism named *Ostracism*. As a result, generative recovery is exclusively applied to the light sketch part (i.e., a Count-Min) before merging it back into the dedicated part. Algorithm details are deferred to Appendix D.2 owing to space constraints.

4. Evaluation

In this section, we evaluate the proposed approach to demonstrate that it achieves the SOTA sketching performance on (i) recovering per-element frequency (§4.1); (ii) finding heavy hitters (§4.2); (iii) estimating distribution and entropy (§4.3); and (iv) incurs limited stream processing overhead (§4.4). Note that our proposal has two variants: FLORE and FLORE (perfect). The former applies when \mathcal{I} is unknown and therefore requires allocating an additional portion of data-plane memory to deploy Bloom Filter (see note in §2.1), whereas the latter does not incur this requirement.

Datasets. We utilize *five* different real-world datasets for simulations, in which the number of distinct keys ranges from 10K to 160K. These include two Internet packet traces (CAIDA and MAWI) and three real-life data streams (Web-docs, Kosarak, and Retail). Further details are provided in Appendix C.1. In addition, we synthesize *five* data streams following different distributions (e.g., Zipf, Pareto, exponential, and log-normal) and report the results in Appendix G.1.

Baselines. We compare our proposal to *nine* SOTA streaming solutions, covering overall four mainstream sketch techniques: two classical sketches (CM and CS); two classical optimizations (AG and CU); two CS-based sketches (PR and NZE); and three learning-augmented sketches (LCM, LCS, and LS). Their specific descriptions and configurations are detailed in Appendix C.2.

Metrics. To assess sketching performance, we employ AAE and ARE to quantify estimation error, WMRE and Entropy AE to measure distribution and entropy fidelity, and FI Score to evaluate heavy-hitter accuracy. Except for the FI Score, lower values indicate better performance across all metrics. For formal definitions, please refer to Appendix C.3.

4.1. Per-Element Frequency Estimation

We first evaluate per-element frequency estimation for both frequent and infrequent items, with results shown in Figure 7 (logarithmic scale). Generally, accuracy improves as memory increases. The baseline CM and its optimizations (AG, CU) provide stable improvements, whereas CS typ-

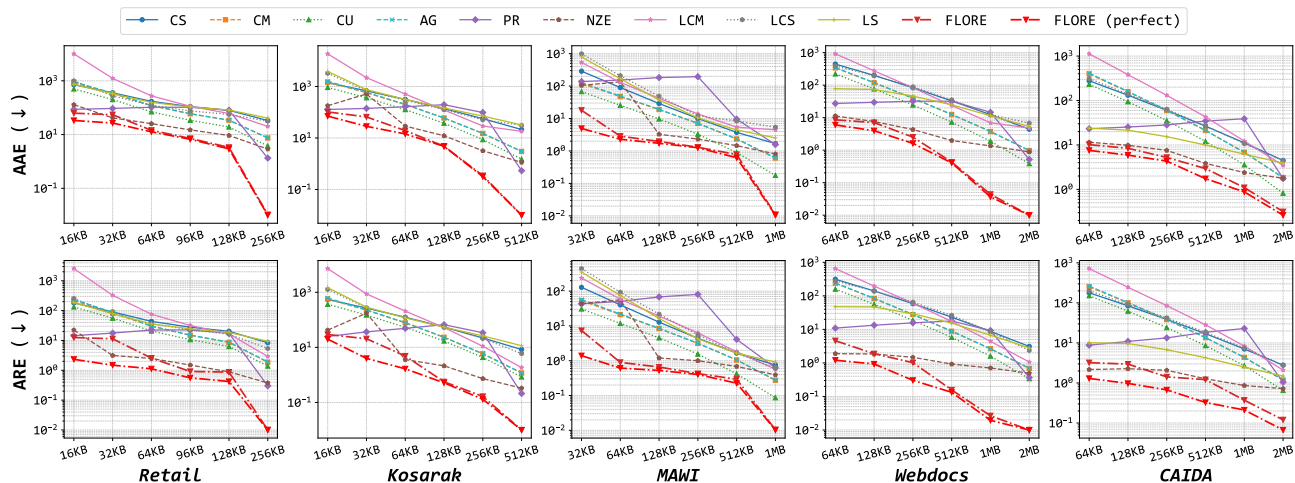


Figure 7. Comparison of per-element frequency estimation accuracy across five real-world datasets.

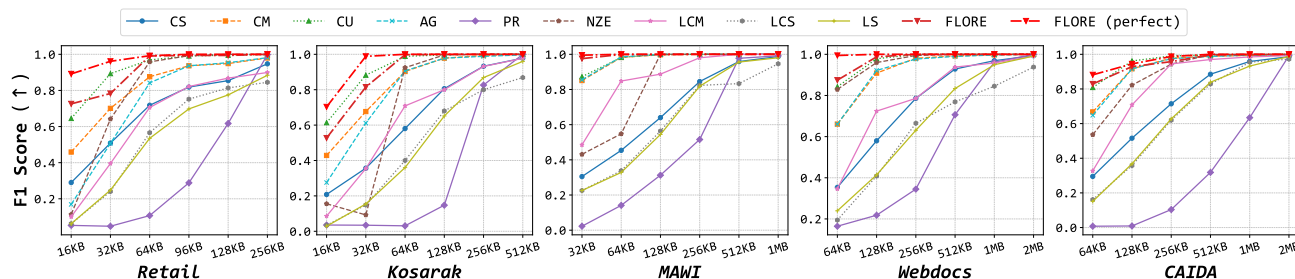


Figure 8. Comparison of heavy hitter detection accuracy across five real-world datasets.

ically lags behind CM except under small memory usage. Learning-augmented sketches (LCM, LCS) reveal a clear trade-off: they struggle in resource-constrained settings due to the high memory overhead of auxiliary structures (buckets/classifiers). While LS mitigates this via truncation, its benefits diminish as memory expands. In contrast, CS-based methods (PR, NZE) achieve remarkable precision under high compression, which beat CM by two orders of magnitude, though their performance is non-monotonic due to the under-determined recovery process. We also observe that FLORE outperforms almost all methods by several orders of magnitude. At a 256KB budget, it reduces AAE and ARE significantly, consistently surpassing CM by over 400 \times , and usually dominates PR and NZE even without GT data for its learning. Meanwhile, FLORE (perfect) marginally outperforms the standard FLORE, as expected.

4.2. Heavy-Hitter Detection

Next, we report the results for heavy-hitter detection, where the top $\log N$ items are defined as heavy hitters. Figure 8 compares the F1 Score of all solutions in heavy hitter detection under different memory sizes. Since only frequent elements are counted here, we observe the following phenomenon. First, CM and CU perform exceptionally well due to their inherent non-negativity. While AG employs an augmented filter to accurately track a small subset of hot items

(e.g., ≤ 100 positions), its overall improvement remains limited. Second, CS and its derivatives (LCS, LS) lack this non-negative property, resulting in inferior accuracy. Third, the performance of PR and NZE is strikingly reversed, with PR consistently yielding the lowest F1 Score. This is because these CS-based methods prioritize global estimation fidelity over the precise recovery of individual heavy hitters. In contrast, FLORE and FLORE (perfect) consistently outperform all these sketch techniques, maintaining a much higher F1 Score across the board. Specifically, on nearly all datasets, FLORE achieves near-perfect detection accuracy (90%~100%) with 64 KB of memory. This advantage becomes even more pronounced under fewer counters, where FLORE delivers up to a 4.5 \times improvement in average.

4.3. Estimation of Distribution & Entropy

We further evaluate the capacity of each sketch technique to model the underlying stream distribution, representing the fidelity of the recovery. As the 1st row of Figure 9 shows, an impressive performance disparity can be observed: FLORE achieves a dramatically lower distance to the real distribution compared to all baselines, despite the absence of GT data during training. Taking the CAIDA dataset as an example, FLORE with a mere 64KB memory budget achieves a level of fidelity that other sketches fail to match even with 2MB, which represents a 32 \times reduction in memory

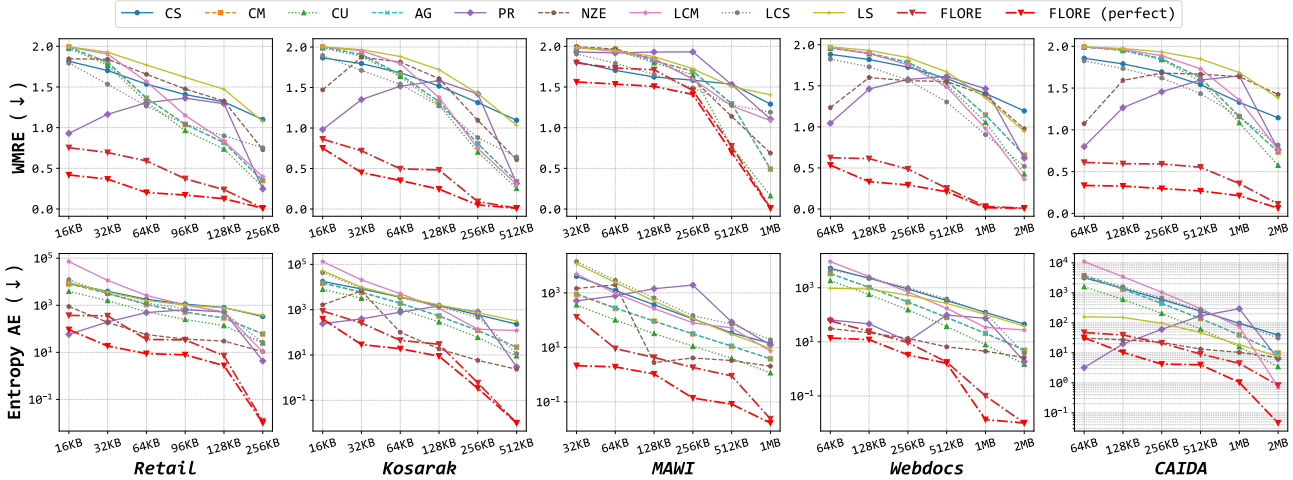
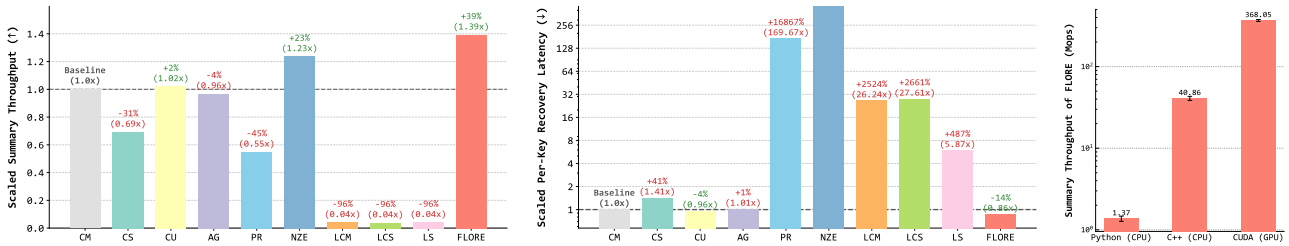


Figure 9. Comparison of distributional and entropy distances to the GT across five real-world datasets.



(a) CPU summary processing speed in natural streams (b) GPU recovery (for all keys) processing speed (c) Speed v.s. Platform
 Figure 10. Comparison of stream processing efficiency on CAIDA with 1MB memory (Green means better than the baseline, CM).

footprint for equivalent accuracy. This superiority stems from FLORE’s generative sketching paradigm, which explicitly learns and leverages the statistical structure of the data stream. Furthermore, our results reveal that per-element estimation accuracy is not necessarily indicative of global distribution fidelity. For instance, while CS-based methods may excel in point estimation, they struggle to faithfully recover the overall distribution. A similar trend is evident in the second row of Figure 9, which illustrates the advantages of our approach in entropy estimation. Interestingly, PR’s estimates are highly accurate under extreme memory scarcity but degrade sharply before stabilizing once the system transitions from an under-determined to a well-determined regime. In contrast, FLORE maintains remarkably stable performance, with the AE consistently remaining near or below 10 on average. These findings demonstrate that FLORE’s recovery is both precise and statistically consistent with GT, marking a clear departure from prior works.

4.4. Processing Efficiency

Figure 10 presents the scaled stream processing speed relative to the CM baseline. We also implement and evaluate FLORE on various platforms, such as GPU using CUDA Toolkit (NVIDIA et al., 2020). The results indicate that learning-augmented sketches suffer from low efficiency due to the required classifier forward pass. Although LS limits

the usage of Oracle (to 15% of queries here), its performance is still suboptimal. CS decoding algorithms need over 10^2 times longer recovery time to get a reliable result, which is unacceptably high. Conversely, FLORE incurs no overhead on the data-plane stream processing as it is used solely for recovery, and filtered stream with $\mathcal{O}(1)$ complexity, which outperforms the baseline in both summary and recovery phases, with gains becoming even more pronounced across different platforms. Specifically, the speed of FLORE on Cuda and C++ is 29.8, 268.6 times higher than in Python.

4.5. Other Experiments

Additional experiments, such as further comparisons, ablation studies and visualizations, are deferred to Appendix G due to space constraints.

5. Conclusion

This paper revisits sketching techniques and highlights their limitations. We find that under resource constraints, existing algorithms are fundamentally insufficient for near-perfect recovery. To bridge this gap, we introduce a new generative sketching paradigm that reframes the problem as posterior generation. These results guide us to design FLORE accordingly. The superior performance of FLORE validates the effectiveness of our methodology. We expect that more generative streaming algorithms can be designed in the future.

Impact Statement

This paper presents work whose goal is to advance the field of Machine Learning and Database Systems. All real-world data streams used in our evaluation are anonymized and do not contain user IP addresses or content-level information; therefore, this work does not raise ethical or privacy concerns. However, there are some other potential societal consequences of our work, none of which we feel must be specifically highlighted here.

References

- Aamand, A., Chen, J., Nguyen, H., Silwal, S., and Vakilian, A. Improved frequency estimation algorithms with and without predictions. *Advances in Neural Information Processing Systems*, 36:14387–14399, 2023. URL https://openreview.net/attachment?id=0VcvYQ3uPh&name=supplementary_material. cited on pages 3, 15, and 18.
- Alon, N., Matias, Y., and Szegedy, M. The space complexity of approximating the frequency moments. In *Proceedings of the twenty-eighth annual ACM symposium on Theory of computing*, pp. 20–29, 1996. cited on page 43.
- Ardizzone, L., Kruse, J., Rother, C., and Köthe, U. Analyzing inverse problems with invertible neural networks. In *The Seventh International Conference on Learning Representations*, 2019a. cited on pages 20 and 23.
- Ardizzone, L., Lüth, C., Kruse, J., Rother, C., and Köthe, U. Guided image generation with conditional invertible neural networks. *arXiv preprint arXiv:1907.02392*, 2019b. cited on page 21.
- Arjovsky, M., Chintala, S., and Bottou, L. Wasserstein gan. *arXiv preprint arXiv:1701.07875*, 685, 2017. cited on pages 5 and 30.
- Bloom, B. H. Space/time trade-offs in hash coding with allowable errors. *Communications of the ACM*, 13(7): 422–426, 1970. cited on page 1.
- Bora, A., Jalal, A., Price, E., and Dimakis, A. G. Compressed sensing using generative models. In *International conference on machine learning*, pp. 537–546. PMLR, 2017. cited on page 31.
- Bowden, R. A., Roughan, M., and Bean, N. Network link tomography and compressive sensing. In *Proceedings of the ACM SIGMETRICS joint international conference on Measurement and modeling of computer systems*, pp. 159–160, 2011. cited on page 16.
- Brijs, T., Swinnen, G., Vanhoof, K., and Wets, G. Using association rules for product assortment decisions: A case study. In *Proceedings of the fifth ACM SIGKDD international conference on Knowledge discovery and data mining*, pp. 254–260, 1999. URL <http://fimi.uantwerpen.be/data/retail.dat>. cited on page 17.
- Caida. Caida anonymized internet traces 2018 dataset, 2018. URL https://catalog.caida.org/dataset/passive_2018_pcap. cited on page 16.
- Candes, E. J. The restricted isometry property and its implications for compressed sensing. *Comptes rendus. Mathematique*, 346(9-10):589–592, 2008. cited on pages 3 and 23.
- Candes, E. J. and Tao, T. Decoding by linear programming. *IEEE transactions on information theory*, 51(12):4203–4215, 2005. cited on page 23.
- Candes, E. J. and Tao, T. Near-optimal signal recovery from random projections: Universal encoding strategies? *IEEE transactions on information theory*, 52(12):5406–5425, 2006. cited on page 3.
- Cao, Y., Feng, Y., Wang, H., Xie, X., and Zhou, S. K. Learning to sketch: A neural approach to item frequency estimation in streaming data. *IEEE Transactions on Pattern Analysis and Machine Intelligence*, 46(11):7136–7153, 2024. cited on pages 4 and 15.
- Chakrabarti, A., Do Ba, K., and Muthukrishnan, S. Estimating entropy and entropy norm on data streams. *Internet Mathematics*, 3(1):63–78, 2006. cited on page 1.
- Chakrabarti, A., Jiang, J., Woodruff, D. P., and Yasuda, T. Streaming algorithms for ℓ_p flows and ℓ_p regression. In *The Thirteenth International Conference on Learning Representations*, 2025. cited on page 3.
- Chandar, V. A negative result concerning explicit matrices with the restricted isometry property. *preprint*, 2008. cited on page 23.
- Charikar, M., Chen, K., and Farach-Colton, M. Finding frequent items in data streams. In *International Colloquium on Automata, Languages, and Programming*, pp. 693–703. Springer, 2002. cited on pages 3, 15, and 17.
- Chen, Y.-C., Qiu, L., Zhang, Y., Xue, G., and Hu, Z. Robust network compressive sensing. In *Proceedings of the 20th annual international conference on Mobile computing and networking*, pp. 545–556, 2014. cited on page 16.
- Cheng, X., Jing, X., Yan, Z., Li, X., Wang, P., and Wu, W. Alsketch: An adaptive learning-based sketch for accurate network measurement under dynamic traffic distribution. *Journal of Network and Computer Applications*, 216: 103659, 2023. cited on pages 6 and 15.

- Cho, K., Mitsuya, K., and Kato, A. Traffic data repository at the {WIDE} project. In *2000 USENIX Annual Technical Conference (USENIX ATC 00)*, 2000. URL <https://mawi.wide.ad.jp/mawi/>. cited on page 16.
- Chung, H., Kim, J., Mccann, M. T., Klasky, M. L., and Ye, J. C. Diffusion posterior sampling for general noisy inverse problems. In *The Eleventh International Conference on Learning Representations*, 2023. cited on page 31.
- Cormode, G. Sketch techniques for approximate query processing. *Foundations and Trends in Databases. NOW publishers*, 15, 2011. cited on page 2.
- Cormode, G. Data sketching. *Communications of the ACM*, 60(9):48–55, 2017. cited on page 1.
- Cormode, G. and Muthukrishnan, S. An improved data stream summary: the count-min sketch and its applications. *Journal of Algorithms*, 55(1):58–75, 2005a. cited on pages 3, 15, and 17.
- Cormode, G. and Muthukrishnan, S. Towards an algorithmic theory of compressed sensing. *Center for Discrete Math. and Comp. Sci.(DIMACS), Tech. Rep. TR*, 25:2005, 2005b. cited on page 1.
- Cormode, G., Garofalakis, M., Haas, P. J., Jermaine, C., et al. Synopses for massive data: Samples, histograms, wavelets, sketches. *Foundations and Trends® in Databases*, 4(1–3):1–294, 2011. cited on page 17.
- Da Dalt, F., Scherrer, S., and Perrig, A. Bayesian sketches for volume estimation in data streams. *Proceedings of the VLDB Endowment*, 16(4):657–669, 2022. cited on pages 3 and 15.
- Dinh, L., Krueger, D., and Bengio, Y. Nice: Non-linear independent components estimation. *arXiv preprint arXiv:1410.8516*, 2014. cited on pages 5 and 20.
- Dinh, L., Sohl-Dickstein, J., and Bengio, S. Density estimation using real nvp. *arXiv preprint arXiv:1605.08803*, 2016. cited on page 20.
- Douligeris, C. and Mitrokotsa, A. Ddos attacks and defense mechanisms: classification and state-of-the-art. *Computer networks*, 44(5):643–666, 2004. cited on page 43.
- Du, E., Wang, F., and Mitzenmacher, M. Putting the “learning” into learning-augmented algorithms for frequency estimation. In *International Conference on Machine Learning*, pp. 2860–2869. PMLR, 2021. cited on pages 15, 17, and 22.
- Eigen Developers. Eigen::LeastSquaresConjugateGradient class reference, 2025. URL https://eigen.tuxfamily.org/dox/classEigen_1_1LeastSquaresConjugateGradient.html. cited on page 17.
- Eppstein, D., Goodrich, M. T., Uyeda, F., and Varghese, G. What’s the difference? efficient set reconciliation without prior context. *ACM SIGCOMM Computer Communication Review*, 41(4):218–229, 2011. cited on page 19.
- Estan, C. and Varghese, G. New directions in traffic measurement and accounting: Focusing on the elephants, ignoring the mice. *ACM Transactions on Computer Systems (TOCS)*, 21(3):270–313, 2003. cited on pages 15 and 17.
- Fang, J., Jiang, H., Wang, K., Ma, Y., Shi, J., Wang, X., He, X., and Chua, T.-S. Alphaedit: Null-space constrained knowledge editing for language models. In *The Thirteenth International Conference on Learning Representations*, 2025. cited on page 4.
- Feng, Y., Cao, Y., Hairu, W., Xie, X., and Zhou, S. K. Mayfly: a neural data structure for graph stream summarization. In *The twelfth international conference on learning representations*, 2023. cited on page 15.
- Feng, Y., Cao, Y., Wang, H., Xie, X., and Zhou, S. K. Lego sketch: A scalable memory-augmented neural network for sketching data streams. In *Forty-second International Conference on Machine Learning*, 2025. cited on pages 4 and 15.
- Ferenc, B. Anonymized click-stream data. URL <https://fimi.uantwerpen.be/data/kosarak.dat>. cited on page 17.
- Fong, D. C.-L. and Saunders, M. Lsmr: An iterative algorithm for sparse least-squares problems. *SIAM Journal on Scientific Computing*, 33(5):2950–2971, 2011. cited on pages 17 and 38.
- Foucart, S. and Rauhut, H. A mathematical introduction to compressive sensing. *The Annals of Statistics*, 50(6): 3538–3562, 2022. cited on pages 3, 23, and 24.
- Fu, Y., Li, D., Shen, S., Zhang, Y., and Chen, K. Clustering-preserving network flow sketching. In *IEEE INFOCOM 2020-IEEE Conference on Computer Communications*, pp. 1309–1318. IEEE, 2020. cited on page 16.
- Goodfellow, I. J., Pouget-Abadie, J., Mirza, M., Xu, B., Warde-Farley, D., Ozair, S., Courville, A., and Bengio, Y. Generative adversarial nets. *Advances in neural information processing systems*, 27, 2014. cited on page 5.

- Gretton, A., Borgwardt, K. M., Rasch, M. J., Schölkopf, B., and Smola, A. A kernel two-sample test. *The journal of machine learning research*, 13(1):723–773, 2012. cited on pages 5, 23, and 24.
- Guo, C., Yuan, L., Xiang, D., Dang, Y., Huang, R., Maltz, D., Liu, Z., Wang, V., Pang, B., Chen, H., et al. Pingmesh: A large-scale system for data center network latency measurement and analysis. In *Proceedings of the 2015 ACM Conference on Special Interest Group on Data Communication*, pp. 139–152, 2015. cited on page 43.
- He, J., Zhu, J., and Huang, Q. Histsketch: A compact data structure for accurate per-key distribution monitoring. In *2023 IEEE 39th International Conference on Data Engineering (ICDE)*, pp. 2008–2021. IEEE, 2023. cited on page 16.
- Ho, J., Jain, A., and Abbeel, P. Denoising diffusion probabilistic models. *Advances in neural information processing systems*, 33:6840–6851, 2020. cited on page 5.
- Hsu, C.-Y., Indyk, P., Katabi, D., and Vakilian, A. Learning-based frequency estimation algorithms. In *International Conference on Learning Representations*, 2019. URL <https://github.com/chenyuhsu/learnedsketch>. cited on pages 3, 15, and 18.
- Huang, Q., Jin, X., Lee, P. P., Li, R., Tang, L., Chen, Y.-C., and Zhang, G. Sketchvisor: Robust network measurement for software packet processing. In *Proceedings of the Conference of the ACM Special Interest Group on Data Communication*, pp. 113–126, 2017. cited on pages 2 and 16.
- Huang, Q., Sheng, S., Chen, X., Bao, Y., Zhang, R., Xu, Y., and Zhang, G. Toward nearly-zero-error sketching via compressive sensing. In *18th USENIX Symposium on Networked Systems Design and Implementation (NSDI 21)*, pp. 1027–1044, 2021. cited on pages 3, 16, 18, and 19.
- Ikeuchi, H. and Saito, H. Network tomography based on adaptive measurements in probabilistic environments. *IEEE Transactions on Information Theory*, 70(11):8251–8265, 2024. cited on page 16.
- Jiang, T., Li, Y., Lin, H., Ruan, Y., and Woodruff, D. P. Learning-augmented data stream algorithms. *ICLR*, 2020. cited on page 15.
- Kingma, D. P. Adam: A method for stochastic optimization. *arXiv preprint arXiv:1412.6980*, 2014. cited on page 22.
- Kingma, D. P. and Dhariwal, P. Glow: Generative flow with invertible 1x1 convolutions. *Advances in neural information processing systems*, 31, 2018. cited on pages 20 and 21.
- Kingma, D. P. and Welling, M. Auto-encoding variational bayes. *arXiv preprint arXiv:1312.6114*, 2013. cited on page 5.
- Kraska, T., Beutel, A., Chi, E. H., Dean, J., and Polyzotis, N. The case for learned index structures. In *Proceedings of the 2018 international conference on management of data*, pp. 489–504, 2018. cited on pages 6, 15, and 43.
- Krishnamurthy, B., Sen, S., Zhang, Y., and Chen, Y. Sketch-based change detection: Methods, evaluation, and applications. In *Proceedings of the 3rd ACM SIGCOMM conference on Internet measurement*, pp. 234–247, 2003. cited on page 1.
- Kullback, S. Kullback-leibler divergence. *Tech. Rep.*, 1951. cited on page 5.
- Kumar, A., Sung, M., Xu, J., and Wang, J. Data streaming algorithms for efficient and accurate estimation of flow size distribution. *ACM SIGMETRICS Performance Evaluation Review*, 32(1):177–188, 2004. cited on page 18.
- Larsen, K. G., Nelson, J., Nguyen, H. L., and Thorup, M. Heavy hitters via cluster-preserving clustering. *Communications of the ACM*, 62(8):95–100, 2019. cited on page 1.
- Lee, G. M., Liu, H., Yoon, Y., and Zhang, Y. Improving sketch reconstruction accuracy using linear least squares method. In *Proceedings of the 5th ACM SIGCOMM conference on Internet Measurement*, pp. 24–24, 2005. cited on page 16.
- Li, J., Li, Z., Xu, Y., Jiang, S., Yang, T., Cui, B., Dai, Y., and Zhang, G. Wavingsketch: An unbiased and generic sketch for finding top-k items in data streams. In *Proceedings of the 26th ACM SIGKDD International Conference on Knowledge Discovery & Data Mining*, pp. 1574–1584, 2020. cited on page 15.
- Li, L., Xie, K., Pei, S., Wen, J., Liang, W., and Xie, G. Cs-sketch: Compressive sensing enhanced sketch for full traffic measurement. *IEEE Transactions on Network Science and Engineering*, 11(3):2338–2352, 2023. cited on page 16.
- Li, T. and He, K. Back to basics: Let denoising generative models denoise. *arXiv preprint arXiv:2511.13720*, 2025. cited on page 30.
- Li, Y., Nguyen, H. L., and Woodruff, D. P. Turnstile streaming algorithms might as well be linear sketches. In *Proceedings of the Forty-Sixth Annual ACM Symposium on Theory of Computing*, pp. 174–183, 2014. cited on page 2.

- Li, Y., Miao, R., Kim, C., and Yu, M. Flowradar: A better netflow for data centers. In *13th USENIX symposium on networked systems design and implementation (NSDI 16)*, pp. 311–324, 2016. cited on pages 16 and 19.
- Li, Y., Xu, Z., Lv, Z., Hu, Y., Cui, Y., and Yang, T. Llm-sketch: Enhancing network sketches with llm. *arXiv preprint arXiv:2502.07495*, 2025. cited on page 15.
- Liu, Y. and Xie, X. Xy-sketch: On sketching data streams at web scale. In *Proceedings of the Web Conference 2021*, pp. 1169–1180, 2021. cited on page 16.
- Lu, Y., Montanari, A., Prabhakar, B., Dharmapurikar, S., and Kabbani, A. Counter braids: A novel counter architecture for per-flow measurement. *ACM SIGMETRICS Performance Evaluation Review*, 36(1):121–132, 2008. cited on page 16.
- Lucchese, C., Orlando, S., Perego, R., and Silvestri, F. Web-docs: a real-life huge transactional dataset. In *FIMI*, volume 126, 2004. URL <http://fimi.uantwerpen.be/data/webdocs.dat.gz>. cited on page 16.
- Mai, H., Khurshid, A., Agarwal, R., Caesar, M., Godfrey, P. B., and King, S. T. Debugging the data plane with anteatr. *ACM SIGCOMM Computer Communication Review*, 41(4):290–301, 2011. cited on page 43.
- Mardani, M. and Giannakis, G. B. Estimating traffic and anomaly maps via network tomography. *IEEE/ACM transactions on networking*, 24(3):1533–1547, 2015. cited on pages 16 and 42.
- Mazziane, Y. B. and Marfoq, O. Count-min sketch with conservative updates: Worst-case analysis. *arXiv preprint arXiv:2405.12034*, 2024. cited on page 15.
- McGregor, A. Graph stream algorithms: a survey. *ACM SIGMOD Record*, 43(1):9–20, 2014. cited on page 43.
- Metwally, A., Agrawal, D., and El Abbadi, A. Efficient computation of frequent and top-k elements in data streams. In *International conference on database theory*, pp. 398–412. Springer, 2005. cited on page 15.
- Misra, J. and Gries, D. Finding repeated elements. *Science of computer programming*, 2(2):143–152, 1982. cited on page 1.
- NVIDIA, Vingelmann, P., and Fitzek, F. H. Cuda, release: 10.2.89, 2020. URL <https://developer.nvidia.com/cuda-toolkit>. cited on page 8.
- Paige, C. C. and Saunders, M. A. Lsqr: An algorithm for sparse linear equations and sparse least squares. *ACM Transactions on Mathematical Software (TOMS)*, 8(1):43–71, 1982. cited on page 38.
- Pati, Y. C., Rezaifar, R., and Krishnaprasad, P. S. Orthogonal matching pursuit: Recursive function approximation with applications to wavelet decomposition. In *Proceedings of 27th Asilomar conference on signals, systems and computers*, pp. 40–44. IEEE, 1993. cited on pages 18 and 38.
- Pinkus, A. Approximation theory of the mlp model in neural networks. *Acta numerica*, 8:143–195, 1999. cited on page 27.
- Powers, D. M. Applications and explanations of zipf’s law. In *New methods in language processing and computational natural language learning*, 1998. cited on page 4.
- Qiao, Y., Yuan, X., and Wu, K. Routing-oblivious network tomography with flow-based generative model. In *IEEE INFOCOM 2024-IEEE Conference on Computer Communications*, pp. 2139–2148. IEEE, 2024. cited on page 23.
- Rezende, D. and Mohamed, S. Variational inference with normalizing flows. In *International conference on machine learning*, pp. 1530–1538. PMLR, 2015. cited on page 5.
- Rombach, R., Blattmann, A., Lorenz, D., Esser, P., and Ommer, B. High-resolution image synthesis with latent diffusion models. In *Proceedings of the IEEE/CVF conference on computer vision and pattern recognition*, pp. 10684–10695, 2022. cited on page 5.
- Roy, P., Khan, A., and Alonso, G. Augmented sketch: Faster and more accurate stream processing. In *Proceedings of the 2016 International Conference on Management of Data*, pp. 1449–1463, 2016. cited on pages 2, 3, 6, 15, and 17.
- Sheng, S., Huang, Q., Wang, S., and Bao, Y. Pr-sketch: monitoring per-key aggregation of streaming data with nearly full accuracy. *Proceedings of the VLDB Endowment*, 14(10):1783–1796, 2021. cited on pages 3, 16, 17, and 19.
- Sun, C., Xu, K., Antichi, G., and Marina, M. K. Netgsr: Towards efficient and reliable network monitoring with generative super resolution. *Proceedings of the ACM on Networking*, 2(CoNEXT4):1–27, 2024. cited on page 16.
- Szarek, S. J. Condition numbers of random matrices. *Journal of Complexity*, 7(2):131–149, 1991. cited on page 3.
- Tang, L., Huang, Q., and Lee, P. P. Mv-sketch: A fast and compact invertible sketch for heavy flow detection in network data streams. In *IEEE INFOCOM 2019-IEEE Conference on Computer Communications*, pp. 2026–2034. IEEE, 2019. cited on page 43.

- Tang, L., Huang, Q., and Lee, P. P. Spreadsketch: Toward invertible and network-wide detection of superspreaders. In *IEEE INFOCOM 2020-IEEE Conference on Computer Communications*, pp. 1608–1617. IEEE, 2020. cited on page 15.
- Tang, N., Chen, Q., and Mitra, P. Graph stream summarization: From big bang to big crunch. In *Proceedings of the 2016 International Conference on Management of Data*, pp. 1481–1496, 2016. cited on pages 1 and 15.
- Tibshirani, R. Regression shrinkage and selection via the lasso. *Journal of the Royal Statistical Society Series B: Statistical Methodology*, 58(1):267–288, 1996. cited on page 38.
- Vardi, Y. Network tomography: Estimating source-destination traffic intensities from link data. *Journal of the American statistical association*, 91(433):365–377, 1996. cited on page 16.
- Vardi, Y. and Lee, D. From image deblurring to optimal investments: Maximum likelihood solutions for positive linear inverse problems. *Journal of the Royal Statistical Society Series B: Statistical Methodology*, 55(3):569–598, 1993. cited on page 6.
- Wang, M., Fan, Z., Wang, D., Xie, G., Li, Q., Luan, Z., Jiang, Y., Yang, T., and Xu, M. Ratiosketch: Towards more accurate frequency estimation in data streams via a lightweight neural network. 2026. cited on page 16.
- Wang, X., Liu, L., Chen, L., Li, D., Miao, Y., and Bai, Y. Resolving packets from counters: Enabling multi-scale network traffic super resolution via composable large traffic model. In *22nd USENIX Symposium on Networked Systems Design and Implementation (NSDI 25)*, pp. 1541–1561, 2025. cited on page 16.
- Wang, Y., Yu, J., and Zhang, J. Zero-shot image restoration using denoising diffusion null-space model. In *The Eleventh International Conference on Learning Representations*, 2023. cited on page 4.
- Xiong, S., Yao, Y., Cao, Q., and He, T. kbf: a bloom filter for key-value storage with an application on approximate state machines. In *IEEE INFOCOM 2014-IEEE Conference on Computer Communications*, pp. 1150–1158. IEEE, 2014. cited on page 19.
- Yan, Y., Li, F., Wang, W., and Wang, X. Talentsketch: Lstm-based sketch for adaptive and high-precision network measurement. In *2022 IEEE 30th International Conference on Network Protocols (ICNP)*, pp. 1–12. IEEE, 2022. cited on page 15.
- Yang, T., Zhou, Y., Jin, H., Chen, S., and Li, X. Pyramid sketch: A sketch framework for frequency estimation of data streams. *Proceedings of the VLDB Endowment*, 10(11):1442–1453, 2017. cited on page 15.
- Yang, T., Gong, J., Zhang, H., Zou, L., Shi, L., and Li, X. Heavyguardian: Separate and guard hot items in data streams. In *Proceedings of the 24th ACM SIGKDD International Conference on Knowledge Discovery & Data Mining*, pp. 2584–2593, 2018a. cited on pages 15 and 19.
- Yang, T., Jiang, J., Liu, P., Huang, Q., Gong, J., Zhou, Y., Miao, R., Li, X., and Uhlig, S. Elastic sketch: Adaptive and fast network-wide measurements. In *Proceedings of the 2018 Conference of the ACM Special Interest Group on Data Communication*, pp. 561–575, 2018b. cited on pages 6, 15, and 19.
- Yang, T., Wang, L., Shen, Y., Shahzad, M., Huang, Q., Jiang, X., Tan, K., and Li, X. Empowering sketches with machine learning for network measurements. In *Proceedings of the 2018 Workshop on Network Meets AI & ML*, pp. 15–20, 2018c. cited on page 15.
- Yang, T., Zhang, H., Li, J., Gong, J., Uhlig, S., Chen, S., and Li, X. Heavykeeper: an accurate algorithm for finding top- k elephant flows. *IEEE/ACM Transactions on Networking*, 27(5):1845–1858, 2019. cited on page 15.
- Yu, M., Jose, L., and Miao, R. Software {Defined}{Traffic} measurement with {OpenSketch}. In *10th USENIX symposium on networked systems design and implementation (NSDI 13)*, pp. 29–42, 2013. cited on page 15.
- Yuan, X. and Qiao, Y. Diffusion-ts: Interpretable diffusion for general time series generation. In *The Twelfth International Conference on Learning Representations*, 2024. cited on page 30.
- Yuan, X., Qiao, Y., Zhao, P., Hu, R., and Zhang, B. Traffic matrix estimation based on denoising diffusion probabilistic model. In *2023 IEEE Symposium on Computers and Communications (ISCC)*, pp. 316–322. IEEE, 2023. cited on page 31.
- Yuan, X., Qiao, Y., Wei, Z., Zhang, Z., Li, M., Zhao, P., Hu, R., and Li, W. Diffusion models meet network management: Improving traffic matrix analysis with diffusion-based approach. *IEEE Transactions on Network and Service Management*, 2025. cited on page 16.
- Yuan, X., Qiao, Y., Li, M., Wei, Z., Feng, C., Wang, Z., and Chen, W. Learning-based sketches for frequency estimation in data streams without ground truth. *IEEE Transactions on Knowledge and Data Engineering*, 2026. cited on pages 4, 16, 22, and 41.

- Zhang, M., Wang, H., Li, J., and Gao, H. Learned sketches for frequency estimation. *Information Sciences*, 507:365–385, 2020. cited on page 15.
- Zhang, Y., Roughan, M., Duffield, N., and Greenberg, A. Fast accurate computation of large-scale ip traffic matrices from link loads. *ACM SIGMETRICS Performance Evaluation Review*, 31(1):206–217, 2003a. cited on page 16.
- Zhang, Y., Roughan, M., Lund, C., and Donoho, D. An information-theoretic approach to traffic matrix estimation. In *Proceedings of the 2003 conference on Applications, technologies, architectures, and protocols for computer communications*, pp. 301–312, 2003b. cited on page 16.
- Zhang, Y., Roughan, M., Willinger, W., and Qiu, L. Spatio-temporal compressive sensing and internet traffic matrices. In *Proceedings of the ACM SIGCOMM 2009 conference on Data communication*, pp. 267–278, 2009. cited on page 16.
- Zhao, B., Li, X., Tian, B., Mei, Z., and Wu, W. Dhs: Adaptive memory layout organization of sketch slots for fast and accurate data stream processing. In *Proceedings of the 27th ACM SIGKDD Conference on Knowledge Discovery & Data Mining*, pp. 2285–2293, 2021. cited on page 15.
- Zhong, Z., Yan, S., Li, Z., Tan, D., Yang, T., and Cui, B. Burstsketch: Finding bursts in data streams. In *Proceedings of the 2021 International Conference on Management of Data*, pp. 2375–2383, 2021. cited on page 15.

Supplementary Material

A. Outline of Appendices

For ease of organization, we divide the supplementary material into appendices as follows. **Appendix B** reviews the related works and positions our study within the existing literature. **Appendix C** describes the experimental setup in detail, including datasets, baselines, and evaluation metrics. **Appendix D** presents the implementation details of FLORE, covering INN architecture, data structures, algorithms, and so on. **Appendix E** provides the complete theoretical proofs omitted from the main text. **Appendix F** provides a systematic analysis of mainstream generative models in the context of data streaming tasks. **Appendix G** reports additional experimental results that further validate the effectiveness and robustness of our approach. Finally, **Appendix H** lists some potential applications of FLORE and discusses current limitations of our approach that we hope future research can address.

B. Related Works

Classical sketching algorithms Sketches are classical streaming algorithms and compact data structures that support approximate queries over large-scale data. Because streaming data comes at them continuously, and in such volume, they try to record the essence of what they’ve seen while strategically forgetting the rest. For more than 30 years, computer scientists have worked to build a better sketching algorithm. Representative examples include Count-Min Sketch (Cormode & Muthukrishnan, 2005a) and Count Sketch (Charikar et al., 2002), which enable fast updates and queries with provable accuracy bounds. These sketches typically maintain an array of m counters organized into k rows, together with k pairwise-independent hash functions that map each item to one counter per row. For instance, in Count-Min Sketch, each update increments the k counters indexed by the hashed positions of the item. To estimate an item’s frequency, the sketch hashes the queried item and returns the minimum value among the corresponding counters across all rows. When increments are positive, a simple modification known as Conservative Update (Estan & Varghese, 2003) leads to better accuracy in frequency estimation. It avoids unnecessary increments by first comparing stored counts for an item and then only incrementing the smallest ones (Mazziane & Marfoq, 2024). Moreover, Augmented sketch (Roy et al., 2016) uses an extra elephant-flow recording structure to further improve accuracy. Due to the skewed nature of data streams, it can potentially provide even higher throughput. Based on this idea, Pyramid sketch (Yang et al., 2017), Elastic sketch (Yang et al., 2018b), HeavyGuardian (Yang et al., 2018a), HeavyKeeper (Yang et al., 2019), and Dynamic Hierarchical Sketch (Zhao et al., 2021) all store the elephant and mice flow information separately in the same space. As these sketches use the hash value as the index, they can support $\mathcal{O}(1)$ insertion and query, but they have suboptimal estimation accuracy of per-element frequency, which in turn greatly reduces the accuracy of other statistics. Additional sketches have been proposed for specialized tasks, such as burst/DDoS victim detection (Zhong et al., 2021; Yu et al., 2013), graph summarization (Tang et al., 2016), reporting top- k items (Metwally et al., 2005; Li et al., 2020), and super-spreader query (Tang et al., 2020). However, they are typically optimized for a narrow set of queries and rely on carefully engineered heuristics. By comparison, our proposal enjoys a tighter theoretical error bound while remaining applicable to a broad class of sketching tasks.

Learning-based sketching algorithms In recent years, researchers have attempted to use machine learning (ML) methods to improve sketch performance. This type of sketching algorithm was first explored by Yang et al. 2018c and Kraska et al. 2018. The former tries to learn task-specific representations, while the latter trains a classifier to distinguish frequent data items; the overall idea and architecture are consistent with Augmented Sketch. Specifically, the learning-augmented sketch uses neural networks (NN), e.g., an RNN (Hsu et al., 2019), to learn and infer whether an item is large and uses an additional lookup table to record large items. This general paradigm of leveraging ML to improve hashing-based sketches has inspired a series of follow-up works (Zhang et al., 2020; Jiang et al., 2020; Du et al., 2021; Yan et al., 2022; Cheng et al., 2023). However, because a forward pass through an ML model is required prior to each hash operation, these methods often incur substantial computational overhead, resulting in significantly reduced stream processing throughput. This issue becomes more pronounced as model complexity increases; for example, a recent study (Li et al., 2025) employs a large language model (LLM) as a learned “oracle”, which is typically impractical for high-speed data streams. Although Da Dalt et al. 2022 and Aamand et al. 2023 partially mitigate this efficiency bottleneck by reducing or even eliminating the need for per-item model inference, a second fundamental challenge remains: the reliance on continuously collected ground-truth data to train the neural models. To address this limitation, Meta-sketch (Cao et al., 2024) is the first learning-based sketch that avoids ground-truth supervision by performing meta-learning over synthetically generated Zipfian datasets. This GT-free learning paradigm has subsequently been adopted and refined in Mayfly (Feng et al., 2023), Lego-sketch (Feng et al., 2025),

Table 1. Statistics of Real-world and Synthetic Data Streams Used in the Evaluation

| Real-World | # of Keys | # of Items | Skewness | Synthetic | # of Keys | # of Items | Skewness |
|----------------|-----------|------------|----------|--------------------|-----------|------------|----------|
| <i>CAIDA</i> | 157 269 | 2 000 000 | 291.56 | <i>Zipf-icml</i> | ~ 30 000 | 1 000 000 | 24.27 |
| <i>Webdocs</i> | 125 623 | 2 000 000 | 25.42 | <i>Zipf</i> | ~ 28 000 | 1 000 000 | 125.93 |
| <i>MAWI</i> | 41 471 | 2 000 000 | 92.67 | <i>Pareto</i> | ~ 28 000 | 1 000 000 | 10.24 |
| <i>Kosarak</i> | 30 495 | 2 000 000 | 89.56 | <i>Exponential</i> | ~ 26 000 | 1 000 000 | 3.81 |
| <i>Retail</i> | 16 470 | 908 576 | 71.27 | <i>Log-Normal</i> | ~ 30 000 | 1 000 000 | 5.64 |

and RatioSketch (Wang et al., 2026). Nevertheless, beyond the open question of whether Zipfian assumptions consistently hold in real-world workloads, the neural architectures employed by these methods still exhibit much lower processing throughput compared to conventional, non-learning-based sketches. In contrast to the aforementioned sketches, our method is grounded in the theory of compressed sensing. It is both more practical and more efficient, as it requires no modification to the classical summary algorithm and relies only on sampled counters for training.

Decoding-based measurement The idea of decoding or recovery from coarse-grained, low-cost measurements obtained via linear systems can be traced back to Network Tomography (Vardi, 1996). By inferring the full end-to-end traffic matrix from more measurable link loads, this technique sparked a surge of research interest in network measurement (Zhang et al., 2003a;b; 2009; Bowden et al., 2011; Chen et al., 2014; Mardani & Giannakis, 2015; Ikeuchi & Saito, 2024; Yuan et al., 2025). However, traffic matrices are defined at the wide area network (WAN) level and are far coarser than five-tuple packet measurements via data sketching, making them unsuitable for fine-grained applications and thus beyond the scope of this work. Turning to sketching algorithms, Lee et al. 2005 were the first to apply the Least Linear Square method to reconstruct flow values from Count-Min Sketch. While Counter-Braids (Lu et al., 2008) highlighted the thematic connection between sketching and compressive sensing, it did not actually employ compressive sensing. In contrast, FlowRadar (Li et al., 2016) and SketchVisor (Huang et al., 2017) explicitly demonstrated that sketches can be formulated as a special case of compressive sensing. Specifically, they typically use a Bloom filter to record unique keys, and at the end of each measurement epoch, leverage this information to recover the complete measurement results using compressed sensing algorithms. This encoding–decoding paradigm culminated in NZE-sketch (Huang et al., 2021) and PR-sketch (Sheng et al., 2021), subsequently inspiring a line of research on sketching algorithms for high-precision measurement (Fu et al., 2020; Liu & Xie, 2021; Li et al., 2023; He et al., 2023). However, the improved accuracy of these approaches comes at the cost of query efficiency: both NZE-sketch and PR-sketch solve regularized optimization problems involving potentially millions of variables, which introduces significant complexity even with state-of-the-art numerical solvers. Our work is inspired by UCL-sketch (Yuan et al., 2026), which addresses this challenge using a learned solver. Similar to Meta-sketch, UCL-sketch relies on prior assumptions about the underlying data stream distribution. Different from them, this work leverages generative modeling to automatically infer and learn the distribution, thereby circumventing these potential limitations. Although some recent works (Sun et al., 2024; Wang et al., 2025) have introduced deep generative models, such as GANs and autoregressive models, into network monitoring tasks, they neither perform systematic theoretical or experimental analysis nor avoid reliance on large pre-collected datasets for offline training.

C. Experimental Setup

We conduct our experiments on a server equipped with an 8-core 3.80GHz CPU, 32GB RAM and a 16GB NVIDIA GeForce RTX 5060 Ti GPU. The server runs on Ubuntu 20.04, and all experiments are repeated 10 times. This section describes the experimental setup used to evaluate the proposed method. We first detail the datasets used in our experiments, followed by the introduction of baseline methods. Finally, we formulate the evaluation metrics.

C.1. Datasets

We evaluate the sketching quality of our approach on **10** datasets, comprising 5 real-world data streams and 5 synthetic data streams. The real-world datasets include: CAIDA-2018 backbone IP packet traces (CAIDA, Caida, 2018), Web document access traces (Webdocs, Lucchese et al., 2004), traffic traces from the WIDE project (MAWI, Cho et al., 2000), click-stream

data (Kosarak, Ferenc), and retail market basket data (Retail, Brijs et al., 1999). For the CAIDA and MAWI datasets, we construct 13-byte flow keys consisting of five fields: source and destination IP addresses, source and destination ports, and transport protocol. For the other datasets, item IDs are converted into 4-byte-long keys.

In addition, we generate five synthetic datasets following representative heavy-tailed distributions: *Zipf-icml*, *Zipf*, *Pareto*, *Exponential*, and *Log-Normal*. Formally, let N denote the number of distinct items, and let f_i be the frequency associated with item i , we can write

- **Zipfian Distribution.** Frequencies follow Zipf’s law $f_i \propto \frac{1}{i^\alpha}$, $i = 1, 2, \dots, N$, where $\alpha > 0$ controls the degree of skew. Note that Zipf-icml is generated by following the implementation of Du et al., 2021, i.e., $f_i \propto \lfloor \frac{N}{i^\alpha} \rfloor$, while Zipf strictly follows the aforementioned formulation with a zipfian skewness of 1.4.
- **Pareto Distribution.** Frequencies are sampled from a Pareto distribution with shape parameter $\alpha > 0$, whose CDF is given by $P(F > x) = (\frac{x_m}{x})^\alpha$, $x \geq x_m$, where x_m is the minimum value. We then draw samples $f_i \sim \text{Pareto}(\alpha)$, scale them by a constant factor, and discretize the results to obtain integer frequencies.
- **Log-Normal Distribution.** Frequencies follow a log-normal distribution, i.e., $\log f_i \sim \mathcal{N}(\mu, \sigma^2)$, where μ and σ denote the mean and standard deviation of the underlying normal distribution. The sampled frequencies are also scaled and rounded to integers.
- **Exponential Distribution.** Frequencies are generated from an exponential distribution with rate parameter $\lambda > 0$, whose density function is $p(x) = \lambda e^{-\lambda x}$, $x \geq 0$. As with the other distributions, samples are scaled and discretized to form integer-valued frequencies.

For most synthetic workloads, the resulting frequency vectors are randomly permuted to eliminate any ordering bias, and each distinct item is encoded as a fixed-length 4-byte key that appears in the stream according to its assigned frequency. Table 1 shows the important details of the datasets (i.e., the number of keys, the number of items, and the skewness of streaming data distribution).

C.2. Baselines

We implement our approach and all other algorithms in Python. We list these 9 state-of-the-art algorithms as follows:

1. **Count-Min Sketch (CM, Cormode & Muthukrishnan, 2005a):** CM maintains k pairwise independent hash functions $h_\ell : U \rightarrow [E]$ and a counter array $C \in \mathbb{R}^{k \times E}$, where $E = m/k$. Upon processing the stream, each counter is updated as $C[\ell, h_\ell(j)] = \sum f_j$. For any item $i \in U$, its frequency estimate is $\tilde{f}_i = \min_{\ell \leq k} \{C[\ell, h_\ell(i)]\}$. In our experiments, we fix $k = 4$; all subsequent sketches follow this configuration unless otherwise specified.
2. **Count Sketch (CS, Charikar et al., 2002):** Similar to CM, CS employs k hash functions $h_\ell : U \rightarrow [E]$ and a counter array $C \in \mathbb{R}^{k \times E}$. Additionally, it utilizes k independent sign hash functions $g_\ell : U \rightarrow \{-1, 1\}$. The counters are updated as $C[\ell, h_\ell(j)] = \sum f_j \cdot g_\ell(j)$, and the estimate for item i is computed as $\tilde{f}_i = \text{median}_{\ell \leq k} \{g_\ell(i) \cdot C[\ell, h_\ell(i)]\}$.
3. **Conservative Update Sketch (CU, Estan & Varghese, 2003):** As a variant of CM, CU employs a conservative update policy to maintain an upper bound on the ground truth ($\tilde{f}_i \geq f_i$). For each incoming tuple (i, v) , a counter $C[\ell, h_\ell(i)]$ is updated only if it achieves the minimum value among all k rows. Formally, $C[\ell, h_\ell(i)] \leftarrow C[\ell, h_\ell(i)] + v$ for all $\ell \in \arg \min_{j \leq k} \{C[j, h_j(i)]\}$.
4. **Augmented Sketch (AG, Roy et al., 2016):** AG utilizes the skew of the underlying stream data to improve the frequency estimation accuracy for the most frequent items by filtering them out earlier. It exchanges data items between the filter and the sketch (i.e., a CM) such that hot items are kept in the filter. We configure the filter with ~ 100 key-value pairs; this relatively small size improves accuracy while preventing lookup overhead from degrading throughput.
5. **PR-sketch (PR, Sheng et al., 2021):** PR also improves estimation accuracy by constructing linear equations that relate counter values to per-key aggregations. Solving the resulting least-squares problem requires an iterative solver. While the original implementation adopts a conjugate gradient method (Eigen Developers, 2025), we instead use LSMR (Fong & Saunders, 2011) from `scipy.sparse.linalg`. We set the number of Bloom Filter hash functions to 7. Memory is partitioned equally between the sketch and the Bloom Filter, subject to an upper bound on the latter: to ensure a false positive rate below 1%, we limit its size to $9.6N$ bits (e.g., 120 KB for $N = 100K$) as suggested by Cormode et al..

6. **NZE-sketch** (NZE, Huang et al., 2021): NZE leverages compressive sensing by constructing a fractional sensing matrix and employing a hash table for elephant element filtering. Specifically, it maintains three data structures: key-value pairs for heavy hitters, a fractional-valued sketch for small elements, and a Bloom filter. We implement the SeqSketch variant due to its superior memory efficiency, using OMP (Pati et al., 1993) for signal recovery. The configuration mirrors PR, but incorporates a hash table; we increase the hash table allocation to 75% in high-memory scenarios to reduce computational overhead during reconstruction.
7. **Learned CM Sketch** (LCM, Hsu et al., 2019): The idea of LCM is similar to AG, which is to store hot and cold elements separately. However, while AG relies on a data-exchange algorithm for classification, LCM employs a learned model. We implement an RNN-based classifier³ with a 10–20KB memory footprint for label prediction. The remaining memory budget is split equally (1:1) between the heavy-hitter (unique buckets) and light-hitter (CM) components.
8. **Learned Count Sketch** (LCS, Hsu et al., 2019): LCS follows the exact configuration of LCM but substitutes the underlying Count Min Sketch with a Count Sketch.
9. **Learned Sketch without Predictions** (LS, Aamand et al., 2023): LS extends LCS by introducing two key query-time optimizations. (i) Efficiency: To mitigate inference overhead, LS performs model predictions probabilistically rather than for every item; we set this sampling probability to 15% in our experiments. (ii) Accuracy: To improve precision for small elements, LS truncates low-value estimates to zero. The threshold is defined as $\frac{C \cdot kN}{m}$, where C is a constant (set to 10 in our experiments). Then, any query result obtained by its light part below this threshold is set to zero.

C.3. Metrics

We evaluate the performance of sketching algorithms using the following metrics. Again, all experiments are repeated 10 times and the average results are reported.

- **Average Absolute Error (AAE)**: $\frac{1}{N} \sum_i^N |f_i - \hat{f}_i|$, which measures the average magnitude of estimation errors.
- **Average Relative Error (ARE)**: $\frac{1}{N} \sum_i^N \frac{|f_i - \hat{f}_i|}{f_i}$, used to evaluate the error normalized by the true flow size. The ARE metric is highly sensitive to mouse elements, because their small true sizes reside in the denominator, even marginal overestimations yield extreme relative errors that inflate the reported mean.
- **Weighted Mean Relative Error (WMRE)**: $\frac{\sum_{j=1}^z |F_j - \hat{F}_j|}{\sum_{j=1}^z \frac{F_j + \hat{F}_j}{2}}$, where z is the maximum flow frequency, and F_j and \hat{F}_j are the true and estimated counts of elements with frequency j . This metric assesses how well the sketch preserves the overall frequency distribution.
- **Entropy Absolute Error (AE)**: $|H - \hat{H}|$, defined as the absolute difference between the true entropy H and the estimated entropy \hat{H} , where $H = -\sum_{i=1}^N \frac{f_i}{S} \log \frac{f_i}{S}$ and $S = \sum f_i$.
- **F1 Score**: $\frac{2 \cdot PR \cdot RR}{PR + RR}$, the harmonic mean of Precision (PR) and Recall (RR). Here, Recall is the ratio of correctly identified heavy hitters to the total number of true heavy hitters, and Precision is the ratio of correctly identified heavy hitters to the total number of reported instances.

Note: when the key space is unknown, traditional approaches typically rely on optimization-based methods to approximate the cardinality or distribution of data streams from counter values, such as the basic MRAC algorithm (Kumar et al., 2004). In this paper, we assume that the key space is known or can be efficiently tracked. Accordingly, for a fair comparison, all traditional algorithms are allowed to directly leverage the known keys when detecting heavy hitters or estimating distribution (i.e., computing WMRE) and entropy.

D. Implementation Details of FLORE

³The original implementation in the prior work (Hsu et al., 2019) was based on TensorFlow for IP address identification. In our implementation, we re-implement this component using PyTorch. For data streams where such correlations are absent, we directly consider an idealized setting by removing the Top-K hot keys from the stream.

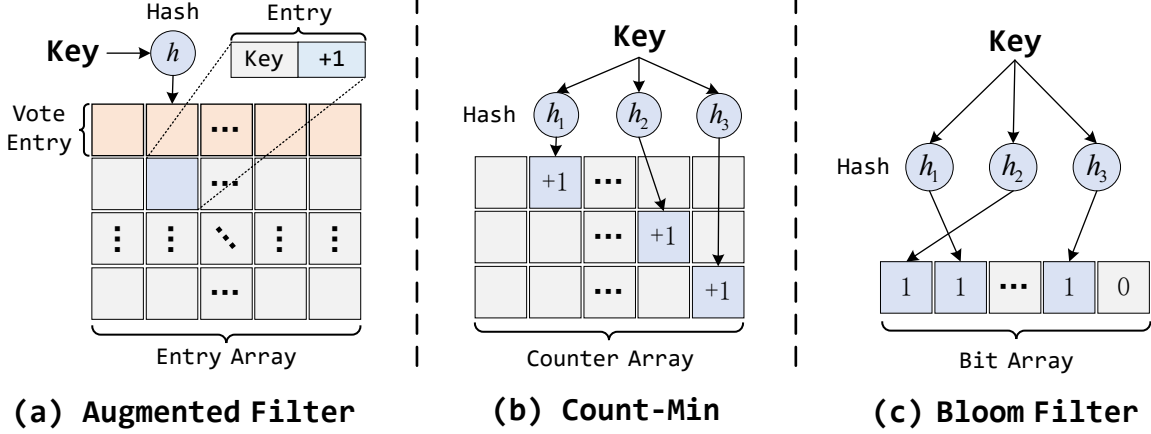


Figure 11. Data structures used in FLORE: a Bloom Filter for key tracking, a Count-Min Sketch for store infrequent items, and an augmented filter for saving frequent items as key-value pairs.

In this section, we provide additional implementation details of FLORE. As illustrated in Figure 11, the local data structure of FLORE consists of three components: (1) an augmented filter for storing frequent elements, (2) a Count-Min Sketch for recording the remaining elements, and (3) a Bloom Filter for tracking newly observed keys. We first describe the Bloom Filter-based key tracking mechanism and the stream filtering algorithm for automatically separating hot items from the data stream into the augmented filter. We then elaborate on the design of the INN employed in FGMs, and conclude with other implementation aspects, such as data preprocessing and training details.

D.1. Key Tracking Mechanism

As discussed in the main text, constructing Φ^4 requires tracking all distinct inserted keys, either during training or/and at query time (retroactively). While we do not concern ourselves with this problem and assume that the key set \mathcal{I} is known, we briefly introduce a standard key tracking mechanism commonly adopted in prior studies (Eppstein et al., 2011; Xiong et al., 2014; Li et al., 2016; Sheng et al., 2021; Huang et al., 2021) to collect \mathcal{I} from the data stream.

The mechanism consists of two parts: key identification and key recording. Specifically, key identification part maintains a lightweight data structure, i.e., a Bloom Filter, to identify keys in the summary phase (or data plane). As depicted in Figure 11(c), the Bloom filter is implemented as a one-dimensional array with m_{bf} entries and is associated with k_{bf} independent hash functions. Each entry stores a single bit indicating whether the mapped input corresponds to a key that has not been observed before. For each incoming item, we examine the bit statuses of the k_{bf} mapped entries prior to updating them. Once a new key is identified in the summary phase, it is forwarded to the recovery phase (or control plane). In the recovery phase, the key recording component stores these keys for subsequent analysis. This offloading strategy reduces the resource consumption of the key-tracking mechanism, as each unseen key is identified and transmitted at most once.

D.2. Stream Filtering Mechanism

We now describe stream filtering mechanism that serves hot keys. The strategy called *separate-and-guard-hot* (Yang et al., 2018a;b), tracks hot keys and records their information with dedicated entries. We first attempt to insert keys to the dedicated part and then evict infrequent keys to the shared part, i.e., a Count-Min. As illustrated in Figure 11(a), the augmented filter is composed of some arrays, and each array is comprised of a number of entries. In spirit to Ostracism (Greek: ostrakismos, where any citizen could be voted to be evicted from Athens for ten years), we aim to use two types of entries to store hottest items with their frequencies: the negative vote lives in the first entry, while the dedicated counters live in the other entries that consists of two fields—fingerprint (key) and counter (frequency). For each incoming tuple (k, v) , we compute a hash function to map it to a specific array. Within the selected array, we identify the entry with the minimum counter value and treat it as the positive vote. The update procedure then follows one of three cases:

- **Case 1.** A dedicated entry with a matching fingerprint is found; its counter is incremented by v .
- **Case 2.** An empty dedicated entry is found and initialized with (k, v) .

⁴We do not explicitly store the 0–1 sparse matrix Φ in memory. Instead, we generate its entries on demand during adaptation.

Algorithm 2 Stream Summary Algorithm for FLORE

Ensure: Encode tuple (k, v) into data structures of FLORE

```

 $i \leftarrow \text{Hash}(k)$ 
ARRAY  $\leftarrow$  AUGMENTEDFILTER[ $i$ ]
Lookup  $k$  in ARRAY[1 ~ end]

if Case 1: item found at position  $j$  then
    ARRAY[ $j$ ].value +  $v \rightarrow$  ARRAY[ $j$ ].value
else if Case 2: position  $j$  is empty then
     $k \rightarrow$  ARRAY[ $j$ ].key and  $v \rightarrow$  ARRAY[ $j$ ].value
else
    ARRAY[0].value +  $v \rightarrow$  ARRAY[0].value
    VOTE $^- \leftarrow$  ARRAY[0].value
     $m \leftarrow$  find minimum entry in ARRAY[1 ~ end]
    VOTE $^+ \leftarrow$  ARRAY[ $m$ ].value
    if Case 3: VOTE $^- /$  VOTE $^+ >$  THRESHOLD then
        load tuple  $(k_{ex}, v_{ex})$  from position  $m$ 
        clear entry at position  $m$ 
        add tuple  $(k, v)$  to position  $m$  (like Case 2)
        # identify and record  $k_{ex}$  with BLOOMFILTER
        insert tuple  $(k_{ex}, v_{ex})$  into COUNT-MIN
    else
        # identify and record  $k$  with BLOOMFILTER
        insert tuple  $(k, v)$  into COUNT-MIN
    end if
end if
    
```

Algorithm 3 Stream Recovery Algorithm for FLORE

Ensure: Decode all information using the model of FLORE

```

 $z \leftarrow$  sample priors from GAUSSIAN distribution
 $b \leftarrow$  flatten counters in COUNT-MIN
SKETCHVEC  $\leftarrow$  GENERATIVEMODEL( $b, z$ )
FILTERVEC  $\leftarrow$  Query(AUGMENTEDFILTER, keys)
DECODEVEC  $\leftarrow$  SKETCHVEC + FILTERVEC
return DECODEVEC and keys
    
```



Figure 12. Ostracism: the exclusion from the collective; figure is polished and excerpted from page 18 of a publicly available slide.

- **Case 3.** Otherwise, an opposing vote is cast to determine whether eviction should occur. Concretely, we increment the negative vote by v and compute the decision variable $\lambda = \frac{\text{negative vote}}{\text{positive vote}}$. If λ exceeds a predefined threshold (e.g., 8), the tuple (k, v) replaces the item in the minimum entry, and the evicted item is forwarded to the Count-Min. Otherwise, (k, v) is directly sent to the Count-Min.

The pseudo-code of the insertion procedure is provided in Algorithm 2. To query the frequency of a key, we perform a single hash operation to locate the corresponding array. If a stored fingerprint matches the queried key, the associated counter value is returned; otherwise, the query returns zero. Then, the final estimate is obtained by summing the generative model’s output and the query vector (see Algorithm 3).

D.3. INN Architecture

Building upon the foundations of prior works (Dinh et al., 2014; 2016; Kingma & Dhariwal, 2018; Ardizzone et al., 2019a), we design the FLORE architecture as a fully invertible neural network (INN). The fundamental unit of this INN is a reversible block consisting of two complementary affine coupling layers. Specifically, each block partitions its input into two components, $[u_1, u_2]$, and applies alternating affine transformations with strictly upper or lower triangular Jacobians:

$$v_1 = u_1 \odot \exp(s_1(u_2)) + t_1(u_2), \quad v_2 = u_2 \odot \exp(s_2(v_1)) + t_2(v_1).$$

Here, \odot denotes element-wise multiplication. The resulting outputs $[v_1, v_2]$ are concatenated and passed to the subsequent block. Crucially, the internal functions s_j and t_j can be represented by arbitrary neural networks and do not require invertibility themselves. In our

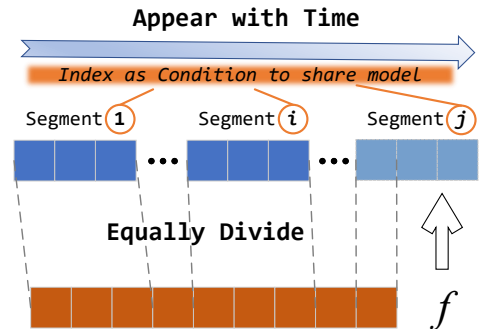


Figure 13. Illustration of our scalable design.

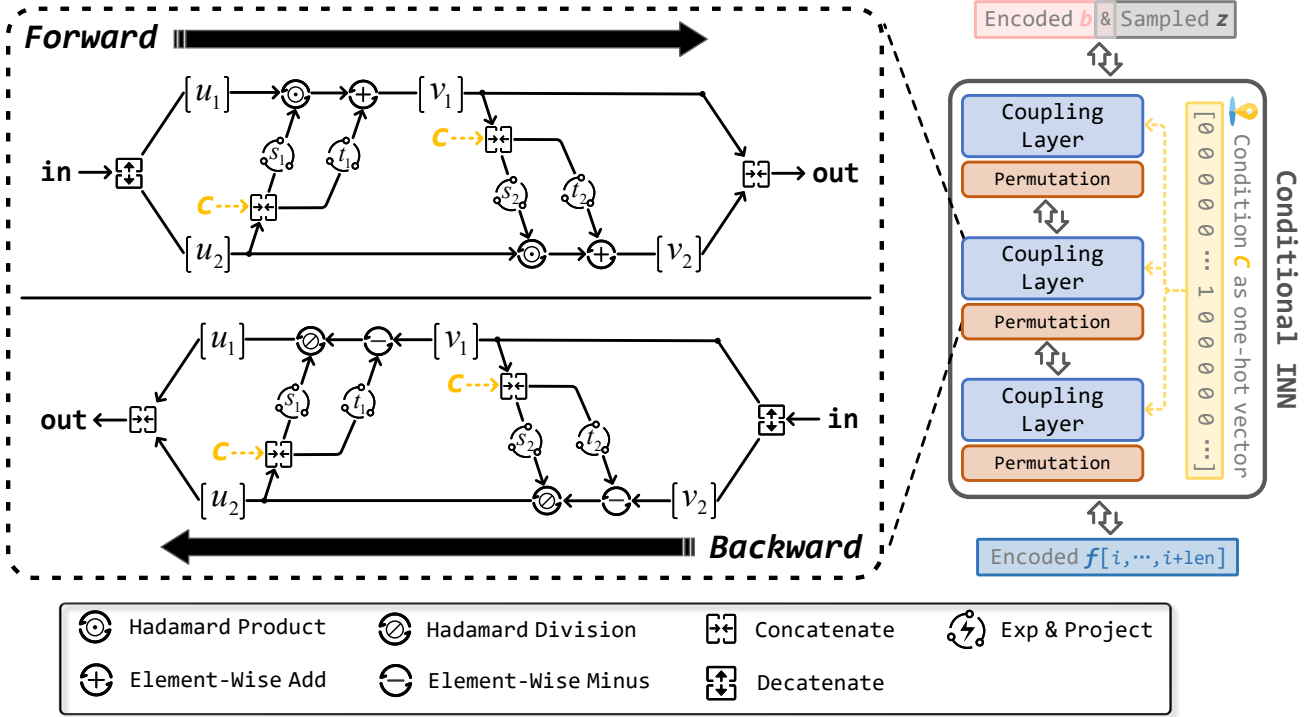


Figure 14. The underlying cINN architecture used in FLORE.

implementation, these are realized by a sequence of fully connected layers with RELU activations. Given the outputs $[v_1, v_2]$, the forward pass is analytically invertible:

$$u_2 = (v_2 - t_2(v_1)) \odot \exp(s_2(v_1)), \quad u_1 = (v_1 - t_1(u_2)) \odot \exp(s_1(u_2)).$$

Here, \odot denotes element-wise division. To enhance model capacity and ensure global dependency, we interleave permutation layers (Kingma & Dhariwal, 2018) between reversible blocks. These layers shuffle the elements of the input in a fixed, pseudo-random manner, forcing the splits $[u_1, u_2]$ to vary across layers and facilitating interaction among all variables.

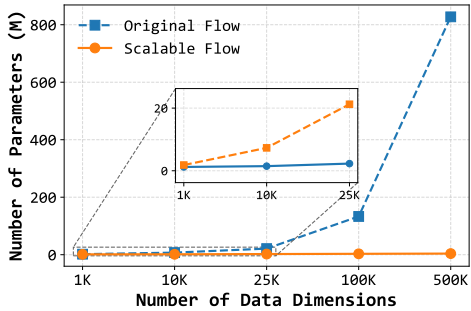


Figure 15. Model size v.s. Data stream size.

Scalable Flows As previously noted in §3.2, FLORE may support dynamic capacity expansion to accommodate streaming data recovery. Direct retraining on the continually expanded key space would incur prohibitive computational overhead, while high-dimensional data streams (often reaching millions of dimensions) would also lead to a dramatic increase in parameter count. To address these challenges, we partition the GT vector f into equal-length segments and incrementally increase the number of segments over time to adapt those new elements (see Figure 13). To maintain parameter efficiency, these segments are able to share the same network conditioned on their respective indices. Such design ensures that when the brand-new keys arrive, only the parameters associated with the most recent index require fine-tuning, thereby minimizing the impact on existing segments. As a result, the model’s parameter complexity is reduced from $\mathcal{O}(\dim(f))$ to $\mathcal{O}(\text{segment length})$. We empirically demonstrate this benefit in Figure 15 by plotting how the number of FLORE’s parameters scales with the size of the data stream (i.e., data dimensions). As can be seen, the scalable design substantially reduces the parameter count, achieving a reduction of over 200 times at 500K unique keys. In our context, this approach is implemented using a Conditional INN (cINN, Ardizzone et al., 2019b). Since the subnetworks s_j and t_j are not explicitly inverted, they can be conditioned on condition c via concatenation without compromising the overall invertibility of the block (i.e., replacing $s_1(u_2)$ with $s_1(u_2, c)$). Specifically, the index c is represented as a one-hot vector and processed by a feedforward conditioning network to extract intermediate representations, which is trained jointly with the cINN. Figure 14 illustrates the final architecture; note that two autoencoders are omitted from the diagram for clarity.

D.4. Other Details

Below, we summarize several auxiliary yet important details that complement the main methodology, covering dataset construction, normalization, retraining, and parameter settings.

D.4.1. DATASET CONSTRUCTION

First of all, FLORE eliminates the need for real samples (f) during training, facilitating online dataset construction, which requires only sketch summaries (b). Then, counters are periodically sampled at fixed intervals (defined by either the number of updates or elapsed time), which we term sampling epochs. To make the model capture the most recent data stream characteristics, we maintain a sliding window of these sampled states by following Yuan et al., 2026. This window operates on a first-in-first-out (FIFO) style, discarding stale states once its capacity is reached. In our experimental setup, we configure the sampling interval to 5,000 updates and the sliding window length to 200~500.

D.4.2. DATA NORMALIZATION

As discussed in the above dataset construction process, we do not have fixed global statistics such as the overall minimum/maximum values or mean/std, due to the evolving nature of the data stream. Therefore, instead of classical min-max normalization or mean normalization, we employ instance normalization (Du et al., 2021; Yuan et al., 2026) to mitigate the influence of the sliding window. It is noteworthy that, in FLORE’s CM with k rows and m/k counters per row, the arrival of a streaming item triggers an update to exactly one counter per row, indexed by hash functions. Then, by leveraging the non-negativity of CM, we can define a scaling factor, scale, as the minimum of the row-wise maximum values: $\text{scale} := \min_{1 \leq j \leq k} \left(\max_{1 \leq i \leq m/k} b \left[\frac{m(j-1)}{k} + i \right] \right)$. This important factor can be computed in $\mathcal{O}(m)$ linear time (often very fast), and every element in f is smaller than this constant. The normalized counters are then input into the neural network as $b' = b/\text{scale}$. At inference time, the model f_G predicts the GT vector in the normalized space, which is subsequently mapped back to the original space via: $\hat{f} = \text{scale} \cdot f_G(b')$.

D.4.3. TRAINING FLORE

Since FLORE’s generative model is trained dynamically on sampled data, its operational model can be periodically updated by the cINN fine-tuned in the background on more recent and up to date data, to gracefully adapt to *planned* changes in the database system (resetting sketch parameters, planned addition/removal of keys) and to natural drifts in data stream distributions. Our evaluation results (Appendix G.4) indicate that FLORE produces high-quality recoveries even epochs after being deployed, and even if the distribution changes during this time (e.g., due to time or/and attacks). This provides ample time for training substitute invertible functions, and one can tentatively handle previously unencountered queries using a simple algorithm such as Count-Min, since FLORE does not disrupt the original data-plane sketching operation.

D.4.4. HYPERPARAMETERS

Data-plane structural parameters. The memory allocation of FLORE follows the NZE-sketch instance. Specifically, the total memory budget is initially partitioned: 50% is allocated to the Bloom Filter, while the remaining 50% is split equally between the Count-Min Sketch and the augmented filter. Both the Bloom Filter and the CM sketch are subject to capacity constraints: a maximum false-positive rate threshold for the Bloom Filter and a hard memory cap of 256KB for the CM sketch. If either limit is reached, any residual memory budget is reallocated to the augmented filter. For CUDA (GPU) implementation of FLORE, we vary the batch size from 100K to 1M and recompile the program for each configuration to evaluate its impact on GPU insertion throughput.

Control-plane model hyperparameters. We evaluate segment lengths from the set $\{512, 1024, 2048\}$. The hidden dimension of FLORE’s f -autoencoder is selected from $\{64, 128, 256, 512\}$. For the hidden representation of b , we set its dimension to 2/3 of that of f , reserving the remaining 1/3 for concatenation with the sampled Gaussian noise vector z . The number of cINN layers is chosen from $\{2, 3, 4, 5\}$. The final layer employs a TANH activation function, consistent with the encoder’s projection of inputs into the $[-1, 1]$ range.

Training parameters. The loss trade-off coefficients α_1 through α_4 are set to (or selected from) 0.5, 0.001, 0.01, and $\{0.01, 0.05, 0.1, 0.25\}$, respectively. Notably, α_2 is assigned a near-zero value, as we observed that the INN demonstrates near-perfect invertibility even without strong regularization. The initial training phase consists of 20~30 epochs, while subsequent fine-tuning to incorporate new elements needs 3~5 epochs. By default, the MMD metric is used to measure the loss term \mathcal{L}_{ort} , and the Adam optimizer (Kingma, 2014) is employed throughout all experiments.

Table 2. Summary of Main Notations

| Symbol | Description | Symbol | Description |
|---------------|--|----------------------------|---|
| f | Ground-truth (frequency) vector | Φ | Linear sketching matrix |
| b | Measurement (counters) vector | k | Number of hash functions in sketch |
| z | Prior (Gaussian) vector | N | Number of distinct items |
| \mathcal{I} | Key set of data stream | m | Number of total counters in sketch |
| T_i | i -th invertible transformation function | (ε, ς) | Coefficient & error probability of sketch |
| ϵ | Error introduced by missing elements | m_{bf} | Number of bits in Bloom Filter |
| s | Non-zero count upper bound | k_{bf} | Number of hash functions in Bloom Filter |
| $p_B(\cdot)$ | Distribution of counters | $p_Z(\cdot)$ | Distribution of priors |
| $p_F(\cdot)$ | Distribution of ground truth | $q(\cdot)$ | Joint distribution of counters and priors |

E. Theoretical Proofs

This section develops the theoretical analyses underlying the main results of the paper. We establish rigorous analyses for the linear sketching problem. We first introduce the necessary definitions and notations, followed by the derivation of the main lemmas and theorems. Parts of our proofs leverage and extend ideas from prior works (Candes & Tao, 2005; Candes, 2008; Chandar, 2008; Gretton et al., 2012; Ardizzone et al., 2019a; Foucart & Rauhut, 2022; Qiao et al., 2024).

E.1. Preliminaries

Notations. In Table 2, we list the notational conventions used in this paper.

Definition E.1. (*Support*) For a vector $\mathbf{x} \in \mathbb{R}^n$, the set of all indices of non-zero elements in \mathbf{x} is called the support of x , denoted as $\text{supp}(\mathbf{x}) : \text{supp}(\mathbf{x}) = \{i : \mathbf{x}_i \neq 0\}$.

Definition E.2. (*Sparsity*) The sparsity of \mathbf{x} = the number of non-zero element in \mathbf{x} = the cardinality of $\text{supp}(\mathbf{x})$. It can be denoted as $|\text{supp}(\mathbf{x})|$ or $\|\mathbf{x}\|_0$. A vector x is s -sparse if $\|\mathbf{x}\|_0 \leq s$.

Definition E.3. (*s -term Approximation*) For $p > 0$, the ℓ_p -error of best s -term approximation to a vector $\mathbf{x} \in \mathbb{C}^N$ is defined by $\sigma_s(\mathbf{x})_p := \inf \left\{ \|\mathbf{x} - \mathbf{z}\|_p, \mathbf{z} \in \mathbb{C}^N \text{ is } s\text{-sparse} \right\}$.

Definition E.4. (*Restricted Isometry Constant*) The s -th restricted isometry constant $\delta_s = \delta_s(\mathbf{A})$ of a matrix $\mathbf{A} \in \mathbb{C}^{m \times N}$ is the smallest number $\delta_s \geq 0$, such that $(1 - \delta_s)\|\mathbf{x}\|_2^2 \leq \|\mathbf{A}\mathbf{x}\|_2^2 \leq (1 + \delta_s)\|\mathbf{x}\|_2^2$ holds for all s -sparse vectors $\mathbf{x} \in \mathbb{C}^N$. Equivalently, it is given by $\delta_s = \max_{S \subseteq [N], \text{card}(S) \leq s} \|\mathbf{A}_S^* \mathbf{A}_S - \mathbf{I}_d\|_{2 \rightarrow 2}$, where \mathbf{A}_S^* is the hermitian transpose of \mathbf{A}_S and $\text{card}(S)$ is the cardinality of set S .

Definition E.5. (*Kullback–Leibler Divergence*) The Kullback–Leibler (KL) divergence is a type of statistical distance: a measure of how much an approximating probability distribution q is different from a true probability distribution p . Mathematically, it is defined as $\mathcal{D}_{\text{KL}}(p \parallel q) = \sum_{x \in \mathcal{X}} p(x) \log \frac{p(x)}{q(x)}$. Obviously, $\mathcal{D}_{\text{KL}}(p \parallel q) \geq 0$ and equals zero if and only if $p = q$ as measures.

Definition E.6. (*Maximum Mean Discrepancy*) Let x and y be random variables defined on a topological space X , with respective Borel probability measures p and q . And let \mathcal{F} be a class of functions $F : \mathcal{X} \rightarrow \mathbb{R}$. We define the maximum mean discrepancy (MMD) as $\text{MMD}[\mathcal{F}, p, q] := \sup_{F \in \mathcal{F}} (\mathbb{E}_x[F(x)] - \mathbb{E}_y[F(y)])$.

E.2. Useful Lemmas

Lemma E.7. Let $\mathbf{u}, \mathbf{v} \in \mathbb{C}^N$ be vectors such that $\|\mathbf{u}\|_0 \leq s$ and $\|\mathbf{v}\|_0 \leq t$. Assume that their supports are disjoint, i.e., $\text{supp}(\mathbf{u}) \cap \text{supp}(\mathbf{v}) = \emptyset$. Then $|\langle \mathbf{A}\mathbf{u}, \mathbf{A}\mathbf{v} \rangle| \leq \delta_{s+t} \|\mathbf{u}\|_2 \|\mathbf{v}\|_2$, where δ_{s+t} is the isometry constant of matrix \mathbf{A} .

Proof. Let $S := \text{supp}(\mathbf{u}) \cup \text{supp}(\mathbf{v})$, so that $|S| \leq s + t$. Denote by $\mathbf{u}_S, \mathbf{v}_S \in \mathbb{C}^{|S|}$ the restrictions of \mathbf{u} and \mathbf{v} to the index set S , and by \mathbf{A}_S the submatrix of \mathbf{A} consisting of the columns indexed by S . Then $\mathbf{A}\mathbf{u} = \mathbf{A}_S \mathbf{u}_S$ and $\mathbf{A}\mathbf{v} = \mathbf{A}_S \mathbf{v}_S$. Since $\text{supp}(\mathbf{u}) \cap \text{supp}(\mathbf{v}) = \emptyset$, we have $\langle \mathbf{u}_S, \mathbf{v}_S \rangle = 0$. Therefore,

$$|\langle \mathbf{A}\mathbf{u}, \mathbf{A}\mathbf{v} \rangle| = |\langle \mathbf{A}_S \mathbf{u}_S, \mathbf{A}_S \mathbf{v}_S \rangle - \langle \mathbf{u}_S, \mathbf{v}_S \rangle| = |\langle (\mathbf{A}_S^* \mathbf{A}_S - \mathbf{I}) \mathbf{u}_S, \mathbf{v}_S \rangle|.$$

Applying the Cauchy–Schwarz inequality yields

$$|\langle (\mathbf{A}_S^* \mathbf{A}_S - \mathbf{Id}) \mathbf{u}_S, \mathbf{v}_S \rangle| \leq \|\mathbf{A}_S^* \mathbf{A}_S - \mathbf{Id}\|_{2 \rightarrow 2} \|\mathbf{u}_S\|_2 \|\mathbf{v}_S\|_2.$$

By the RIP of order $s + t$, i.e., Definition E.4, we have $\|\mathbf{A}_S^* \mathbf{A}_S - \mathbf{Id}\|_{2 \rightarrow 2} \leq \delta_{s+t}$. Finally, noting that $\|\mathbf{u}_S\|_2 = \|\mathbf{u}\|_2$ and $\|\mathbf{v}_S\|_2 = \|\mathbf{v}\|_2$, we obtain $|\langle \mathbf{A} \mathbf{u}, \mathbf{A} \mathbf{v} \rangle| \leq \delta_{s+t} \|\mathbf{u}\|_2 \|\mathbf{v}\|_2$, which completes the proof. \square

Lemma E.8. *For any $x \in (0, 1)$, we have that $\sqrt{x+1} < 1 + (\sqrt{2} + 1)x$.*

Proof. Let $g(x) = (\sqrt{2} + 1)x - \sqrt{x+1} + 1$. Then, $g'(x) = \sqrt{2} + 1 - \frac{1}{2\sqrt{x+1}}$. Also, $g(0) = 0$, $g(1) = 2$, and $g'(x) > 0$ for any $x \in (0, 1)$. Therefore, $\sqrt{x+1} < 1 + (\sqrt{2} + 1)x$, $\forall x \in (0, 1)$. \square

Lemma E.9. *Let $\mathbf{x} \in \mathbb{R}^N$ be an s -sparse vector, and $\mathbf{A} \in \mathbb{R}^{m \times N}$ be a random dense matrix drawn from the Gaussian matrix ensemble. Let $\varepsilon \in (0, 1)$. If*

$$\frac{m^2}{m+1} \geq 2s \left(\sqrt{\ln(2.34N/s)} + \sqrt{\frac{\ln(\varepsilon^{-1})}{s}} \right)^2 \quad (3)$$

then with probability at least $1 - \varepsilon$, \mathbf{x} is the unique minimizer of $\|\mathbf{z}\|_1$ subject to $\mathbf{A}\mathbf{x} = \mathbf{A}\mathbf{z}$.

Proof. This lemma is a direct application of Theorem 9.16 from page 258 of Foucart & Rauhut 2022. \square

Lemma E.10. *Let \mathcal{F} be a unit ball in a universal reproducing kernel Hilbert space \mathcal{H} , defined on the compact metric space \mathcal{X} , with associated continuous kernel $k(\cdot, \cdot)$. Then $\text{MMD}[\mathcal{F}, p, q] = 0$ if and only if $p = q$.*

Proof. The original proof can be found in Gretton et al. 2012 (see its Theorem 5). \square

E.3. Proof of Proposition 2.1

Proof. We first partition the vector f into a sequence of vectors $f_{\mathcal{T}_k}$ based on the magnitudes of its entries. Specifically, let $f_{\mathcal{T}_0}$ retain the s largest entries of f in magnitude (with all others set to 0), $f_{\mathcal{T}_1}$ retain the next s largest entries, and so forth. Given $f = f^* + h$, at a high level, our proof separately provides upper bounds for $\|h_{\mathcal{T}_{0 \cup 1}}\|_2$ and $\|h_{\mathcal{T}_{0 \cup 1}^c}\|_2$, thereby bounding our target $\|f^* - f\|_2 = \|h\|_2$ (i.e., the sum of these two terms). According to the above definition, we can write

$$\|h_{\mathcal{T}_j}\|_2 = \sqrt{\sum_i h_{\mathcal{T}_j}^2(i)} \leq \sqrt{s \max_i h_{\mathcal{T}_j}^2(i)} \leq \sqrt{\frac{1}{s} \sum_i h_{\mathcal{T}_{j-1}}(i)} = \sqrt{\frac{1}{s}} \|h_{\mathcal{T}_{j-1}}\|_1,$$

which holds for $j \geq 2$. Based on this, we have $\sum_{j \geq 2} \|h_{\mathcal{T}_j}\|_2 \leq \frac{1}{\sqrt{s}} \sum_{j \geq 1} \|h_{\mathcal{T}_j}\|_1 = \frac{1}{\sqrt{s}} \|h_{\mathcal{T}_0^c}\|_1$. Then the following useful inequality can be further derived:

$$\|h_{\mathcal{T}_{0 \cup 1}^c}\|_2 = \left\| \sum_{j \geq 2} h_{\mathcal{T}_j} \right\|_2 \leq \sum_{j \geq 2} \|h_{\mathcal{T}_j}\|_2 \leq \frac{1}{\sqrt{s}} \sum_{j \geq 1} \|h_{\mathcal{T}_j}\|_1 = \frac{1}{\sqrt{s}} \|h_{\mathcal{T}_0^c}\|_1 \quad (4)$$

Since f^* minimizes $\|f^*\|_1$ subject to the constraint $\Phi f^* = \Phi f + \epsilon$, i.e., $\min_{\Phi f^* = b} \|f^*\|_p$, it is intuitively clear that $\|f^*\|_1$ cannot exceed $\|f\|_1$. Hence, we have $\|f\|_1 \geq \|f^*\|_1$, which leads to

$$\begin{aligned} \|f_{\mathcal{T}_0}\|_1 + \|f_{\mathcal{T}_0^c}\|_1 &= \|f\|_1 \geq \|f^*\|_1 = \|f - h\|_1 = \|(f - h)_{\mathcal{T}_0}\|_1 + \|(f - h)_{\mathcal{T}_0^c}\|_1 \\ &\geq \|f_{\mathcal{T}_0}\|_1 - \|h_{\mathcal{T}_0}\|_1 + \|h_{\mathcal{T}_0^c}\|_1 - \|f_{\mathcal{T}_0^c}\|_1. \end{aligned}$$

To this end, we get $\|h_{\mathcal{T}_0^c}\|_1 \leq 2 \|f_{\mathcal{T}_0^c}\|_1 + \|h_{\mathcal{T}_0}\|_1$. Combining with Ineq. (4), it gives the first upper bound

$$\|h_{\mathcal{T}_{0 \cup 1}^c}\|_2 \leq \frac{1}{\sqrt{s}} \|h_{\mathcal{T}_0^c}\|_1 \leq \frac{1}{\sqrt{s}} \|h_{\mathcal{T}_0}\|_1 + \frac{2}{\sqrt{s}} \|f_{\mathcal{T}_0^c}\|_1 \quad (5)$$

We now continue to derive an upper bound for the other term, $\|h_{\mathcal{T}_{0\cup 1}}\|_2$. By applying the Cauchy–Schwarz inequality, we obtain the following inequality:

$$\begin{aligned} \|\Phi(f^* - f)\|_2^2 &= \langle \Phi f^* - b + b - \Phi f, \Phi f^* - b + b - \Phi f \rangle \\ &= \|\Phi f^* - b\|_2^2 + \|b - \Phi f\|_2^2 + 2|\langle \Phi f^* - b, b - \Phi f \rangle| \\ &\leq \|\Phi f^* - b\|_2^2 + \|b - \Phi f\|_2^2 + 2\|\Phi f^* - b\|_2 \|b - \Phi f\|_2 \\ &= (\|\Phi f^* - b\|_2 + \|b - \Phi f\|_2)^2 \end{aligned}$$

Therefore,

$$\|\Phi h\|_2 = \|\Phi(f^* - f)\|_2 \leq \|\Phi f^* - b\|_2 + \|b - \Phi f\|_2 \leq 2\|\epsilon\|_2 \leq 2\eta$$

Here we again apply the Cauchy–Schwarz inequality together with Definition E.4 to get:

$$|\langle \Phi h_{\mathcal{T}_{0\cup 1}}, \Phi h \rangle| \leq \|\Phi h_{\mathcal{T}_{0\cup 1}}\|_2 \|\Phi h\|_2 \leq 2\eta\sqrt{1 + \delta_{2s}} \|h_{\mathcal{T}_{0\cup 1}}\|_2$$

By Lemma E.7, we have

$$\begin{cases} |\langle \Phi h_{\mathcal{T}_0}, \Phi h_{\mathcal{T}_j} \rangle| \leq \delta_{2s} \|h_{\mathcal{T}_0}\|_2 \|h_{\mathcal{T}_j}\|_2, & \forall j \in \{1, 2, \dots\}, \\ |\langle \Phi h_{\mathcal{T}_1}, \Phi h_{\mathcal{T}_j} \rangle| \leq \delta_{2s} \|h_{\mathcal{T}_1}\|_2 \|h_{\mathcal{T}_j}\|_2, & \forall j \in \{0, 2, \dots\}. \end{cases}$$

Thus, using the inequality $\|h_{\mathcal{T}_0}\|_2 + \|h_{\mathcal{T}_1}\|_2 \leq \sqrt{2} \|h_{\mathcal{T}_{0\cup 1}}\|_2$, we obtain

$$\begin{aligned} \|\Phi h_{\mathcal{T}_{0\cup 1}}\|_2^2 &= \langle \Phi h_{\mathcal{T}_{0\cup 1}}, \Phi l \rangle - \left\langle \Phi h_{\mathcal{T}_{0\cup 1}}, \sum_{j \geq 2} \Phi h_{\mathcal{T}_j} \right\rangle \leq 2\eta\sqrt{1 + \delta_{2s}} \|h_{\mathcal{T}_{0\cup 1}}\|_2 - \left\langle \Phi h_{\mathcal{T}_0} + \Phi h_{\mathcal{T}_1}, \sum_{j \geq 2} \Phi h_{\mathcal{T}_j} \right\rangle \\ &\leq 2\eta\sqrt{1 + \delta_{2s}} \|h_{\mathcal{T}_{0\cup 1}}\|_2 + \delta_{2s} (\|h_{\mathcal{T}_0}\|_2 + \|h_{\mathcal{T}_1}\|_2) \sum_{j \geq 2} \|h_{\mathcal{T}_j}\|_2 \\ &\leq 2\eta\sqrt{1 + \delta_{2s}} \|h_{\mathcal{T}_{0\cup 1}}\|_2 + \sqrt{2}\delta_{2s} \|h_{\mathcal{T}_{0\cup 1}}\|_2 \sum_{j \geq 2} \|h_{\mathcal{T}_j}\|_2. \end{aligned}$$

Moreover, since $(1 - \delta_{2s}) \|h_{\mathcal{T}_{0\cup 1}}\|_2^2 \leq \|\Phi h_{\mathcal{T}_{0\cup 1}}\|_2^2$, revisiting Ineq. (4) yields:

$$\|h_{\mathcal{T}_{0\cup 1}}\|_2 \leq \frac{2\sqrt{1 + \delta_{2s}}}{1 - \delta_{2s}} \eta + \frac{\sqrt{2}\delta_{2s}}{1 - \delta_{2s}} \sum_{j \geq 2} \|h_{\mathcal{T}_j}\|_2 \leq \frac{2\sqrt{1 + \delta_{2s}}}{1 - \delta_{2s}} \eta + \frac{\sqrt{2}\delta_{2s}}{\sqrt{s}(1 - \delta_{2s})} \|h_{\mathcal{T}_0^c}\|_1$$

Combining this further with inequality $\|h_{\mathcal{T}_0^c}\|_1 \leq 2\|f_{\mathcal{T}_0^c}\|_1 + \|h_{\mathcal{T}_0}\|_1$ established earlier, we have

$$\|h_{\mathcal{T}_{0\cup 1}}\|_2 \leq \frac{2\sqrt{1 + \delta_{2s}}}{1 - \delta_{2s}} \eta + \frac{\sqrt{2}\delta_{2s}}{\sqrt{s}(1 - \delta_{2s})} \|h_{\mathcal{T}_0}\|_1 + \frac{2\sqrt{2}\delta_{2s}}{\sqrt{s}(1 - \delta_{2s})} \|f_{\mathcal{T}_0^c}\|_1.$$

It should also be noted that $\|h_{\mathcal{T}_0}\|_1 \leq \sqrt{s} \|h_{\mathcal{T}_0}\|_2 \leq \sqrt{s} \|h_{\mathcal{T}_{0\cup 1}}\|_2$, which also follows from the Cauchy–Schwarz inequality, as shown in the following derivation:

$$\frac{1}{\sqrt{s}} \|h_{\mathcal{T}_0}\|_1 = \sqrt{\left(\sum_i \frac{1}{\sqrt{s}} |h_{\mathcal{T}_0}(i)| \right)^2} \leq \sqrt{\left(\sum_{j=1}^s \frac{1}{s} \right) \sum_i h_{\mathcal{T}_0}^2(i)} = \|h_{\mathcal{T}_0}\|_2 \leq \|h_{\mathcal{T}_{0\cup 1}}\|_2$$

Thus, further, we have

$$\begin{aligned} \|h_{\mathcal{T}_{0\cup 1}}\|_2 &\leq \frac{2\sqrt{1 + \delta_{2s}}}{1 - \delta_{2s}} \eta + \frac{\sqrt{2}\delta_{2s}}{1 - \delta_{2s}} \|h_{\mathcal{T}_{0\cup 1}}\|_2 + \frac{2\sqrt{2}\delta_{2s}}{\sqrt{s}(1 - \delta_{2s})} \|f_{\mathcal{T}_0^c}\|_1 \\ &\leq \frac{2\sqrt{1 + \delta_{2s}}}{1 - (\sqrt{2} + 1)\delta_{2s}} \eta + \frac{2\sqrt{2}\delta_{2s}}{\sqrt{s} - \sqrt{s}(\sqrt{2} + 1)\delta_{2s}} \|f_{\mathcal{T}_0^c}\|_1 \end{aligned} \tag{6}$$

Now using the first upper bound as in Ineq. (5), we can write

$$\|f^* - f\|_2 = \|h\|_2 \leq \|h_{\mathcal{T}_{0 \cup 1}}\|_2 + \|h_{\mathcal{T}_{0^c \cup 1}}\|_2 \leq 2\|h_{\mathcal{T}_{0 \cup 1}}\|_2 + \frac{2}{\sqrt{s}} \|f_{\mathcal{T}_0^c}\|_1.$$

Finally, Substituting into the Ineq. (6), we see that

$$\|f^* - f\|_2 = \|h\|_2 \leq \frac{2 + (2\sqrt{2} + 2)\delta_{2s}}{\sqrt{s} - \sqrt{s}(\sqrt{2} + 1)\delta_{2s}} \|f_{\mathcal{T}_0^c}\|_1 + \frac{4\sqrt{1 + \delta_{2s}}}{1 - (\sqrt{2} + 1)\delta_{2s}} \eta$$

Let $\rho = (\sqrt{2} + 1)\delta_{2s}$; then the above expression can be rewritten as

$$\|f^* - f\|_2 \leq \frac{2(1 + \rho)}{\sqrt{s}(1 - \rho)} \|f_{\mathcal{T}_0^c}\|_1 + \frac{4\sqrt{1 + \delta_{2s}}}{1 - \rho} \eta \leq \frac{2(1 + \rho)}{\sqrt{s}(1 - \rho)} \|f_{\mathcal{T}_0^c}\|_1 + \frac{4(1 + \rho)}{1 - \rho} \eta,$$

where the second inequality is by Lemma E.8. And by Definition E.3, $\sigma_s(f)_1$ is the minimum ℓ_1 -error over all s -sparse approximations of f . Since $f_{\mathcal{T}_0}$ retains the s largest entries of f in magnitude, $\sigma_s(f)_1 = \|f - f_{\mathcal{T}_0}\|_1 = \|f_{\mathcal{T}_0^c}\|_1$. Hence, $\|f^* - f\|_2 \leq Cs^{-1/2}\sigma_s(f)_1 + 2C\eta$, where $C = \frac{2(1+\rho)}{1-\rho}$. This concludes the proof. \square

E.4. Proof of Theorem 2.2

Proof. Clearly, our proof is divided into two parts, establishing the lower bounds for the 0-1 sparse and random dense cases separately. Without loss of generality, we further emphasize that these two cases specifically refer to the count-min and Gaussian settings; that is, in the 0-1 matrix, each column contains exactly k (determined by the number of hash functions) 1's. Before we prove the first case, we need to introduce the following variant of RIP: there exists $c > 0$ such that for all s -sparse vector $f \in \mathbb{R}^N$, $c\|\Phi f\|_2 \leq \|f\|_2 \leq cD\|\Phi f\|_2$.

① **Φ is 0-1 sparse matrix.** To start, we square the new RIP inequality to obtain $c^2\|\Phi f\|_2^2 \leq \|f\|_2^2 \leq c^2D^2\|\Phi f\|_2^2$. We can bound c by considering the 1-sparse vector $f = e_i$, where e_i is a standard basis vector with a 1 in a coordinate corresponding to a column of Φ with k 1's. Then, the inequalities above give $c^2k \leq 1 \leq c^2D^2k$. We will only need the right inequality, which we rewrite as $\frac{1}{c^2} \leq D^2k$.

Now, consider the vector f with 1's in the first s positions and 0's elsewhere, i.e., $f = \sum_{i=1}^s e_i$. Let w_i denote the number of 1's in row i and in the first s columns of Φ . Then, since the first s columns of Φ contain ks 1's, we can write $\sum_i w_i \geq ks$. Applying the Cauchy-Schwarz inequality, we obtain

$$\|\Phi f\|_2^2 = \sum_{i=1}^m w_i^2 \geq \frac{(\sum_{i=1}^m w_i)^2}{m} \geq \frac{(ks)^2}{m}, \text{ but } \|\Phi f\|_2^2 \leq \frac{\|f\|_2^2}{c^2} \leq D^2ks,$$

so putting the two inequalities together gives $\frac{(ks)^2}{m} \leq D^2ks$. Cancelling out ks from both sides gives $\frac{k}{m} \leq \frac{D^2}{s}$.

Also, let r be the maximum number of 1's in any row of Φ . By permuting the rows and columns of Φ , we may assume that $\Phi_{1,i} = 1$ for $1 \leq i \leq r$, i.e., that the first row of Φ has a 1 in the first r entries. In the following proof, we assume that this reordering has already been done. We can now obtain a second bound on $\frac{k}{m}$ from the obvious inequality: $kN \leq \text{number of 1's in } \Phi \leq rm$, and thus, $\frac{k}{m} \leq \frac{r}{n}$.

For notational convenience, let $\tau = \min\{r, s\}$. Consider the vector f with 1's in the first τ positions and 0's elsewhere, i.e., $f = \sum_{i=1}^{\tau} e_i$. For this choice of f , we see that $\|\Phi f\|_2^2 \geq \tau^2$ because the first entry of Φf is τ . Note that because $\tau \leq s$, the inequalities defining the new RIP apply to f . Thus, we can apply $\frac{1}{c^2} \leq D^2k$ to get $\tau^2 \leq \|\Phi f\|_2^2 \leq \frac{\|f\|_2^2}{c^2} \leq D^2k\tau$.

We now plug in our two bounds on $\frac{k}{m}$. If $r > s$, then $\tau = s$, and we use the bound $\frac{k}{m} \leq \frac{D^2}{s}$. This gives $s^2 \leq D^2\frac{D^2}{s}ms$, so $m \geq \frac{s^2}{D^4}$. Similarly, if $r \leq s$, then $\tau = r$, so using our second bound on $\frac{k}{m}$ gives $r^2 \leq D^2\frac{r}{N}mr$. Therefore, in this case $m \geq \frac{N}{D^2}$. Putting the two bounds together, $m \geq \min\left\{\frac{s^2}{D^4}, \frac{N}{D^2}\right\}$, or we can say that $m \geq \mathcal{O}(s^2)$.

② **Φ is random dense matrix.** Based on Lemma E.9, we consider the asymptotic regime where $N, s, m \rightarrow \infty$. The left-hand side of Ineq. (3) satisfies $\frac{m^2}{m+1} \approx m$ for large m . On the right-hand side, since N/s is large, we have $\ln(2.34N/s) = \ln(N/s) + O(1) \approx \ln(N/s)$. Furthermore, as s grows, the term $\frac{\ln(\epsilon^{-1})}{s}$ becomes negligible and vanishes in the limit. Substituting these approximations back into the inequality yields $m \gtrsim 2s(\sqrt{\ln(N/s)})^2$, which simplifies to the lower bound $m \geq 2s \ln(N/s)$, or we can say that $\mathcal{O}(s \log(N/s))$, ending the proof. \square

E.5. Proof of Proposition 2.3

Proof. Before decomposing the vector f , we first perform a singular value decomposition (SVD) of the sketching matrix Φ : $\Phi = U\Sigma V^\top$. Here, $U \in \mathbb{R}^{m \times m}$ and $V \in \mathbb{R}^{N \times N}$ are orthogonal matrices, and $\Sigma \in \mathbb{R}^{m \times N}$ is a rectangular diagonal matrix whose diagonal entries are the singular values of Φ , arranged in descending order. Let the rank of Φ be r . According to the properties of SVD, the orthogonal matrix V can be written as $V = [\psi, \phi]$, where $\psi = \psi_1, \psi_2, \dots, \psi_r \in \mathbb{R}^{N \times r}$ forms an orthonormal basis for the range-space of Φ , and $\phi = \phi_1, \phi_2, \dots, \phi_{N-r} \in \mathbb{R}^{N \times (N-r)}$ forms an orthonormal basis for the null-space of Φ .

Now define $f_\Phi = \psi\psi^\top f$ and $f_N = \phi\phi^\top f$. Note that

$$f_\Phi + f_N = \psi\psi^\top f + \phi\phi^\top f = (\psi\psi^\top + \phi\phi^\top)f = VV^\top f = f$$

Hence, f can be decomposed into two components, f_Φ and f_N . Since $f = f_\Phi + f_N$, left-multiplying both sides by Φ yields $\Phi f = \Phi f_\Phi + \Phi f_N$. And because $f_N = \phi\phi^\top f$ and ϕ is a basis of the null-space of Φ , we have $\Phi f_N = \Phi\phi\phi^\top f = 0$, and therefore $\Phi f_\Phi = \Phi f = b$. Thus, f_Φ and f_N correspond to the components of f lying in the range-space and the null-space of Φ , respectively. Moreover,

$$f_\Phi^\top f_N = (\phi\phi^\top f)^\top, \quad \phi\phi^\top f = f^\top \psi(\psi^\top \phi)\phi^\top f = 0$$

Therefore, f_Φ and f_N are orthogonal and uncorrelated, which completes the proof. \square

E.6. Proof of Theorem 3.1

Proof. This subsection continues the proof of Proposition 2.3; thus, there is conceptual overlap, and unless otherwise stated, the used notation is consistent with the preceding discussion.

We first notice that $b = \Phi f_\Phi = U\Sigma V^\top f_\Phi$. Recalling that $V^\top = [\psi, \phi]$, and using the facts that $\psi^\top \psi = \text{Id}$ and $\phi^\top \phi = 0$, this expression can be further expanded as $\begin{pmatrix} \Sigma_{\leq r}^{-1} U_{\leq r}^\top b \\ \mathbf{0} \end{pmatrix} = V^\top f_\Phi$, where $\Sigma_{\leq r} \in \mathbb{R}^{r \times r}$ is the diagonal matrix consisting of the top r singular values of Φ , $\Sigma_{\leq r}^{-1}$ is its inverse, $U_{\leq r}^\top \in \mathbb{R}^{r \times m}$ denotes the first r rows of U^\top , and $\mathbf{0}$ is the zero vector. Since V^\top is full rank, there exists a one-to-one correspondence between f_Φ and $\bar{b} = U_{\leq r}^\top b$.

Next, we show that b and \bar{b} are also in one-to-one correspondence. Analogous to V , we can rewrite U^\top as $U^\top = [\psi', \phi']$, where $\psi' = U_{\leq r}^\top$ forms an orthonormal basis for the column space of Φ , and ϕ' spans the null space of Φ^\top . Since for all possible f , the vector b always lies in the column space of Φ , we have $U^\top b = \begin{pmatrix} \psi' b \\ \mathbf{0} \end{pmatrix} = \begin{pmatrix} \bar{b} \\ \mathbf{0} \end{pmatrix}$. Since U^\top is full rank, there exists a one-to-one correspondence between b and \bar{b} . To this end, b is uniquely associated with both \bar{b} and f_Φ .

Similarly, left-multiplying the identity $f = f_\Phi + f_N$ by ϕ^\top yields $\phi^\top f = \phi^\top f_\Phi + \phi^\top f_N = \phi^\top f_N =: Z \in \mathbb{R}^{N-r}$. We then perform an SVD of ϕ^\top , denoted by $\phi^\top = U'\Sigma'V'^\top$. Since the rank of ϕ^\top is $N-r$, its singular value matrix Σ' contains $N-r$ non-zero singular values. Moreover, because the null space of ϕ^\top is spanned by $\text{span}(\psi)$, we have $V' = [\phi, \psi]$. Consequently, the above equation can be rewritten as $\begin{pmatrix} \Sigma'_{\leq N-r}^{-1} U'^\top Z \\ \mathbf{0} \end{pmatrix} = V'^\top f_N$, where $\Sigma'_{\leq N-r}$ consists of the first $N-r$ columns of Σ' , and $\Sigma'_{\leq N-r}^{-1}$ denotes its inverse. Since both V' and U' are full-rank matrices, the above equation establishes a one-to-one correspondence between Z and f_N .

Since any fixed vector can be regarded as the mean of some Gaussian distribution, we can efficiently approximate Z using a gaussian vector z . The vector z can be standard gaussian if passed through a single-layer MLP by leveraging Universal Approximation Theorem (Pinkus, 1999). Therefore, we can say that the pair $[b, z]$ uniquely determines $f = f_\Phi + f_N$. Equivalently, there exists a learnable mapping $G: \mathbb{R}^{m+N-r} \rightarrow \mathbb{R}^N$ such that $G([b, z]) = f$, which completes the proof. \square

E.7. Proof of Theorem 3.2

Proof. Suppose we take a posterior conditioned on a fixed b , i.e., $p(f | b)$, and transform it using the forward pass of our perfectly converged INN. First, if the orthogonal loss \mathcal{L}_{ort} converges to zero, we have $q(b, z) = p_B(b)p_Z(z)$, according to Definition E.5 (for KL divergence) and Lemma E.10 (for MMD). Then because $\mathcal{L}_{\text{con}} = \mathbb{E}[(\Phi f - b)^2] \rightarrow 0$ and

$\mathcal{L}_{\text{inv}} = \mathbb{E} \left[(f - G(G^{-1}(f)))^2 \right] \rightarrow 0$, we know that the INN's output distribution of b' (marginalized over z) must be $p'_B(b') = \delta(b' - b)$ where $\delta(\cdot)$ is the Dirac delta function. Also, because of the independence between z and b' in the output, the output distribution of z is still pre-defined $p_Z(z)$. So the joint distribution of outputs is $q(b', z) = \delta(b' - b)p_Z(z)$.

When we run forward the INN, and repeatedly input b while sampling $z \sim p_Z(z)$, this is the same as sampling $\pi := [b', z]$ from the joint distribution $q(b', z)$ above. Next, we show that the INN G will transform these samples back to $p(f | b)$ or $p_F(f)$ for convenience.

Note that by the change of variables theorem, we can write the backward transformation as $q(\pi) = p_F(f = G(\pi)) \left| \det \frac{dG}{d\pi} \right|$ where $\det \frac{dG}{d\pi}$ is the Jacobian determinant of the bijective function. Similarly, for the forward direction, we have $p'_F(f) = q(\pi = G^{-1}(f)) \left| \det \frac{dG^{-1}}{df} \right|$. Putting it together, we have

$$p'_F(f) = p_F(f = G(G^{-1}(f))) \left| \det \left[\frac{dG}{d\pi} \frac{dG^{-1}}{df} \right] \right| = p_F(f) |\det [\mathbf{Id}]| = p_F(f) = p(f | b),$$

which concludes our proof. \square

E.8. Proof of Theorem 3.3

Proof. Without loss of generality, we start by a rescaled version of the linear sketching problem:

$$g_j = \sum_i f_i h_{i,j}, \quad \text{s.t. } f_i \geq 0, \sum f_i = 1, g_j = \frac{b_j}{\sum_j b_j}, \text{ and } h_{i,j} = \frac{\Phi_{i,j}^\top}{\sum_i \Phi_{i,j}^\top} = \frac{\Phi_{i,j}^\top}{k_j},$$

which transforms all measures, i.e., f and b , into probability measures. Then, if the original solution is given, the solution can be transformed as follows: given the obtained solution f , the true solution is $\hat{f} = \frac{k_j}{\sum_j b_j} f$.

Our formulation can also be regarded as a statistical model. Suppose we observe N samples Y_1, \dots, Y_N , which are independently drawn from a distribution g . If the distribution $g(y)$ is given by $g(y) = \int h(x, y) f(x) dx$ where $h(x, y)$ is the corresponding kernel function of $h_{(\cdot)}$, this is equivalent to the following two-step sampling process: first draw X from $f(x)$, and then draw Y from the conditional distribution $h(x, \cdot)$ given X . In other words, the observed data Y arise from a latent variable model:

$$X \rightarrow Y, \quad \text{where } X \sim f \text{ and } Y | X = i \sim h_{i,\cdot}.$$

As a result, the joint and marginal probabilities are given by

$$P(X = i, Y = j) = f_i h_{i,j}, \quad P(Y = j) = g_j = \sum_i f_i h_{i,j}.$$

This structure constitutes a standard latent variable model, which is formally very similar to a Gaussian Mixture Model (GMM), except that in this case, the transition probabilities $h_{i,j}$ are fixed and known. If we only observe the data Y_1, \dots, Y_N , the likelihood function is given by $L_N(f) = \prod_j (\sum_i f_i h_{i,j})^{n_j}$, where n_j denotes the number of times Y takes the value j , and $\sum_j n_j = N$. Therefore, the log-likelihood is $\log L_N(f) = \sum_j n_j \log (\sum_i f_i h_{i,j})$. If we express the empirical distribution as $g_j = \frac{n_j}{N}$, then we obtain

$$\frac{1}{N} \log L_N(f) = \sum_j g_j \log \left(\sum_i f_i h_{i,j} \right) \quad (7)$$

Next, we show its connection with KL divergence. First, we can interpret the sketching problem $g_j = \sum_i f_i h_{i,j}$ as solving the following optimization problem: $\min_{f \geq 0, \sum f_i = 1} \mathcal{D}_{\text{KL}}(g \| H^\top f)$ where $H^\top f$ represents the distribution induced by f through the transition matrix H , i.e., $(H^\top f)_j = \sum_i f_i h_{i,j}$. In other words, we seek a distribution f such that the resulting mixture distribution $H^\top f$ is as close as possible to the observed empirical distribution g , measured in terms of KL divergence. By Definition E.5, this minimization problem is equivalent to: $\max_f \sum_j g_j \log (\sum_i f_i h_{i,j})$, which is precisely Eqn. (7).

Now we return to the latent variable interpretation introduced earlier. Let us clarify the assumptions and notation: ① Complete data: (X, Y) , with joint distribution $P(X = i, Y = j) = f_i h_{i,j}$; ② Observed data: only Y is observed. This

is precisely the definition of an incomplete data problem. Consequently, the log-likelihood based on the complete data is $\sum_{i,j} n_{i,j} \log(f_i h_{i,j})$ where $n_{i,j}$ is the number of times $(X = i, Y = j)$ occurs. However, in practice, we can only compute the log-likelihood based on the observed data $\sum_j n_j \log(\sum_i f_i h_{i,j})$. Therefore, this problem is well-suited for iterative solution using the EM algorithm, which alternates between estimating the missing data (Expectation step, E-step) and maximizing the likelihood (Maximization step, M-step) under the current estimate of the parameters.

Formally, in each iteration of the EM algorithm, we can proceed as follows:

- **E-step:** Based on the current estimate $f^{(n-1)}$, we compute the hidden responsibility probabilities, i.e., the posterior probability that a given observation $Y = j$ originated from latent component $X = i$. This is given by Bayes' rule:

$$P^{(n-1)}(X = i | Y = j) = \frac{f_i^{(n-1)} h_{i,j}}{\sum_k f_k^{(n-1)} h_{k,j}} \quad (8)$$

- **M-step:** We update the parameter f_i by maximizing the expected complete-data log-likelihood with respect to f . The updated estimate is obtained as

$$f_i^{(n)} = \sum_j g_j P^{(n-1)}(X = i | Y = j) \quad (9)$$

Substituting the expression for the conditional probability, i.e., Eqn. (8), into the update rule, i.e., Eqn. (9), we have

$$f_i^{(n)} = f_i^{(n-1)} \sum_j \left(\frac{h_{i,j}}{\sum_k f_k^{(n-1)} h_{k,j}} \right) g_j \iff \hat{f}_i^{(n)} = \hat{f}_i^{(n-1)} \sum_j \frac{\Phi_{i,j}^\top}{(\Phi \hat{f}^{(n-1)})_j} b_j.$$

This recurrence relation provides an iterative scheme for updating the distribution f , and it corresponds exactly to the formula presented in Theorem 3.3, which concludes the proof. \square

Algorithm 4 (Pytorch) EM iterative refinement pseudocode for FLORE

```
# f: Count-Min solution (batch-wise); b: sketch observations; Phi: sketching matrix; T: number of EM steps

minloss = L1Loss(Phi @ f, b) # initialize flag
for t in range(T):
    # E-step: compute normalization factors
    C1 = Phi / (Phi @ f) # measurement-wise normalization
    C2 = f / Sum(Phi, axis=0) # prior normalization

    # M-step: multiplicative update
    ft = C2 * WeightedSum(b, C1)

    # accept update if reconstruction error is reduced
    if L1Loss(Phi @ ft, b) < minloss:
        f = ft; minloss = L1Loss(Phi @ ft, b)

return f
```

Remark E.11. From an interpretative perspective, we can view this EM algorithm as “denoising” the Count-Min solutions using global information, i.e., the linear system $b = \Phi f$. To realize the iterative update, we have the following formula:

$$f_i \leftarrow \frac{f_i}{\sum_{j=1}^m \Phi_{i,j}^\top} \sum_{j=1}^m \frac{\Phi_{i,j}^\top \times b_j}{\sum_{k=1}^N \Phi_{i,k} \times f_k} \quad (10)$$

While the EM algorithm is defined on a single-key basis, it admits more efficient GPU parallelization. Algorithm 4 illustrates the procedure in a PyTorch-like pseudocode, in which all batch-wise operations are implemented via matrix and tensor primitives. At the end of each iteration, the solution is updated only if the reconstruction error improves, guaranteeing that the refined result does not degrade and otherwise stays unchanged.

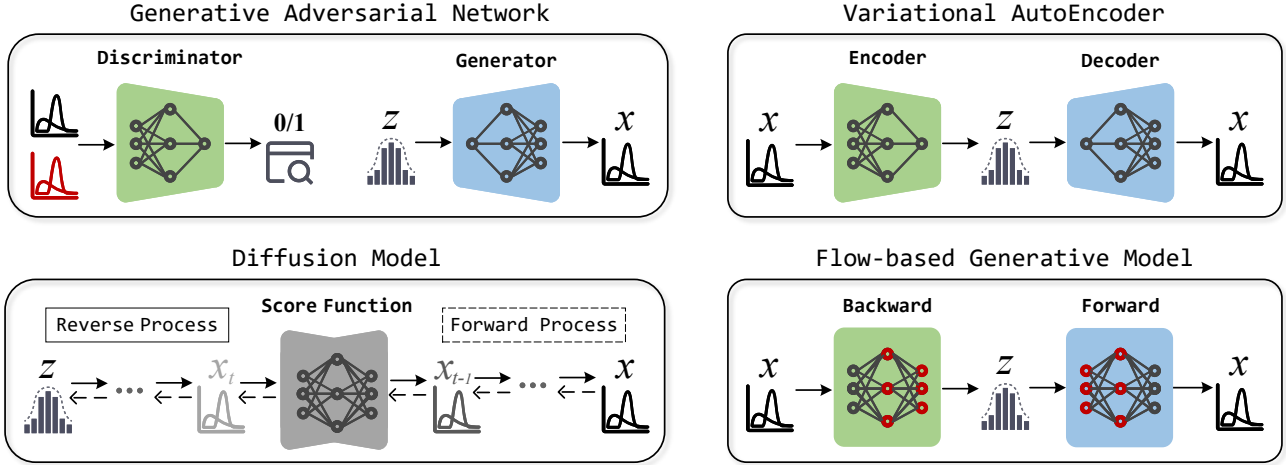


Figure 16. Overview of different types of deep generative models considered in this work.

F. On the Choice of GMs for Data Stream

In this section, we aim to analyze deep GM families to select a base model for our generative sketching paradigm. As mentioned in §3.1, here we restrict our analysis to four representative classes of deep generative models—① Variational Autoencoders (VAEs): it learns a probabilistic latent representation by optimizing a variational lower bound. ② Generative Adversarial Networks (GANs): it generates data through an adversarial game between a generator and a discriminator. ③ Diffusion Models (DMs): it synthesizes data by iteratively reversing a noise-injection process. ④ Flow-based Generative Models (FGMs): it constructs an exact and invertible mapping between data and latent variables, allowing tractable likelihood computation and efficient sampling under architectural constraints. The high-level overview of these four GMs is illustrated in Figure 16. Further, to support real-world streaming applications, our model selection is guided by three key principles: (i) The selected GM should support **easy adaptation**, because after prolonged usage, the model inevitably encounters generalization issues, and any subsequent fine-tuning must minimize disruption as much as possible; (ii) The selected GM should support **fast inference**, because sketch recovery and downstream analytics are often performed under limited latency constraints in high-speed data stream processing; and (iii) The selected GM should support **high accuracy & realness**, because faithful reconstruction of the underlying data distribution is essential for reliable estimation and decision-making in measurement-based applications.

F.1. Unconditional Distribution Modeling Capability

We start with evaluating the GM’s ability to fit the data stream distribution, as this ability forms the foundation of any downstream generative task. To this end, we construct synthetic data streams drawn from two different distributions. Specifically, *Gaussian* streams are used to assess the models’ generalization ability under smooth and light-tailed distributions, while *Zipfian* streams are adopted to emulate natural data stream characteristics with strong skewness and heavy tails. For both distributions, we vary the streaming data dimensionality, i.e., the number of distinct keys, from 1K to 100K, thereby systematically examining the robustness and scalability of each model across a wide range of stream sizes. Then, we train unconditional GMs on these synthetic streams using standard training protocols. All models adopt lightweight architectures composed of simple linear layers. VAEs, GANs, and FGMs are implemented with conventional adversarial or log-likelihood objectives, while the Wasserstein distance regularization is additionally included to improve adversarial training stability (WGAN, Arjovsky et al., 2017). For DMs, we directly train the underlying network to predict the clean signal from noisy inputs (Yuan & Qiao, 2024; Li & He, 2025), in which 1,000 diffusion and sampling steps is used.

Figure 17 compares the sampling results of these five methods on the two datasets, in which the closer the curve is to the GT curve, the better the distribution fitting capability. The figure shows that all GMs perform very well under the 1K and 10K settings. Among them, FGM and DM exhibit the most accurate fits, whereas VAE and GAN perform slightly worse. Compared to GAN, WGAN yields more confident generations, with its curve consistently exhibiting a sharper peak around the GT mode. However, as the dimensionality of the data stream increases to 50K and 100K, the performance landscape changes markedly. VAE fails to approach the target distribution, and GAN-based methods suffer from severe instability (see 1st row), from which even WGAN cannot escape this “fate”. In contrast, FGM and DM remain robust under

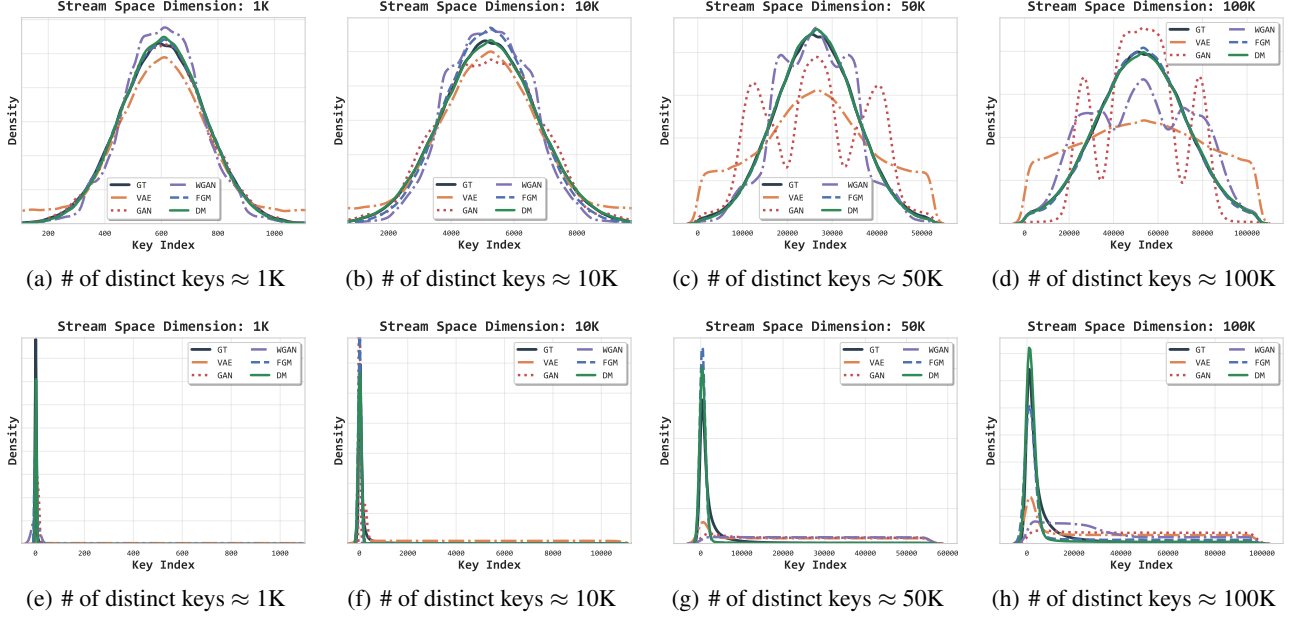


Figure 17. Visualization of Streaming data distribution fitting. The first row shows results on Gaussian distributions, while the second row shows results on Zipfian distributions. From left to right, the scale of the data stream gradually increases.

high-dimensional settings. Even worse, in heavy-tailed distributions (see 2nd row), the aforementioned methods cannot even capture the overall “shape”. Notably, DM demonstrates superior capability in accurately shaping the underlying distribution. Hence, from the perspective of unconditional distribution learning, FGM and DM emerge as the most suitable candidates.

F.2. Conditional Generation for Stream Recovery

Next, we evaluate the transferability of the (unconditional) generative capabilities of different models to downstream data stream (conditional) recovery. To elicit the GM’s intrinsic distribution-shaping capability and minimize the influence of the underlying architecture, we directly extend the unconditional GM to a conditional version. Our approach is based on gradient-based search in the latent space of the GM for a “good” latent variable z that produces content consistent with the observed data. By following prior works (Bora et al., 2017; Yuan et al., 2023), for all GMs except DMs, we first identify a “starting point,” and then perform backward updates on it using the gradient of $\|b - \Phi f_G(z)\|_2^2 + \|z\|_1$ with regard to z , where the former term enforces consistency with the observations, while the latter term promotes plausibility (or likelihood). Regarding DMs, we directly integrate this gradient adjustment into the reverse sampling process, as applying the aforementioned iterative refinement to them would be too time-consuming. See DPS (Chung et al., 2023) for more details. Algorithm 5 and Algorithm 6 present our two implementation strategies, respectively.

Algorithm 5 Estimation Algorithm for Unconditional GMs

Ensure: Volume estimation using an unconditional GM
Require: GM f_G , strength ζ , matrix Φ , # of loops K
 $\{z_0, \dots, z_i, \dots\} \leftarrow$ sample a set of priors from $\mathcal{N}(0, I)$
 Select a good z such that $\arg \min_{z_i} \|b - \Phi f_G(z_i)\|_2^2$
 $b \leftarrow$ sample counters by linear sketching
for $j = K$ to 0 **do**
 $z \leftarrow z - \zeta \nabla_z (\|b - \Phi f_G(z)\|_2^2 + \|z\|_1)$
end for
 $x \leftarrow f_G(z)$
 return x

Algorithm 6 Estimation Algorithm for Unconditional DMs

Ensure: Volume estimation using an unconditional DM
Require: DM f_G , strength ζ , matrix Φ , # of steps T
 $x_T \leftarrow$ sample prior from $\mathcal{N}(0, I)$
 $b \leftarrow$ sample counters by linear sketching
for $t = T$ to 0 **do**
 $x'_{t-1} \leftarrow \text{REVERSESAMPLEONESTEP}(x_t, t, f_G)$
 $\hat{x}_0 \leftarrow \text{PREDICTX0WITHXT}(x'_{t-1}, t)$
 $x_{t-1} \leftarrow x'_{t-1} - \zeta \nabla_{x_t} \|b - \Phi \hat{x}_0\|_2^2$
end for
 return x_0

We still experiment on the two synthetic datasets described above, employ Count-Min as the underlying sketch, insert the

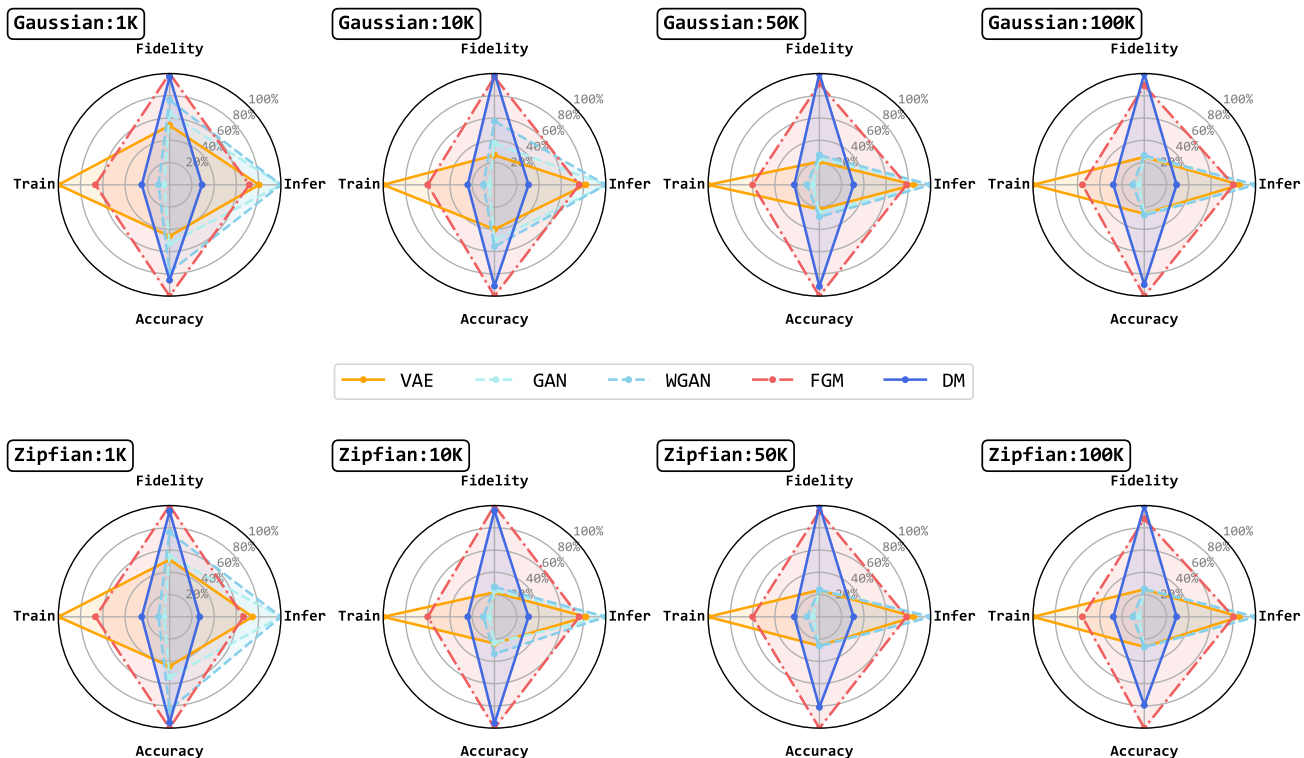


Figure 18. Performance comparison of different generative models under Gaussian and Zipfian distributions. For better visualization, metrics across different dimensions are normalized by the best result, where higher values indicate better performance.

GT vector into the sketch, construct the projection matrix Φ , and force the trained GM to recover the GT vector from the sketch counters b . As Figure 18 shows, we test their sketching performance along four dimensions to embrace our principles: *fidelity* measured by WMRE, *accuracy* measured by ARE, *inference* time measured by the logarithmic time (ms) taken for a single generation pass, and *training* time (s) measured by the time taken for training the GM. On one hand, consistent with their unconditional generation results, VAEs and GANs perform adequately on small-scale data streams, but their accuracy and fidelity drop sharply as data dimensionality increases, especially under Zipfian distributions, whereas FGM and DM remain robust. On the other hand, what is not evident from unconditional generation results is that: First, despite DM consistently achieving the highest fidelity, its accuracy does not follow suit. For instance, under the Zipfian distribution, DM’s accuracy gradually falls behind that of FGM. Second, GANs suffer from extremely long training times, roughly 5 ~ 10 times longer than other methods, due to their notoriously unstable adversarial training; as dimensionality increases, convergence to an optimal generator requires painstaking and delicate parameter tuning. Meanwhile, DM also faces severe inference inefficiency, as it requires lengthy iterative sampling along a Markov chain. Concretely, generating a single sample (or batch) of 100K-dimensional vectors with 1,000 diffusion steps consumes over 10 GB of GPU memory and takes tens of seconds, making it roughly $10^3 \times$ slower than alternative approaches. Given these two critical limitations, we exclude both GANs and DM from further consideration. Finally, due to the limited expressive power of VAEs, we select FGMs, which offer a more favorable balance, as the backbone model for our generative sketching paradigm.

G. Supplementary Experimental Results

In this section, we report additional experiments that could not be accommodated in the main text. Below, we sequentially present: comparisons on synthetic data streams (G.1), distributional visualization (G.2), ablation studies (G.3), and robustness evaluation under changing conditions (G.4).

G.1. Additional Results on Synthetic Data Stream

To evaluate the adaptability of our method to data streams with different distributions, Figure 19 details its performance across five heavy-tailed distributions, including Zipf, Pareto, Exponential, and Log-Normal. The overall trend closely

mirrors that observed on real-world datasets in the main text (with FLORE consistently achieving optimal or near-optimal results), yet the degree of distribution skew impacts performance.

First, regarding per-element accuracy (columns 1~2): Under tight memory budgets, all non-CS-based approaches perform poorly. For instance, CM and CS typically incur errors on the order of 10^3 (both relative and absolute) at 16KB. Learning-augmented sketches fare even worse, as they require extra space to store a small subset of hot items and their classifiers. Interestingly, LS performs well under certain skew levels by directly truncating counters (e.g., highly skewed CAIDA, and moderately skewed Exponential and Log-Normal here), though this advantage quickly diminishes as memory increases. Among CS-based schemes, PR exhibits severe estimation instability, only converging to reasonable error levels when ample memory is available (as the system becomes determined and admits a unique solution). NZE steadily improves accuracy with more memory, making it the most accurate sketch algorithm (trading computational complexity for performance), but it is still outperformed by FLORE. Specifically, FLORE reduces error by up to $700\times$ compared to other methods and achieves near-zero error at memory sizes of 256KB and above.

Second, regarding heavy-hitter accuracy (column 3): The behavior under the Zipf distributions closely mirrors that of the real-world distributions presented in the main text, where FLORE always achieves near 100% accuracy, requiring only 16KB. However, “surprises” emerge under the Exponential and Log-Normal distributions. Almost all methods fail to detect heavy hitters effectively under a low skewness, as the keys become less distinguishable. Notably, CM performs worse than usual, even falling behind PR (which typically ranks last), with its peak F1 score barely reaching around 80%. Other approaches, including CS, optimizations, and learning-augmented sketches, suffer similarly. LS is particularly noteworthy: its counter-truncation strategy yields unusually low accuracy on these latter two distributions. In contrast, FLORE not only consistently sits at the top of the curves but also demonstrates remarkable recovery: although its performance at 16KB is subpar, it rebounds almost linearly thereafter, pulling ahead of all competitors by a wide margin. Specifically, FLORE achieves roughly $2\times$ to $4\times$ higher F1 scores.

Third, regarding distribution alignment (column 4~5): Thanks to its generative nature, though it is fully GT-free, FLORE continues to dominate decisively on these metrics. Specifically, FLORE’s WMRE rarely exceeds 0.5, while most baseline methods require as much as 512KB of memory to achieve comparable accuracy. Even more strikingly, under tight memory budgets, FLORE’s error is less than 1/3 that of baselines. Moreover, even high-accuracy CS-based methods like PR and NZE suffer from inherent limitations in distribution modeling. Notably, NZE’s enforced sparsity during reconstruction inevitably compromises fidelity to the true underlying distribution. Regarding entropy estimation, although low-skew distributions narrow the performance gap between FLORE and other methods, FLORE still significantly outperforms all non-CS-based approaches. For example, on the Zipf dataset, FLORE’s absolute entropy estimation error is, on average, $105.14\times$ and $712.98\times$ smaller than that of CM and CS, respectively. Another observation is that PR’s performance improves noticeably in the bottom two rows, sometimes even surpassing FLORE, but its gains remain very limited when ample memory is available. We attribute this stagnation to the solver’s inability to find a sparser solution, causing it to plateau.

G.2. Additional Results on Visualizations

To gain insights into the behaviors of sketches, we next visualize and compare the recovery results from each sketch viewpoint (i.e., FLORE, CM, CS, NZE, LCM, and LCS), which can also be regarded as a reflection of how well the distribution is perceived by them. The resulting visualizations under different distributions and space budgets are shown from Figure 20 to Figure 22, where key-wise frequencies are aggregated by their nearest 100 elements. Similar to the visualizations in the previous section, here the more the shaded areas overlap and the smaller the area, the better the results. First of all, the output of all sketches becomes more realistic as the memory budget increases. We also observe that all non-CS methods significantly overestimate the true frequencies of most elements because they lack a global perspective. Meanwhile, due to the need to satisfy both consistency and sparsity constraints, the total area of NZE using compressive sensing is close to that of the true distribution; however, it often compensates for high-frequency items by underestimating the majority of values or otherwise. In comparison, FLORE consistently achieves the highest fidelity in both curve shape and overall pattern under identical settings. Although FLORE partially overestimates the true values of some elements at 32KB under the guidance of the CM enhanced by EM refinements, it requires only 128KB to become nearly indistinguishable from the ground-truth pattern, achieving an almost perfect fit. This aligns with our quantitative distribution estimation results (WMRE) and can be attributed to the powerful distribution approximation capability of the generative modeling paradigm.

On the (Generative) Linear Sketching Problem

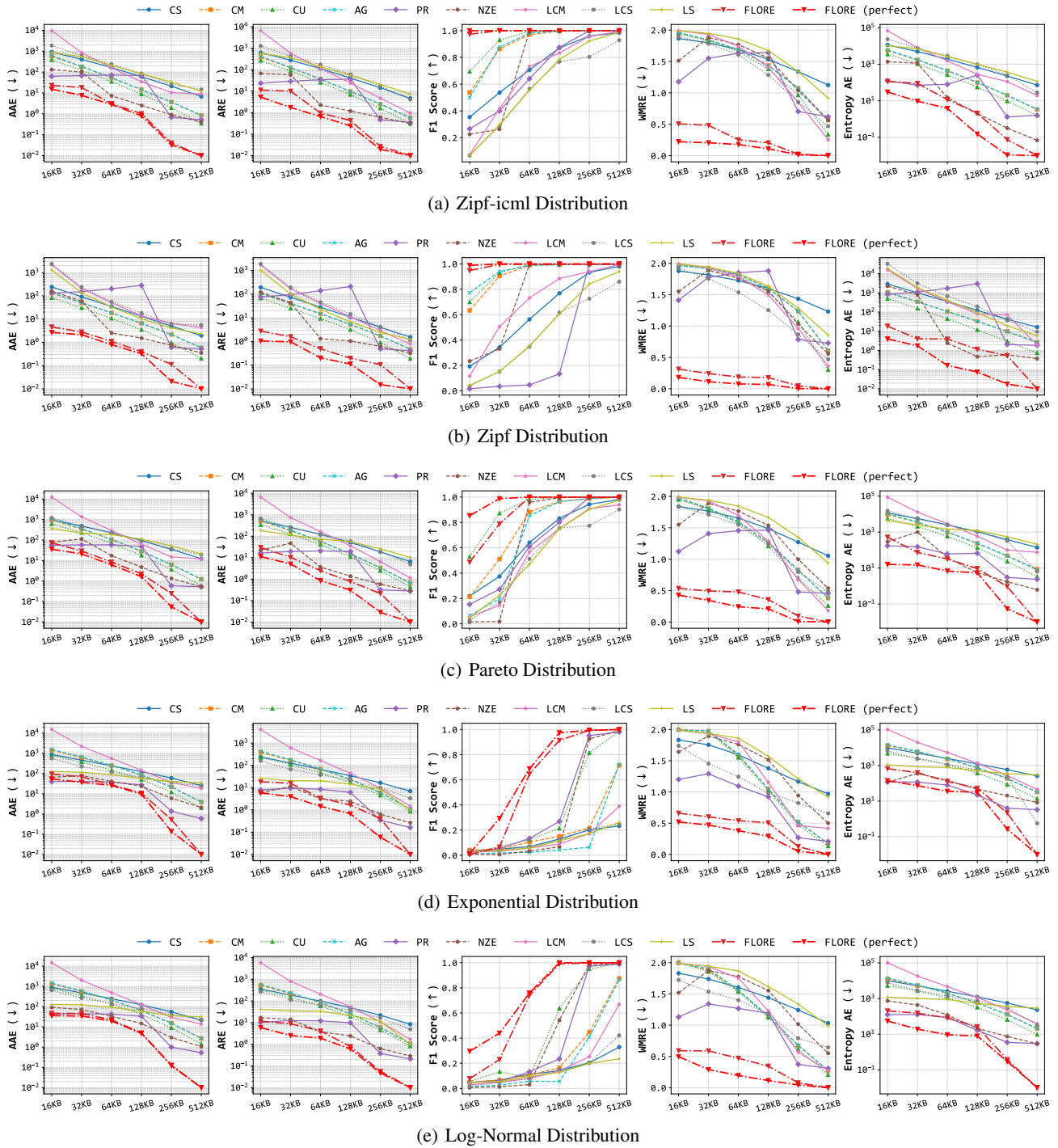


Figure 19. Sketching performance comparison with different synthetic streaming data distributions. The length of all synthesized streams is fixed at 1 million items. While the number of distinct keys varies across different heavy-tailed distributions, it stays at approximately 30k across all cases. FLORE exhibits substantially stronger robustness to distributional variation compared to the alternatives.

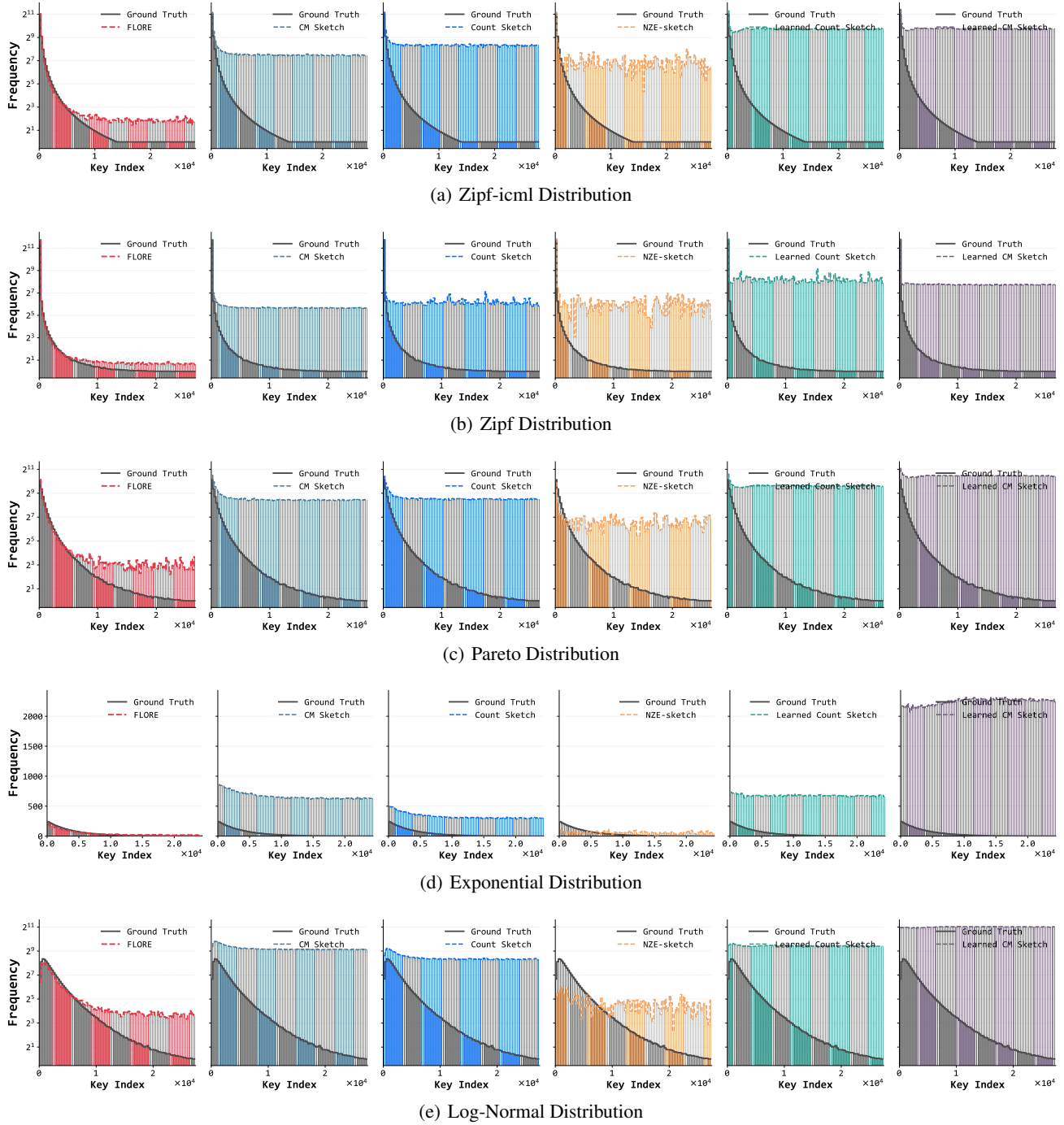


Figure 20. Visualizations of sketch recovery under a fixed 32KB memory budget. From left to right, we present the recovery results of FLORE, CM, CS, NZE, LCM, and LCS, compared against the ground-truth sample distribution. To enhance readability, every 100 consecutive keys are aggregated in the x-axis.

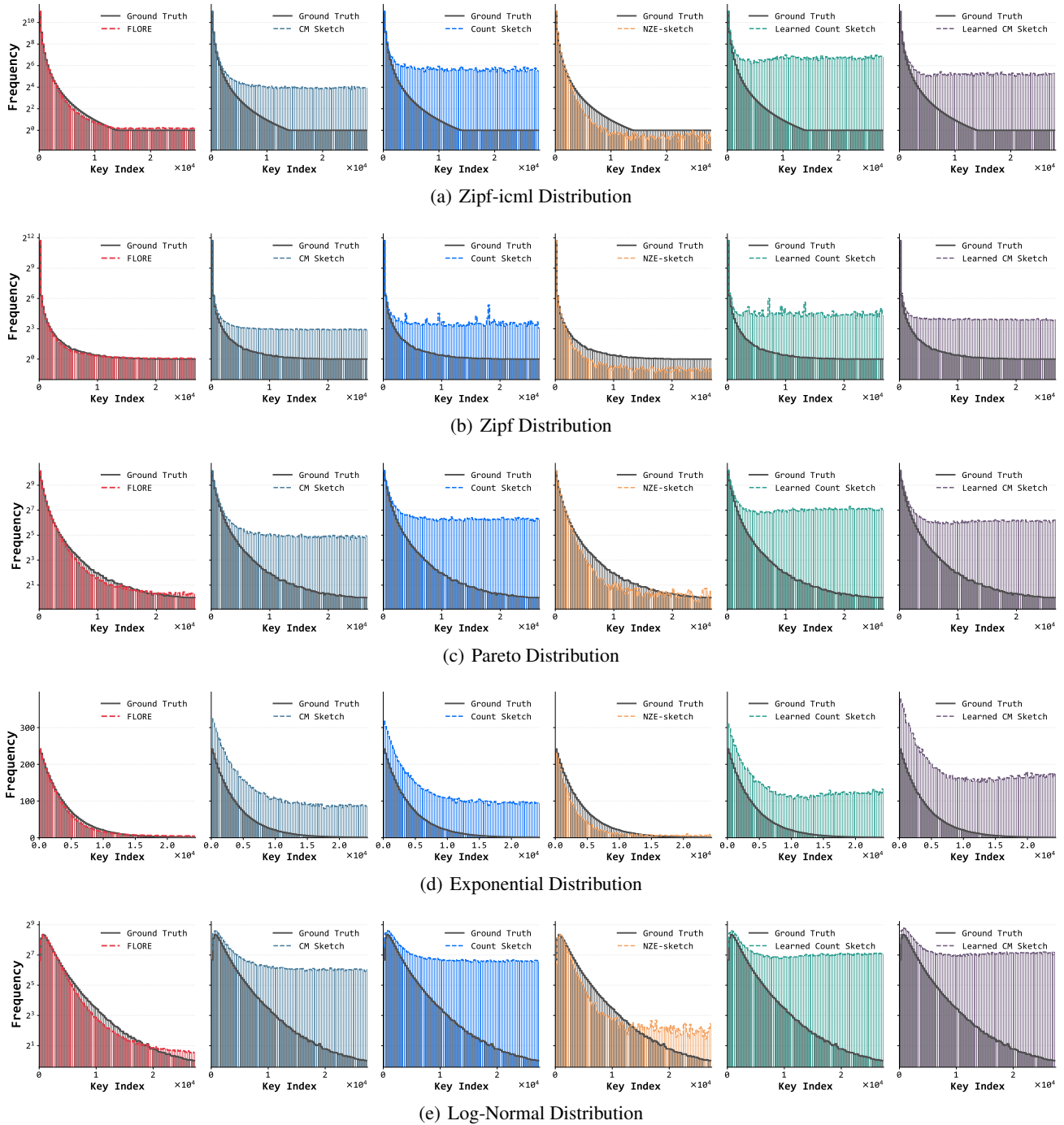
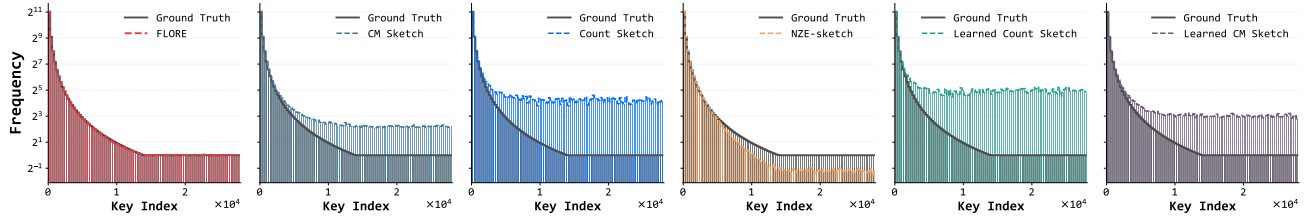
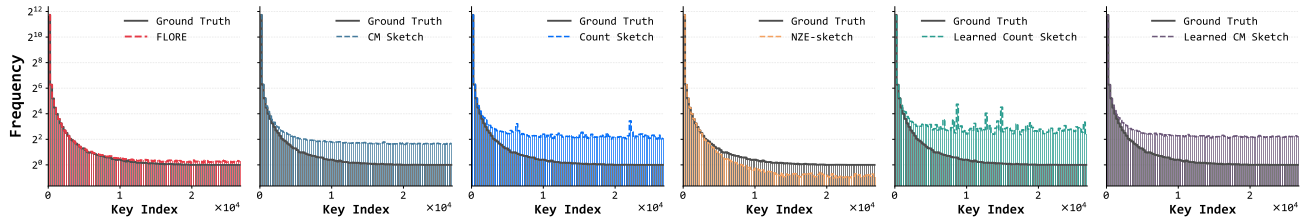


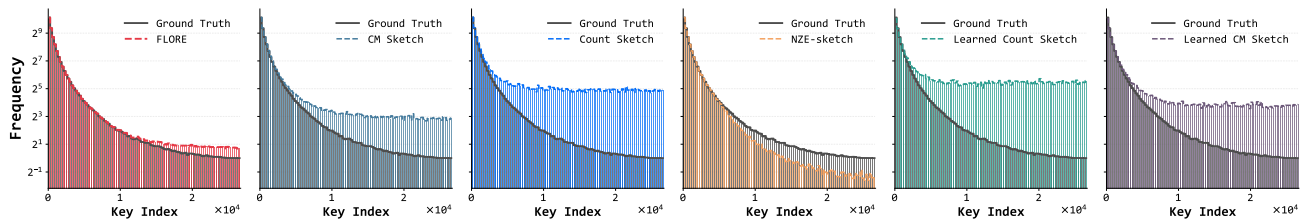
Figure 21. Visualizations of sketch recovery under a fixed 128KB memory budget. From left to right, we present the recovery results of FLORE, CM, CS, NZE, LCM, and LCS, compared against the ground-truth sample distribution. To enhance readability, every 100 consecutive keys are aggregated in the x-axis.



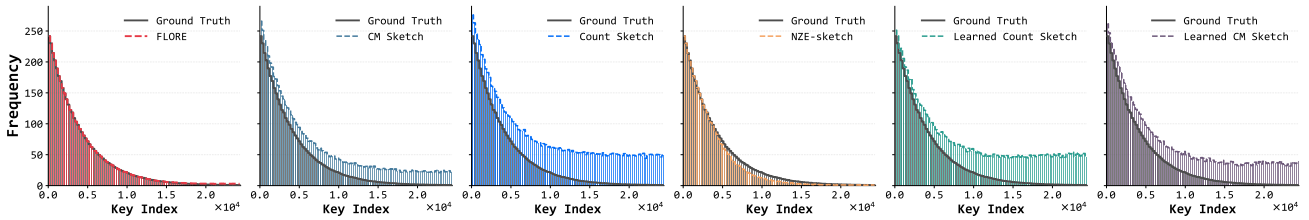
(a) Zipf-icml Distribution



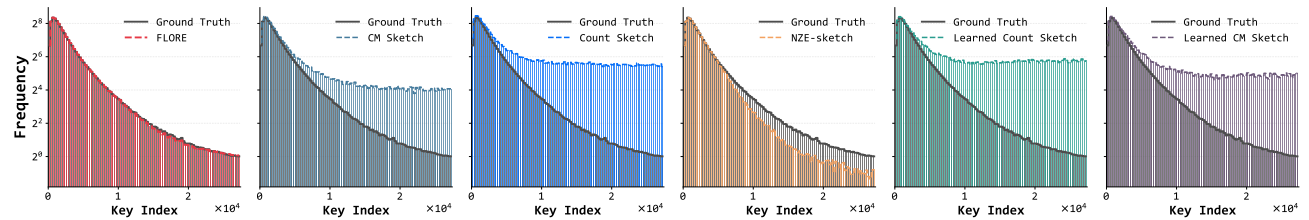
(b) Zipf Distribution



(c) Pareto Distribution



(d) Exponential Distribution



(e) Log-Normal Distribution

Figure 22. Visualizations of sketch recovery under a fixed 256KB memory budget. From left to right, we present the recovery results of FLORE, CM, CS, NZE, LCM, and LCS, compared against the ground-truth sample distribution. To enhance readability, every 100 consecutive keys are aggregated in the x-axis.

On the (Generative) Linear Sketching Problem

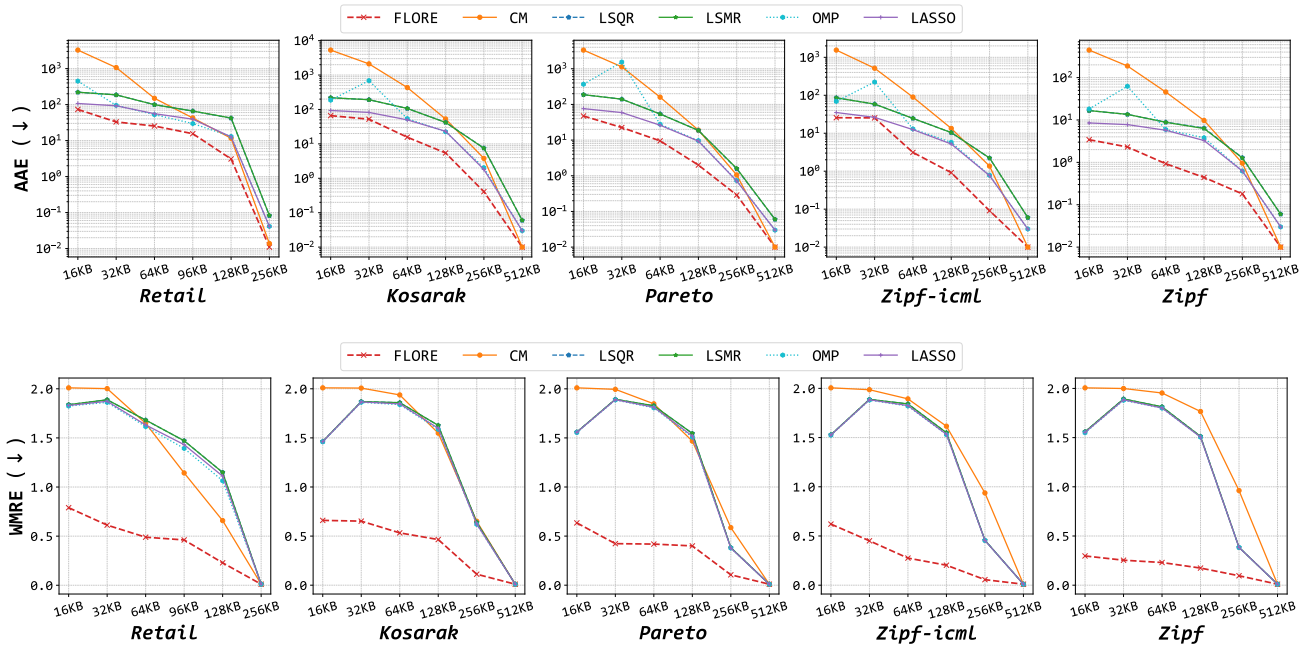


Figure 23. Comparing FLORE with the Count-Min and SOTA compressive sensing algorithms by replacing the generative model.

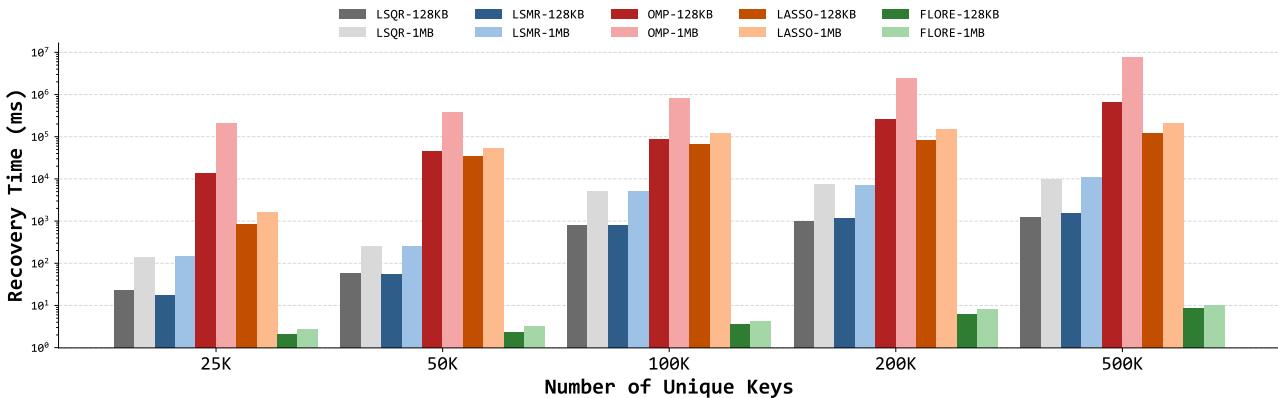


Figure 24. Comparison of computation times for recovery procedure.

G.3. Ablation Studies

Next, we perform several ablation studies to assess the impact of FLORE’s key features on its overall performance.

G.3.1. EFFECT OF GENERATIVE MODEL

To further validate our generative method, we replaced the INN-based generator with four SOTA CS algorithms: LSQR (Paige & Saunders, 1982), OMP (Pati et al., 1993), LASSO (Tibshirani, 1996), and LSMR (Fong & Saunders, 2011). Since FLORE is built on top of Count-Min Sketch, a Count-Min query algorithm (i.e., CM) is included here as a traditional benchmark. The main results are shown in Figure 23. We conduct experiments on five relatively small datasets, since these CS algorithms are often very resource-consuming (see results discussed later). Overall, our method consistently outperforms the CS baselines in terms of accuracy. More notably, the improvement in distribution fidelity is substantially larger, achieving on average approximately a 65% gain over the best baseline.

Also, we compare the computation time for FLORE with other LP-based CS algorithms in Figure 24. As the stream size increases, we observe that FLORE demonstrates scalable performance precisely as intended, requiring less than 15 ms of

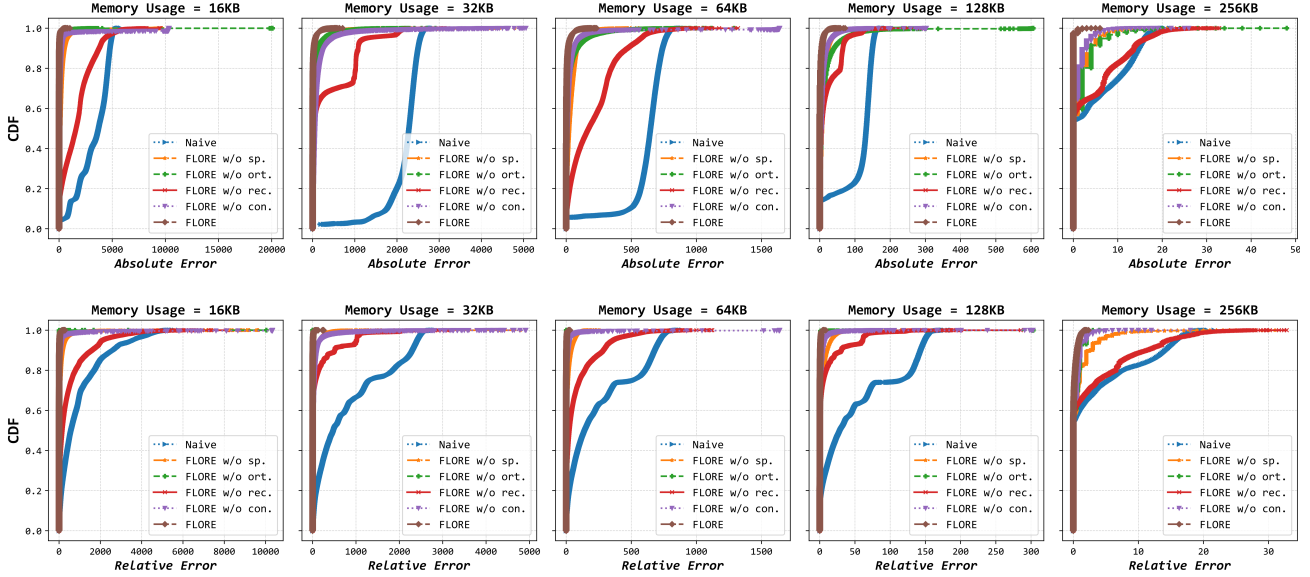


Figure 25. CDFs for the AAE and ARE of FLORE and its variants on the real-world Kosarak dataset.

computation time while achieving better recovery. When the number of unique keys is 500K, for instance, FLORE achieves $10^2 \sim 10^6 \times$ speedups relative to the baselines, accentuating the importance of employing an FGM in the control plane.

G.3.2. EFFECT OF TRAINING OBJECTIVE

We next evaluate the impact of training losses used by **FLORE**. In accordance with our design choices, we consider the following five FLORE variants for comparison. (i) **Naive**: This variant removes all generative losses (i.e., \mathcal{L}_{inv} , \mathcal{L}_{ort} , and \mathcal{L}_{rec}) in the FGM and degenerates into a simple one-way mapping function. (ii) **FLORE w/o sp.**: This variant removes the sparsity constraint (i.e., \mathcal{L}_{sp}) introduced by compressed sensing theory. (iii) **FLORE w/o ort.**: This variant eliminates the orthogonality constraint (i.e., \mathcal{L}_{ort}) between z and b . (iv) **FLORE w/o rec.**: This variant discards the reconstruction guidance (i.e., \mathcal{L}_{rec}) provided by CM + EM and relies solely on counter-based learning. (v) **FLORE w/o con.**: This variant removes the explicit linear equation constraints (i.e., \mathcal{L}_{con}), leaving the model to learn without structural supervision. As shown in Figure 25 and Figure 26, we plot the cumulative distribution function (CDF) that shows absolute/relative errors achieved by FLORE and its variants on Kosarak and Zipf, respectively.

The simple mapping function **Naive** exhibits the most severe performance degradation, underscoring the critical role of the generative paradigm in recovery. The variant **FLORE w/o rec.** performs better than **Naive** but still suffers from a substantial loss in accuracy. This behavior arises because a generative model requires an effective “information channel” to anchor its learning to the underlying GT vector, a role that is fulfilled by our EM algorithm. While not as critically important as the two aforementioned loss terms, the other three variants demonstrate their impact through fine-grained adjustments. In particular, these variants tend to produce a small number of outliers with exceptionally large errors. For example, on the Kosarak dataset with a 16KB budget, **FLORE w/o ort.**, **FLORE w/o con.**, and **FLORE w/o sp.** each exhibit data points with absolute errors of 20,000, 10,000, and 8,000, respectively. Interestingly, although the consistency enforced by the linear equations is intuitively expected to play a central role, directly removing it does not cause the sketch measurement system to collapse. This is because the solution obtained by our EM algorithm already approximately satisfies this constraint, thereby implicitly guiding the model to learn the desired relationship. In contrast, FLORE exhibits consistently stable performance across all scenarios: more than 90% of its restoration errors lie within the lowest 10% of error magnitudes, and such extreme outliers are almost entirely eliminated. These observations corroborate the effectiveness of each training loss component in FLORE.

G.3.3. EFFECT OF STREAM FILTERING

Because the key-value pairs stored in the augmented filter are guaranteed to be accurate, we further conduct an analysis on the processing speed improvement brought by FLORE’s stream filtering mechanism, as indicated by “FLORE w/o Stream Filtering”. To enable a finer-grained dissection of effective components, we also introduce two additional baselines:

On the (Generative) Linear Sketching Problem

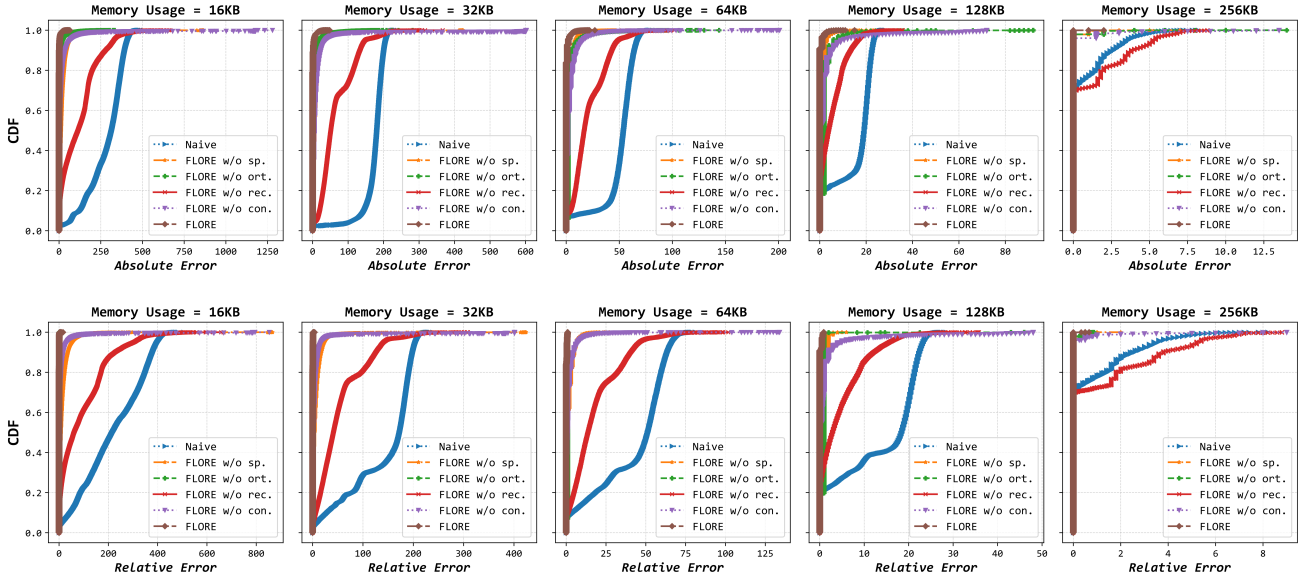


Figure 26. CDFs for the AAE and ARE of FLORE and its variants on the synthetic Zipf dataset.

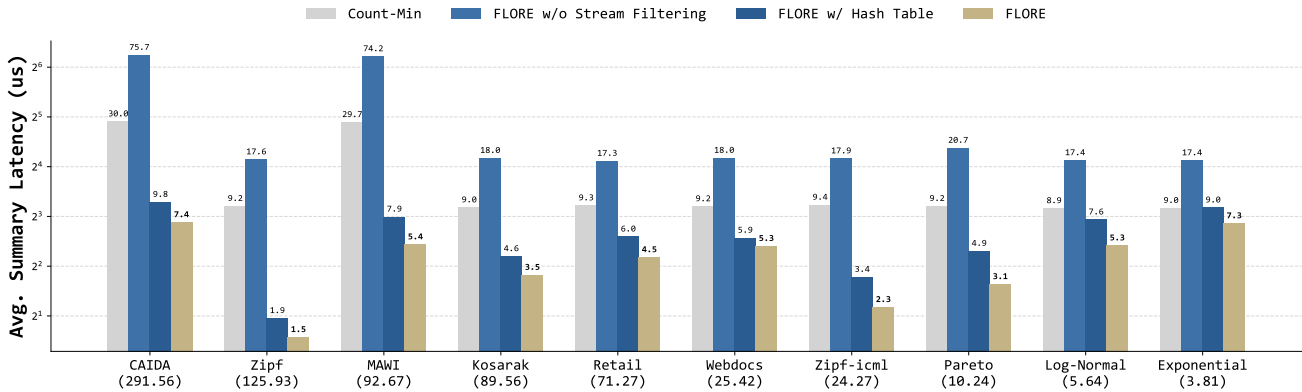


Figure 27. Ablation comparing FLORE and FLORE without the stream filtering mechanism or separation design, where (x) at the bottom indicates that the data stream has skewness x .

Count-Min and FLORE w/ Hash Table. The former is a standard Count-Min sketch that completely removes the idea of separation, representing a naive data stream summarization approach without key tracking mechanism. The latter replaces FLORE’s Ostracism-based filtering algorithm with a simpler hash-table strategy (following the design of NZE-sketch) to investigate the impact of the proposed algorithmic design. We report the average time (or latency) required to summarize a single data item across all ten datasets in Figure 27. From the figure, we have three important findings. First, FLORE w/o Stream Filtering is even slower than Count-Min because it requires additional time to consult the Bloom Filter to determine whether a key belongs to the existing set. Second, even simply adding a hash table (i.e., FLORE w/ Hash Table) dramatically reduces processing latency, by more than 5x on average, and the performance gain becomes even greater as the skewness of the data stream increases. Third, our Ostracism-based mechanism further accelerates processing speed. Although FLORE involves a lookup operation, this operation runs in constant time and yields an additional 15% improvement over the hash-table baseline.

G.3.4. EFFECT OF EM REFINEMENT

Figure 28 compares the simple CM and CM equipped with 10-step EM refinement (as indicated by “CM + EM”) when testing in the CAIDA dataset (1st row) and MAWI dataset (2nd row). It can be seen that the enhancement brought by EM is truly impressive. To be more specific, on the CAIDA dataset, it reduces CM’s AAE by approximately 76% and ARE by about 86%. Similarly, on the MAWI dataset, it lowers CM’s AAE by roughly 80% and ARE by around 84%. The

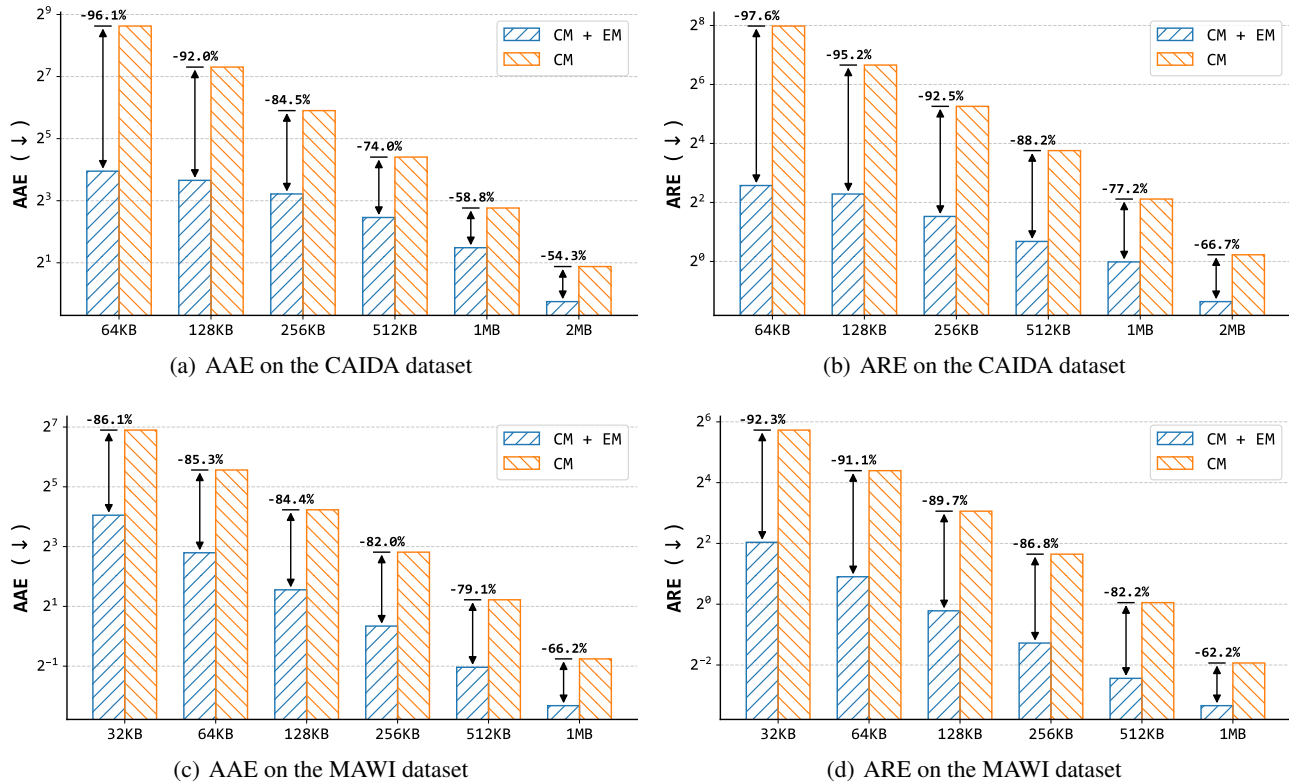


Figure 28. Ablation comparing Count-Min Sketch and Count-Min Sketch + EM refinement (with ten steps).

result is consistent with our theoretical analysis (see Theorem 3.3). However, as noted in §3.2, this comes at the cost of expensive iterative search, especially when the dimensionality of Φ reaches into the tens of thousands. In fact, for large-scale data streams like CAIDA, which involve over 150K dimensions, the CPU often requires minutes of EM refinement time. Although we can accelerate this process using GPU parallelization, it may still incur tens of GB of GPU memory overhead, but fortunately, this computation is needed only once during training.

G.4. Additional Results on Changing Condition

Finally, we evaluate the robustness of FLORE under temporal, natural, and spatial variations in data streams. In these experiments, we randomly sample 10% to 20% of the key set to simulate changes in stream behavior in each sampling epoch, following the prior work (Yuan et al., 2026). All experiments are conducted on the CAIDA dataset.

| Memory | | Fluctuation Factor | | | |
|--------|-----------|--------------------|-------|-------|-------|
| | | 0.2 | 0.5 | 1.0 | 2.0 |
| 128KB | average | 0.0% | -1.0% | -1.8% | 2.7% |
| | 90th Pct. | 0.4% | -0.2% | -2.1% | 5.9% |
| 256KB | average | -0.0% | -1.1% | -1.8% | 1.9% |
| | 90th Pct. | 0.2% | -0.3% | -1.4% | 2.8% |
| 512KB | average | 0.2% | 0.0% | -1.0% | 1.0% |
| | 90th Pct. | 0.3% | -0.0% | 1.1% | 1.3% |
| 1MB | average | 0.0% | -1.9% | 0.2% | -0.3% |
| | 90th Pct. | 1.1% | -0.8% | 0.2% | -0.5% |

Table 3. ARE Performance decline with increased CAIDA network traffic fluctuation. Negative values indicate no degradation.

| Memory | | Training stream time windows | | |
|--------|-----------|------------------------------|---------|---------|
| | | 0%-25% | 25%-50% | 50%-75% |
| 128KB | average | 5.4% | 3.6% | 4.4% |
| | 90th Pct. | 9.6% | 7.8% | 8.7% |
| 256KB | average | 2.6% | 3.2% | 2.1% |
| | 90th Pct. | 4.0% | 5.7% | 4.6% |
| 512KB | average | 0.2% | 1.8% | 0.5% |
| | 90th Pct. | 0.9% | 0.2% | 1.0% |
| 1MB | average | 0.5% | 1.6% | -1.5% |
| | 90th Pct. | 0.0% | 1.0% | 1.6% |

Table 4. ARE Performance decline with natural drift in CAIDA network traffic. Negative values indicate no degradation.

| Memory | | Proportion Factor | | | |
|--------|-----------|-------------------|-------|-------|-------|
| | | 0.9 | 0.5 | 0.25 | 0.1 |
| 128KB | average | 0.3% | 0.7% | 1.8% | 2.3% |
| | 90th Pct. | 1.7% | 1.0% | 3.1% | 6.5% |
| 256KB | average | 0.2% | 0.6% | 1.5% | 2.6% |
| | 90th Pct. | 0.4% | 0.7% | -0.4% | 2.4% |
| 512KB | average | 0.0% | -0.6% | 1.7% | 1.3% |
| | 90th Pct. | 0.2% | 0.4% | 1.4% | 0.6% |
| 1MB | average | 0.5% | 0.7% | -1.0% | -1.6% |
| | 90th Pct. | 0.0% | -0.6% | -0.4% | 1.4% |

Table 5. ARE Performance decline with spatial shift in CAIDA network traffic. Negative values indicate no degradation.

Temporal changes. To increase temporal variability, we proceed as follows. For each selected key, we generate a temporal change in one epoch by sampling from a Gaussian distribution $\mathcal{N}(\mu, \sigma^2)$ and scaling it by a factor, where $\mu = 0$ and σ is the standard deviation across different sampling epochs of the key. The scaling factor $\in \{0.2, 0.5, 1.0, 2.0\}$ controls the

amplitude of the fluctuation. We evaluate the impact of sudden changes by measuring the ARE degradation of FLORE relative to its performance under stable conditions. The results are summarized in Table 3. When the scaling factor is relatively small, FLORE exhibits no noticeable performance degradation. Even when the scaling factor = 2, the performance degradation is still within 10%.

Natural changes. To test the impact of natural shifts, we conduct training separately with 0%-25%, 25%-50%, and 50%-75% of the sampled counters, followed by testing on the last 25%. Note that evaluation is performed only on the selected keys that appear in all four parts. This protocol enables us to quantify performance degradation relative to the setting in which 75% of the data is used for training. The results w.r.t. ARE are summarized in Table 4. We observe that FLORE maintains stable performance on the selected keys even long after the completion of training (exceeding two times the total duration of the training data).

Spatial changes. To simulate changes in the spatial distribution of frequencies, we redistribute frequencies across different keys in one epoch. Specifically, we reassign the top 10% of hot keys to the selected keys such that they account for 90%, 50%, 25%, and 10% of their original total volume. We refer to the resulting scaling parameter as the proportion factor $\in \{0.9, 0.5, 0.25, 0.1\}$, which controls the magnitude of the spatial change. As presented in Table 5, the performance variations are not significant across all spatial distributions. Compared to the results in Table 3, although there is indeed a slightly greater decline in FLORE’s performance, the impact is still limited, and FLORE consistently maintains good accuracy across different proportion factors.

Overall, FLORE is robust to changing conditions in the real world. We attribute this partly to the GM’s ability to capture the underlying distribution inherent to the sketching problem, while compressive sensing enables the model to effectively detect anomalous changes (Mardani & Giannakis, 2015).

H. Applications & Limitations

At the end of this work, we discuss the practical applicability of FLORE across a range of sketch-based tasks and outline its current limitations along with promising directions for future work.

Applicable scenarios. First, we have demonstrated the applicability of FLORE to four tasks, including *frequency estimation*, *heavy hitter detection*, *distribution estimation*, and *entropy estimation*. Since our analysis covers almost all linear aggregation scenarios, which are the most fundamental statistics, the proposed approach can also perform well on all the following use cases. (i) *Heavy changer detection* (Tang et al., 2019). The task aims to identify the elements whose frequency changes between two adjacent epochs are larger than the predefined threshold, with applications to imply the existence of a DDoS attack (Douligieris & Mitrokotsa, 2004). (ii) *Blackhole detection* (Mai et al., 2011). In this task, the blackhole behavior is modeled by a normal entity A and a faulty entity B. Specifically, when the data stream is transmitted from entity A to entity B, entity B drops the items associated with certain specific keys due to an interface failure. The goal of the task is to identify the missing (i.e., victim) keys. (iii) *Incorrect routing detection* (Guo et al., 2015). Consider three entities A, B, and C, where entity A can send data items to both entity B and entity C. Incorrect routing refers to the scenario where, due to corruption in entity A’s routing table, a subset of keys that should have been sent to entity B are mistakenly forwarded to entity C. The goal of the task is to identify the keys affected by this incorrect routing. The above three binary classification tasks can be naturally derived from our heavy-hitter detection task. (iv) *Norm estimation* (Alon et al., 1996). The problem of ℓ_p norm estimation is to provide a multiplicative approximation to $|f|_p := (\sum_i |f_i|^p)^{1/p}$, which is similar to distribution & entropy estimation. (v) *Graph sketching* (McGregor, 2014). The task falls into the scope of combinatorial problems on graphs. We consider dynamic graph streams where edges can be both inserted and deleted. The input is a sequence $S = \langle a_1, a_2, \dots \rangle$, where $a_i = (e_i, \Delta_i)$ with e_i encoding an undirected edge as before, and $\Delta_i \in \{-1, 1\}$. The multiplicity of an edge e is defined as $f_e = \sum_{i: e_i=e} \Delta_i$. For simplicity, we restrict our attention to the case where f_e is in $\{0, 1\}$ for all edges. Then, let $f \in \{0, 1\}^{\binom{N}{2}}$ be the vector whose entries equal the current edge multiplicities f_e , and let $\mathcal{A}(f) \in \mathbb{R}^m$ denote the sketch of this vector. Upon arrival of an update (e, Δ) , we can simply update $\mathcal{A}(f)$ as: $\mathcal{A}(f) \leftarrow \mathcal{A}(f) + \Delta \cdot \mathcal{A}(i^e)$ where i^e is the vector that is “1” only in the coordinate corresponding to edge e , and zero elsewhere. We can see that the formulation of this problem is entirely analogous to our linear sketching problem. Thus, it suffices to store the current sketch and leverage FLORE to compute the solution.

Limitations and future works. We believe that our investigation of generative optimization for data sketching has but scratched the surface. In what follows, we outline current limitations of our approach, as well as intriguing directions for future research. (i) In the FLORE’s data structures, a Bloom Filter is employed to determine whether an element belongs to a known set. As a probabilistic data structure, however, the Bloom Filter may incur false positives, and achieving an extremely low false-positive rate requires memory usage that grows nearly linearly with N . To mitigate this overhead, future work may explore learning-enhanced Bloom Filter (Kraska et al., 2018), biasing key mappings toward higher-indexed regions of the bit array can substantially reduce storage requirements while preserving query accuracy. (ii) Note that our method reconstructs the state information of all elements simultaneously, which is not well-suited for point queries. For instance, after the model outputs f , we must locate the position corresponding to a specific key and retrieve its value, an operation that incurs $\mathcal{O}(N)$ complexity. A good direction for future research is the development of accelerated mapping indices. By decoupling the generative reconstruction from the lookup mechanism, we aim to achieve sub-linear or constant-time retrieval for specific keys, thereby enhancing FLORE’s utility for real-time, per-element monitoring.